Processing, Structure and Ferroelectric Properties of PVDF-Based Ferroelectric Polymers

Nan Meng

Submitted in partial fulfilment of the requirements of the Degree of Doctor of Philosophy

School of Engineering and Materials Science,

Queen Mary, University of London,

London, UK

May 2017

Declaration

I, Nan Meng, confirm that the research included within this thesis is my own work or that where it has been carried out in collaboration with, or supported by others, that this is duly acknowledged below and my contribution indicated. Previously published material is also acknowledged below.

I attest that I have exercised reasonable care to ensure that the work is original, and does not to the best of my knowledge break any UK law, infringe any third party's copyright or other Intellectual Property Right, or contain any confidential material.

I accept that the College has the right to use plagiarism detection software to check the electronic version of the thesis.

I confirm that this thesis has not been previously submitted for the award of a degree by this or any other university.

The copyright of this thesis rests with the author and no quotation from it or information derived from it may be published without the prior written consent of the author.

Signature:

Date:

Abstract

Polyvinylidene fluoride (PVDF) and its copolymer with trifluoethylene (PVDF-TrFE) have been widely investigated. This is largely attributed to their ferroelectric properties, which are present in a limited number of polymers. In comparison with the more widely used ferroelectric ceramics, the ease of their fabrication makes them attractive in flexible electronic devices. Despite many advances in their application, we are still lacking a complete fundamental understanding of the relationship between their structure and the functional properties.

The melt-extrusion of PVDF revealed that the α-phase is predominantly formed in films. The ferroelectric β-phase PVDF was obtained by high temperature drawing of the α-phase of as-extruded films. It was observed that a minimum draw ratio of 3 is required to generate the β-phase. Chain mobility is crucial to the formation of β-phase. Too high chain mobility when drawing at temperatures above 100 °C can only orientate the pre-existing α-crystals without making the chain conformation change to form the β-crystals. Furthermore, the comparison between the produced α- and β-PVDF films is summarized. The α-PVDF films crystallized into spherulites with random orientation, while β-PVDF films displayed fibriliar structure showing preferred orientation of the polymer chains along the drawing direction. The overall crystallinity obtained from DSC data hardly varied, however, the drawn β-PVDF films had a lower melting temperature, which was also confirmed from the dielectric temperature spectra. The drawn β-PVDF films showed higher dielectric constant and larger remnant polarization

compared with the as-extruded α-PVDF films, which is mainly ascribed to their higher β-phase content and preferred orientation.

Highly aligned PVDF-TrFE films were processed using a melt extrusion processing route. Crystalline structure and orientation were optimized by controlling the melt extrusion conditions. XRD patterns suggested that there was nearly perfect alignment of the c-axis (polymer chain direction) along the extrusion direction in the optimized as-extruded films. SEM analysis confirmed the morphology of the crystalline phase, showing edge-on lamellae stacked perpendicular to the extrusion direction. DSC data indicated high crystallinity and well-ordered ferroelectric structure of the extruded films. FTIR spectroscopy revealed strong intermolecular dipole-dipole interaction in the extruded films. Accordingly, the optimized as-extruded PVDF-TrFE films exhibited a coercive field of 24 kV/mm, half of the commonly reported values for bulk films (~ 50 kV/mm) and a remnant polarization of 0.078 C/m^2 which further increased to 0.099 C/m^2 after annealing. This value is close to the theoretical limit (0.102 C/m^2) assuming perfect in-plane c-axis orientation and 100% crystallinity.

The typical limitations of PVDF - low crystallinity and indirect ferroelectric β-phase crystallization - and PVDF-TrFE - higher materials and processing costs and a low Curie point - are tackled by a simple and industrially viable melt blending approach. Despite the immiscible nature of PVDF and PVDF-TrFE, strong interactions exist between the two polymers when co-melt processed, which substantially affect the morphology and texture of the blends as well as their dielectric and ferroelectric properties. Surprisingly, minor amounts of PVDF-TrFE led to a significant increase in the β-phase content and preferred orientation of PVDF, well beyond the rule-of-

mixtures. Moreover, the blends exhibited maximum increases in the dielectric constant of 80% and 30%, respectively compared with pure PVDF and PVDF-TrFE. The ferroelectric remnant polarization increased from 0.040 to 0.077 C/m^2, while the coercive field decreased from 75 to 32 kV/mm with increasing PVDF-TrFE from 0 to 40 wt. %. The enhancement of properties is explained by the strong interactions at the interfaces between PVDF and PVDF-TrFE, which also suppresses the Curie transition of PVDF-TrFE, providing a potentially increased working temperature range for blended films, which is important in applications like non-volatile energy storage devices, ferroelectric field-effect transistors and touch sensors.

Ferroelectric composites, integrating dielectric ceramic fillers with mechanically flexible polymers, are promising materials for flexible electronic applications. Numerous research works have demonstrated enhanced dielectric and ferroelectric properties of composite materials. However, the mechanisms responsible for these enhancements are not completely understood. Herein, PVDF and $BaTiO_3$ (BTO) were used to study the effect of dielectric filler on the crystallization, phase transformation and dielectric properties of PVDF. The crystallization of α-PVDF was not affected by the presence of BTO particles, but small amounts of BTO (< 3 vol. %) made PVDF crystallize into larger spherulites. This is linked to crystallization kinetic studies, which showed that BTO acted as a nucleation agent for large full ring banded spherulites when its content was less than 1 vol. %. Furthermore, solid state drawing in the presence of BTO particles promoted the formation of β-PVDF with more pronounced crystalline orientation at high drawing temperatures (120 °C). The dielectric and ferroelectric properties were enhanced with BTO filling. The 100 °C oriented drawn PVDF tape exhibited a dielectric permittivity of 14 (100 Hz) and remnant polarization of 0.080

C/m^2 (10 Hz), which increased to 20 and 0.095 C/m^2, respectively, after filling with 5 vol. % BTO; neither resulting in high dielectric loss tangent (~ 0.02) nor obvious current leakage. Moreover, the coercive field decreased from 80 to 50 kV/mm with increasing BTO content from 0 to 5 vol. %.

Acknowledgments

It was difficult to start writing acknowledgments. By all respects, the PhD study is a journey with ups and downs. I would not say I liked every single part of it, especially, the failure of experiments, the unexplainable data, the rejection of paper and the rainy cold in London.

I would like to first thank my beloved country, P.R. China, for offering the CSC scholarship and letting me have such a fantastic international experience.

Then, the most heartfelt gratitude will be given to my supervisor, Prof. Mike Reece. I still remember our first discussion. It was in your office, and I showed you my first ferroelectric PE-loops without the units or descriptions of X-Y axes. I was thrilled because I finally got non-banana-shaped curves. You listened to me patiently and explained to me the mechanism and most importantly taught me how to draw a figure scientifically. In research, you are passionate and conscientious. In life, you are thoughtful and gentle. The things I learnt from you completely changed me and made me a better person.

Dr. Emiliano Bilotti, my secondary supervisor, who not only inspires me in polymer research but also gives me support and help when I feel depressed. I am truly grateful for your patience and kindness. Dr. Haixue Yan, a quick-witted, resourceful and intelligent guy, who knows everything about ferroelectrics. I really appreciate the discussion with you. Dr. Wei Tu, an expert in polymer processing, who leads me during the experiment. Thank you for your endless help and guides. Dr. Theo Saunders, a genius of science and engineering. Thank you for the test equipment you built for our

whole group. Dr. Rory Wilson, Dr. Alice Williams and Mr. Dennis Ife, I am truly grateful for your technical support.

I was very lucky to have so many lovely PhD girl colleagues, Yi Liu, Min Yu, Xintong Ren, Yunyin Lin, and Kening Wan, I will miss our girls' talk, hang-out and the shared snacks every time we were famished late afternoon. Also, Dr. Han Zhang, Dr. Olivier Picot, Dr. Kan Chen, Dr. Amit Mahajan, Jiyue Wu and Jun Cao, I appreciate any kind of support provided by these gentlemen.

Special thanks are given to my boyfriend, Rui Mao. We had our undergraduate degree at Donghua University and PhD at QMUL. Whenever I had a dilemma of polymers, I could discuss with you. You always gave me suggestions and comments no matter whether they made sense or not. You are 'the walking polymer physics'. But trust me, you are more than that to me. You are the chocolate sauce on my ice cream. I am glad and fortunate to have you by my side.

Last but not least, I want to give my huge thanks to my parents and brother. Thank you, everyone, for tolerating my endless grumbles of everything.

Researchers keep saying ferroelectrics are good candidate materials for non-volatile memories. How I wish I could save every single bit of good memories using ferroelectrics. I will miss the PhD life, I will miss Queen Mary and I will miss London.

Table of Contents

List of Abbreviations

1D-WAXD	One dimensional wide angle X-ray diffraction
2D-WAXD	Two dimensional wide angle X-ray diffraction
AC	Alternating current
A.U.	Arbitrary unit
$BaTiO_3$/ BTO	Barium titanate
BOPP	Biaxial-oriented polypropylene
CA	California
CL	Cooled phase from high temperature phase of PVDF-TrFE
d_{31}, d_{32}, and d_{33}	Piezoelectric coefficients
D-E loops	Displacement-electric field loops
DMA	Dynamic Mechanical Analyser
DSC	Differential Scanning Calorimetry
E_c	Coercive field
f	Herman's orientation factor
FTIR	Fourier Transform Infrared Spectroscopy
HT	High temperature phase of PVDF-TrFE
IE curves	Current-Electric field curves
LB	Langmuir-Blodgett
LG	Landau–Ginzburg
LT	Low temperature phase of PVDF-TrFE
MC 15	15 ml micro compounder
MMT	montmorillonite
M_n	Number average molecular weight
M_w	Weight average molecular weight
MWCNT	multiwalled carbon nanotube
NPL	National Physical Laboratory
OR	Oregon
P_r	Remnant polarization
P_s	Spontaneous polarization
P_{sat}	Saturated polarization

PBA	Poly(1,4-butylene adipate)
PE	Polyethylene
PET	Poly(ethylene terephthalate)
PFBPA	Pentafluorobenzyl phosphonic acid
PMMA	Polymethyl methacrylate
PMN-PT	Lead magnesium niobate-lead titanate
PP	Polypropylene
PVDF	Polyvinylidene fluoride
PVDF-CTFE	Poly(vinylidene fluoride-chlorotrifluoroethylene)
PVDF-HFP	Poly(vinylidenefluoride-hexafluoropropylene)
PVDF-TFE	Poly(vinylidene fluoride-tetrafluoroethylene)
PVDF-TrFE	Poly(vinylidene fluoride-trifluoethylene)
PVF	Polyvinyl fluoride
SAXS	Small-angle X-ray scattering
SEM	Scanning Electron Microscopy
SiO_2	Silica
T_c	Curie temperature
T_{cry}	Crystallization temperature
T_g	Glass transition temperature
T_m	Melting temperature
TG^+TG^-	Trans-gauche chain conformation
TiO_2	Titanium dioxide
TTT	All-trans chain conformation
U_e	Energy storage density
UK	United Kingdom
USA	United State of America
VDF	Vinylidene fluoride
WAXS	Wide-angle X-ray scattering
XRD	X-ray Diffraction

List of Figures

List of Tables

Chapter 1 Introduction

1.1 Background

Ferroelectrics are a special category of dielectrics which have spontaneous polarization that can be switched by applying an external electric field[1-3]. The first discovered ferroelectric was Rochelle salt (potassium sodium tartrate tetrahydrate, $KNa(C_4H_4O_6)\cdot 4H_2O$) in 1921.[4] Then the discovery and in-depth research in the 1940s on ferroelectric ceramics represented by barium titanate ($BaTiO_3$) opened a new chapter for ferroelectrics.[1, 5, 6] From the 1970s, two non-solid ferroelectrics had been thoroughly investigated because of the possibility to apply them in flexible devices. One of them was ferroelectric liquid crystals with a rod-like structure;[7] another was the ferroelectric polymers of which the typical ones are polyvinylidene fluoride (PVDF) and its copolymer with trifluoethylene (PVDF-TrFE). Ferroelectric switching of PVDF and PVDF-TrFE is accomplished by the rotation of the polar dipoles (CH_2-CF_2 and CHF-CF_2) about the chain axes (C-C) with domain wall progressing through chain rotations in the a-b plane of lamella.[8-11]

1.2 Scope of this thesis

A review about the fundamental structure, dielectric and ferroelectric properties of PVDF and PVDF-TrFE is given in Chapter 2, which also includes the reported work of blends among fluoropolymers and PVDF based composite materials with enhanced dielectric and ferroelectric properties. The experimental procedures and characterization techniques used in this PhD research are summarized in Chapter 3. The processing of

PVDF is described in Chapter 4, which focuses on the influence of extrusion and the uniaxial drawing conditions on the phase transformation of PVDF. The experimental results and discussions of the relationship between structures and functional properties for the extruded PVDF-TrFE and PVDF/PVDF-TrFE blended films are explained in Chapters 5 and 6, respectively. The crystallization kinetics and enhancement of dielectric and ferroelectric properties of PVDF composites with BTO fillers are discussed in Chapter 7. The conclusion and future work are summarized in Chapter 8.

Chapter 2 Literature Review

2.1 Structure of PVDF and its copolymer PVDF-TrFE

2.1.1 PVDF

PVDF is a semi-crystalline polymer with at least four polymorphs; α, β, γ, and δ-phase. The energetically favourable polymorph is the α-phase which is non-polar due to the self-cancelation of dipoles resulting from the antiparallel packed trans-gauche (TG^+TG^-) molecules.[10] If TG^+TG^- molecules pack in a parallel fashion; the formed polymorph is δ-phase.[12] The favoured ferroelectric polymorph is the β-phase with all-trans (TTT) chain conformation.[13] An intermediate conformation $T_3G^+T_3G^-$ takes a parallel packing to form the γ-phase.[14] Figure 2.1 depicts the phase transition among different polymorphs along with chain conformation and parameters of corresponding unit cells.

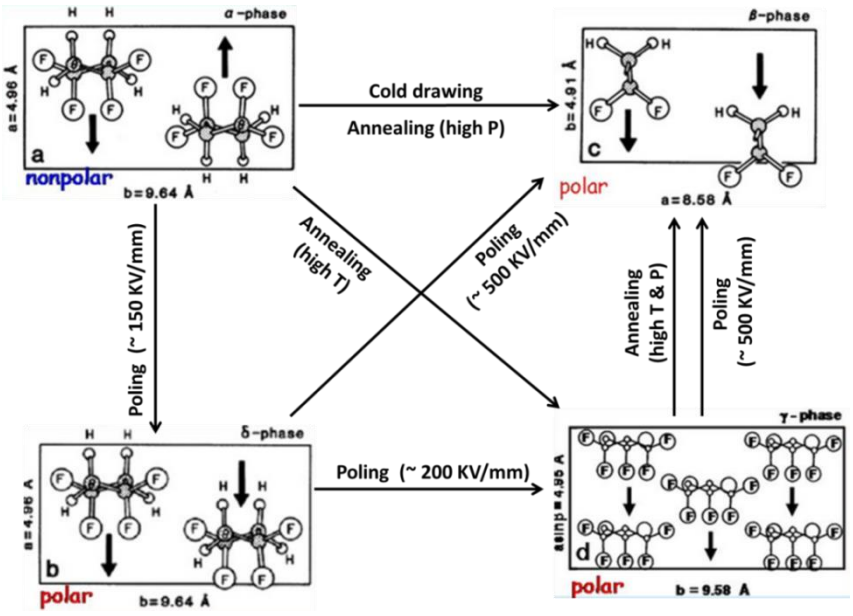

Figure 2.1 A scheme of crystalline transformations of PVDF phases induced by thermal, mechanical and electrical treatment (reproduced based on[13, 15]).

2.1.2 PVDF-TrFE

PVDF-TrFE is a random copolymer due to the size similarity between the hydrogen and fluorine atoms. Based on potential energies calculated by Hasegawa[10], the all-trans chain conformation (β-phase) favours inter-molecularly while trans-gauche (α-phase) favours intra-molecularly. However, the introduction of small amounts of TrFE stabilizes all-trans conformation relative to other conformations intra-molecularly[16] but further introduction causes severe instability. As a result, the chain conformation and corresponding crystalline structure of PVDF-TrFE exhibit composition dependence.[17-20] Figure 2.2 shows the different characteristics of PVDF-TrFE as a function of composition. From Figure 2.2, PVDF-TrFE can be divided into three main categories over the entire composition range; VDF < 50 mol. %, VDF 50-80 mol. % and VDF > 80 mol. %. In the VDF 50-80 mol. % range, Figure 2.2 (b) shows the existence of a Curie transition. The values of Curie temperature (T_c) upon heating are higher than those on cooling, suggesting thermal hysteresis of the first order transition. For 80 mol. % VDF, T_c values are similar to the melting temperature (T_m). Consequently, above 80 mol. % the Curie transition is merged with the melting process. When the VDF content is below 50 mol. %, the structure instability makes the ferroelectric transition weak and obscure.

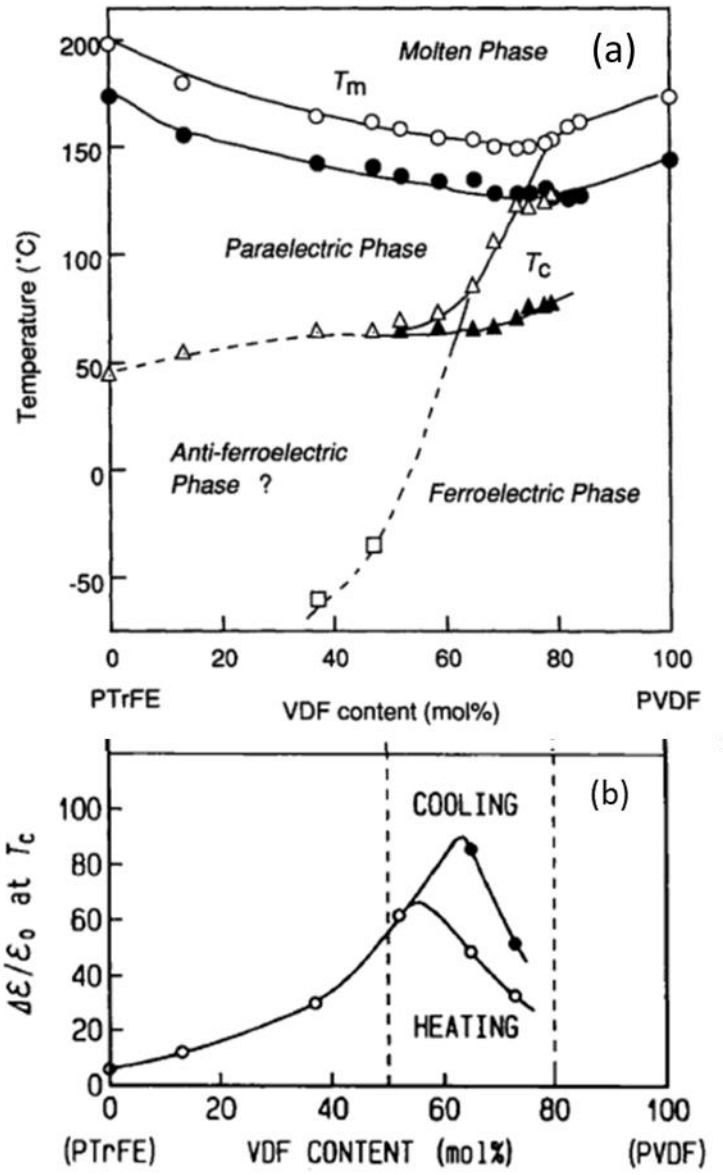

Figure 2.2 Characteristics of PVDF-TrFE as a function of composition: (a) phase diagram; (b) dielectric constant at Curie point (taken from[15, 21]). In the phase diagram, o= melting temperature (T_m), ●= crystallization temperature (T_{cr}), Δ= Curie point during heating (T_{c+}), ▲= Curie point during cooling (T_{c-}), □=ferroelectric and antiferroelectric transition

From the point of view of Curie transition, the crystalline phases of PVDF-TrFE can be notated as the low temperature phase (LT); high temperature phase (HT) and cooled phase (CL). The LT phase is intrinsically the same with respect to the chain conformation of the β-phase.[22, 23] The HT phase contains large amount of gauche bonds

and can be considered as a mixture of γ- and α-phase.[22] The CL phase is formed by slowly cooling the HT phase. The CL phase is regarded as a tilting β-phase and transforms into LT phase under stretching or poling.[23] Table 2.1 lists the crystallographic data for PVDF and PVDF-TrFE.

Table 2.1 Crystallographic data of PVDF and PVDF-TrFE (reproduced from[22-24])

		Unit cell parameters	**Molecular chain**
PVDF	α-	a=4.96 Å b=9.64 Å c =4.96 Å β=90°	TG^+TG^-
	β-	a=8.58 Å b=4.91 Å c =2.56 Å	TTT
	γ-	a=4.96 Å b=9.58 Å c =9.23 Å β=92.9°	$T_3G^+T_3G^-$
	δ-	a=4.96 Å b=9.64 Å c =4.96 Å β=90°	TG^+TG^-
PVDF-TrFE 55/45 mol. %	LT	a=9.12 Å b=5.25 Å c =2.55 Å	TTT
	HT	a=9.75 Å b=5.63 Å c =4.60 Å a/b=√3	$T_3G^+T_3G^-/TG^+TG^-$
	CL	a=9.16 Å b=5.43 Å c =2.528 Å β=92.9° (assumed) Tilt angle φ=18° in the tilt plane	Long trans segments with irregular gauche linkage

2.2 Summary of properties for β-PVDF and PVDF-TrFE

2.2.1 Ferroelectric properties

The ferroelectric properties are generated from the permanent dipoles with the spontaneous polarization (P_s) along the b-axis. The dipole moment of CH_2CF_2 is μ_v=7.0×10^{-30} Cm. The P_s of β-phase PVDF is much larger than the other polymorphs due to the alignment of the molecular dipoles along one direction. The theoretical P_s value with regard to the unit cell parameters is $P_s = 2\mu_v/abc$= 0.13 C/m^2. The ferroelectric switching is accomplished by the coupled global rotation of the molecular polymer chain axis (c-axis).[25] The P_s value is intrinsic and solely dependent on the crystal structure, while the remnant polarization P_r is linked to the degree of crystallinity and orientation of the c-axis. If the c-axis is perfectly oriented in the film plane and the b-axis about the c-axis is random, the maximum possible value (100% crystalline) of P_r is 95% of P_s.[15] Therefore good in-plane c-axis orientation and high crystallinity are required to achieve a high P_r value. The orientation of a- and b-axes hardly influences the remnant polarization as long as the c-axis shows perfect in-plane orientation.

With regard to PVDF-TrFE, three types of dipole unit contribute to the polarization. Legrand group[26] reported ferroelectric properties for three compositions PVDF-TrFE (80/20, 70/30 and 60/40 mol. %) based on neutron diffraction data (Table 2.2, β-PVDF was added for direct comparison). Results from Table 2.2 clearly reveal the decrease of polarization with increasing molecular ratio of TrFE, which is due to the reduction of dipole moment and the expansion of the unit cell volume.[26] PVDF-TrFE with appropriate composition (normally 65-80 mol. %) is superior to PVDF due to the high crystallinity of the ferroelectric phase (~ 80 %). Annealing PVDF-TrFE above its Curie

temperature but slightly below its melting point yields a much higher crystallinity (> 90 %),[27] which is due to the high chain mobility allowing the rearrangement of polymer chains and the occurrence of lamellae thickening. Higher crystallinity favours higher remnant polarization.[28] The commonly reported values of remnant polarization for typical annealed PVDF-TrFE are about 0.090 C/m^2 (Table 2.3) which is higher than that of PVDF (~ 0.060 C/m^2).[25, 29]

Table 2.2 Effect of the composition of PVDF-TrFE on: crystallographic data, dipole moment of a monomer μ, spontaneous polarization P_s, experimental values of remnant polarization P_r and Curie transition temperature upon heating T_{c+}. Data of β-PVDF was added for reference.[26]

	β-PVDF	**80/20**	**70/30**	**60/40**
a(Å)	8.58	8.9	9.05	9.2
b(Å)	4.91	5.05	5.12	5.18
c(Å)	2.56	2.55	2.55	2.55
Volume (Å^3)	107.8	114.6	118.2	121.5
μ	7.0	6.3	6.0	5.6
P_s (C/m^2)	0.130	0.110	0.102	0.092
P_r (C/m^2)	0.0583[25]	0.080[30]	0.092[31]	0.088[32]
T_{c+}(°C)	—	130.5	88.5	64.5

The coercive field (E_c) corresponds to the electric field at which the net polarization of a material is zero and the point where the maximum rate of ferroelectric switching occurs.

Experimental values of E_c for most ferroelectrics are a few orders of magnitude lower than the theoretical Landau–Ginzburg (LG) intrinsic values $E_c=0.5P/\varepsilon\varepsilon_0$[33], which is built on the electric field needed to overcome the minimum of free Gibbs energy density. The LG intrinsic values for PVDF and PVDF-TrFE are 340 and 500 kV/mm. The much lower experimentally measured values (Table 2.3) are due to the actual mechanism of nucleation of ferroelectric domains which involves the localized nucleation of domains followed by the forward and sideways growth.[34] Under this mechanism the domain nucleation normally occurs at defects/imperfections. Apart from acting as domain nucleation agents, defects also serve as pinning sites during domain wall movement and thereby hindering the subsequent growth of domains. Consequently, the E_c for ferroelectrics is an extrinsic property and importantly dependent on the degree of crystallographic order/perfection. The semi-crystalline nature and unavoidably irregular polymer crystals escalate the complexity of its ferroelectric polarization reversal. As for PVDF and PVDF-TrFE, their dipole moments align along the b-axis and rotate around the c-axis. The relative orientation of the b-axis with respect to the applied electric field influences the E_c value. Kassa *et al.* [35] introduced a simple model to explain the crystalline orientation effect on ferroelectric reversal; the perfect in plane orientation of a- and c-axis minimizes the value of E_c, which is consistent with other reported work.[36, 37] Apart from crystalline orientation, edge-on lamellae especially with shorter length[35] and lower domain wall energy as a consequence of better crystal perfection[36, 38] favour easier ferroelectric reversal. Another influencing factor reported by Tasaka *et al.* [39] was that the higher crystallinity along with thicker lamellae crystallites eased the ferroelectric switching process, which is due to a reduction in the number of folding chains arising from the expansion of intermolecular distance.

Table 2.3 Reported values of coercive field (E_c) for PVDF and PVDF-TrFE.

	Sample	**Sample description**	**Measurement condition**	E_c **(kV/mm)**	P_r **(C/m^2)**
Kepler *et al.* [25]	PVDF	Uniaxially oriented β ~ 30 μm; Biaxially oriented α+β ~ 25 μm	280 kV/mm; 30 Hz	~ 90	0.06 0.06
Furukawa *et al.* [29]	PVDF	Coextruded α+β	200 kV/mm; 0.8 Hz	~ 75	0.06
Davis *et al.* [28]	PVDF	(1) β; (2) α; (3) α+β	200 kV/mm; 60 Hz	(1) ~ 50; (2) ~ 90; (3) ~ 85	0.05 0.06 0.06
Li *et al.*[40]	PVDF	Spin-coated δ 400 nm	250 kV/mm; 100 Hz	115	0.07
Zhang *et al.* [41]	PVDF-TrFE 50/50 mol. %	Hot compression 25-40 μm	160 kV/mm; 1-10 Hz	45	0.06
Furukawa *et al.* [42]	PVDF-TrFE 52/48 mol. %	Hot compression 20 μm	200 kV/mm; 300 Hz	40	0.06
Davis *et al.* [28]	PVDF-TrFE 65/35 mol. %	Hot compression 65-100 μm	200 kV/mm; 60 Hz	50	0.06
Huang et al. [43]	PVDF-TrFE 68/32 mol. %	Uniaxially stretched 20 μm	150 kV/mm; 10 Hz	52	0.1
Davis *et al.* [28]	PVDF-TrFE 73/27 mol. %	Hot compression 65-100 μm	60 kV/mm; 60 Hz	40	0.07

	Sample	Sample description	Measurement condition	E_c (kV/mm)	P_r (C/m^2)
Ohigashi *et al.* [44, 45]	PVDF-TrFE 74/26 mol. %	Uniaxially stretched, clamped annealed at 135 °C for 2h and poled at 25 °C; 5-100 μm	55 kV/mm; 100 Hz	38	0.10
Kimura *et al.* [46]	PVDF-TrFE 75/25 mol. %	Spin-coated 60 nm	Integrating switching current as a function of time.	125	0.08

Table 2.3 continued

The last row of Table 2.3 shows a much higher E_c (125 kV/mm) for 60 nm PVDF-TrFE 75/25 mol. %, which is due to the restraint of domain nucleation for ultra-thin films. Figure 2.3(a) shows the thickness dependence of E_c of PVDF-TrFE.[34, 46-53] The E_c of PVDF-TrFE films processed by Langmuir-Blodgett (LB) technique appeared to fit the L-G intrinsic value. It is regarded that 100 nm is a critical thickness for PVDF-TrFE. Contrary to PVDF-TrFE, PVDF exhibits more extrinsic ferroelectric switching;[54-58] The E_c values are independent of film thickness, especially above 20 nm (Figure 2.3(b)). This is an obvious advantage of PVDF compared to PVDF-TrFE for application as thin films.

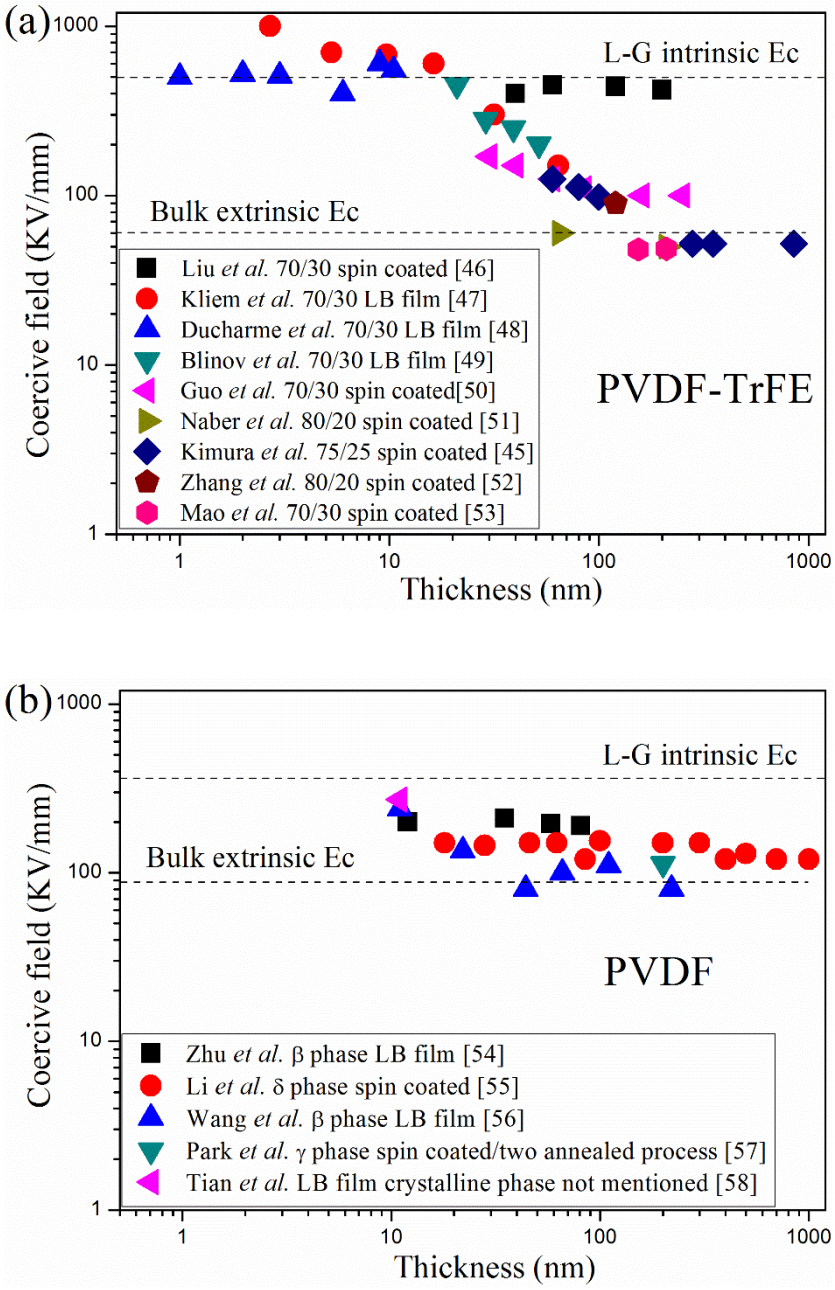

Figure 2.3 Reported E_c values as a function of film thickness: (a) PVDF-TrFE; (b) PVDF.

Summing up the ferroelectric properties of PVDF and PVDF-TrFE: (1) P_s theoretical value for β-PVDF is 0.13 C/m^2, for PVDF-TrFE P_s decreases with increasing molecular ratio of TrFE. Average experimentally measured P_r values for PVDF (crystallinity ~ 50%) and PVDF-TrFE (crystallinity ~ 80%) are 0.060 and 0.090 C/m^2, respectively; (2)

intrinsic LG coercive field values for PVDF and PVDF-TrFE are 340 and 500 kV/mm, respectively, which are much larger than the measured E_c; PVDF 90 kV/mm, PVDF-TrFE 50 kV/mm. In-plane orientation of c-axis facilitates ferroelectric reversal. E_c values of thin PVDF-TrFE films show thickness dependence, and the critical thickness of PVDF-TrFE is about 100 nm. However, thin PVDF films exhibit more extrinsic ferroelectric switching; E_c values are independent of film thickness especially for films thicker than 20 nm.

2.2.2 Dielectric properties

The dielectric properties of PVDF and PVDF-TrFE are sensitive to the degree of crystallinity, crystallite size and crystalline orientation. At 1 kHz and 25 ℃, reported values the real part of the dielectric constant for PVDF and PVDF-TrFE are 8-19[59-62] and 8-17[15, 19, 42, 63], respectively.

The dielectric frequency spectra for PVDF and PVDF-TrFE(65/35 mol. %) are shown in Figure 2.4[15] which also includes data for PTrFE and poly(vinylidene fluoride-tetrafluoroethylene) PVDF-TFE(80/20 mol. %) copolymer. All four exhibit a relaxation process at ~ 1 MHz related to non-crystalline molecular motions (α_a), while PVDF shows another relaxation process at ~ 1 Hz produced by the crystalline motions in the α phase.[64]

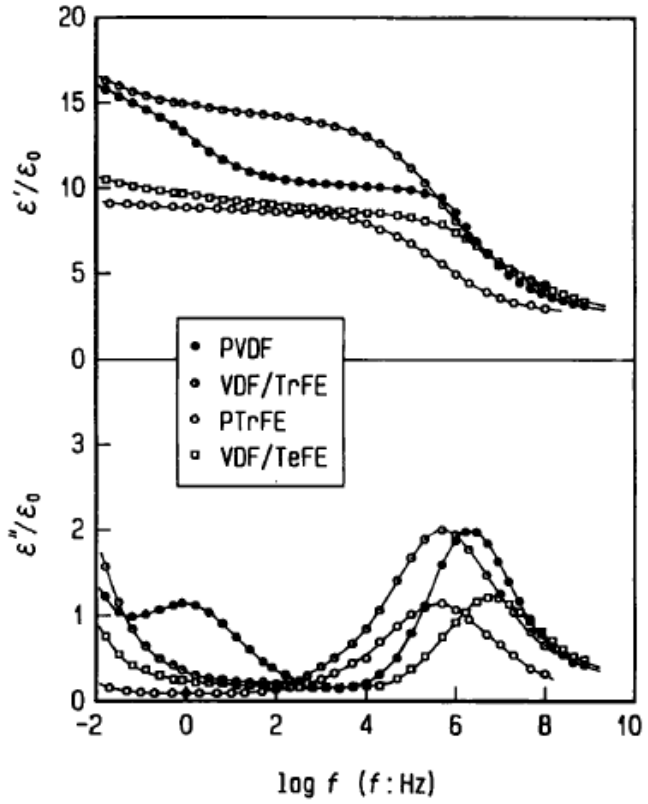

Figure 2.4 Dielectric frequency spectra of PVDF, PVDF-TrFE(65/35 mol. %), PTrFE and PVDF-TeFE(80/20 mol. %) at room temperature.[15]

Figure 2.5(a, b) shows dielectric temperature spectra at different frequencies for PVDF, and two relaxation are denoted; the lower one at -25 ℃ and 1 kHz is ascribed to the glass transition (T_g), the temperature of which shifts to higher temperature with increasing frequency (β relaxation), while the higher one is assigned to the chain relaxation in the crystalline region (α_c). Figure 2.5(c, d) shows dielectric frequency spectra at different temperatures for PVDF. The α_a relaxation process which is generated due to the dipole relaxation in the amorphous region and interfaces between amorphous and crystalline regions. It was observed that the peak position of α_a relaxation shifts to higher frequency with increasing temperature due to the increased

dipole mobility. Yano *et al.* [59] also reported another relaxation process for PVDF below T_g (-80 ℃, at 1 kHz) named γ relaxation.

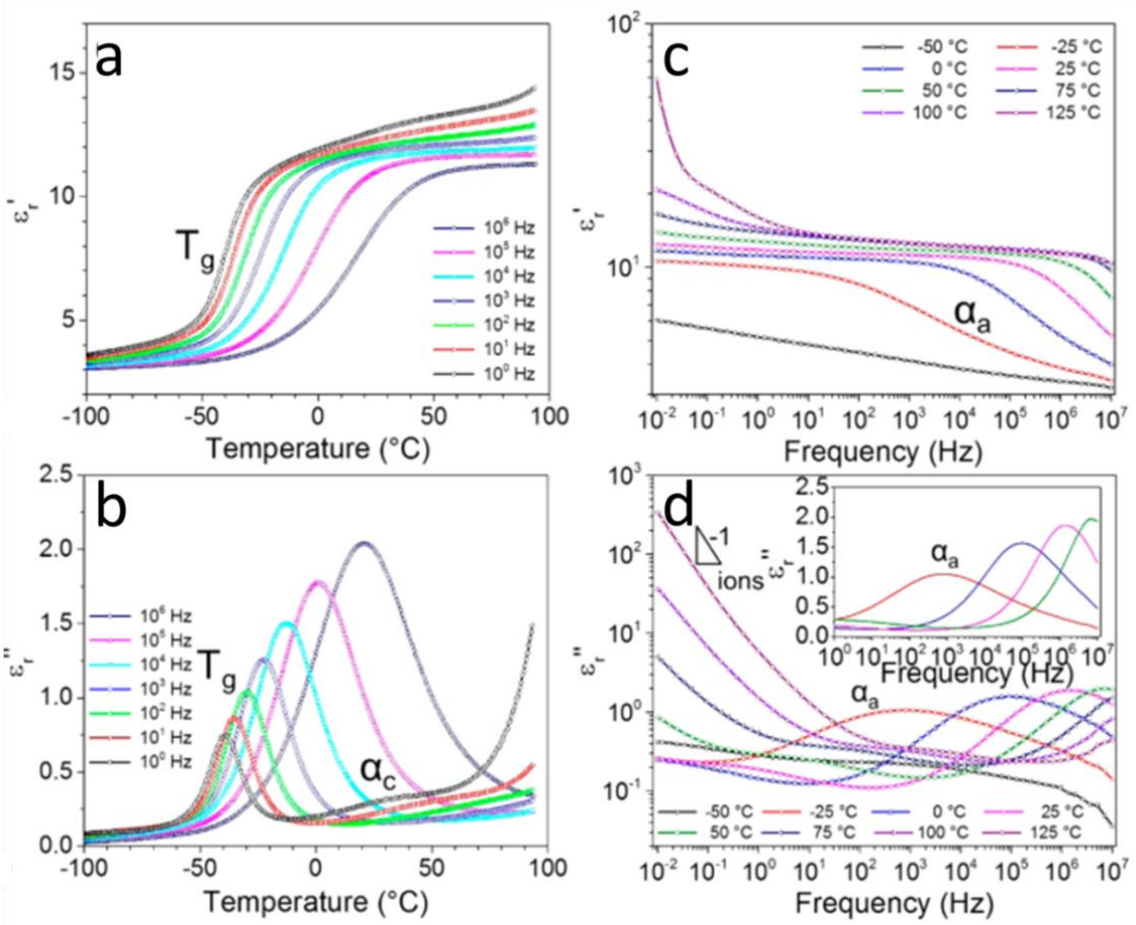

Figure 2.5 Real (a) and imaginary (b) parts of dielectric constant as a function of temperature at different frequency; real (c) and imaginary (d) parts of dielectric constant as a function of frequency at different temperatures.[65]

Yang *et al.* [65] investigated the dielectric properties of biaxially oriented PVDF, and concluded that the orientation of the interfacial amorphous PVDF chains increases the dielectric constant at low electric fields. Simulated values of dielectric constant for PVDF crystals were reported by Karasawa *et al.* [66] where the dielectric constant at zero

frequency for β-PVDF crystals was estimated to be 2.44 (slightly higher than that of α- and γ-) and comparable with the measured value 3.1 (-102 ℃, 0.059 MHz).[67]

Similar to PVDF, PVDF-TrFE (VDF 50-80 mol. %) also exhibits α_a relaxation (non-crystalline molecular motions) and β relaxation (glass transition). Apart from those two relaxation processes, the Curie transition can be observed in dielectric temperature spectra (Figure 2.2). Omote *et al.* [68] reported dielectric anisotropy for highly crystalline and highly oriented PVDF-TrFE (75/25 mol. %) films (Figure 2.6). The chain c-axis was along the stretching direction (orientation factor 0.9986) and the b-axis oriented ±30° off the film normal. In Figure 2.6(a), subscripts 1, 2 and 3 represent the film stretching direction (chain c-axis), film transverse direction and film normal direction, respectively. Values of dielectric constant for a single crystal were derived based on the relative orientation and shown in Figure 2.6(b). ε_2^c was larger than the other two in the whole temperature range below the Curie transition temperature, suggesting chain molecules undergo rotational vibration or torsional vibration around the chain axis due to the CF_2 dipoles along the b-axis.[68] Inset of Figure 2.6(b) shows ε_1^c increases abruptly near the Curie transition, which is attributed to the change of chain conformation from all-trans to trans-gauche.

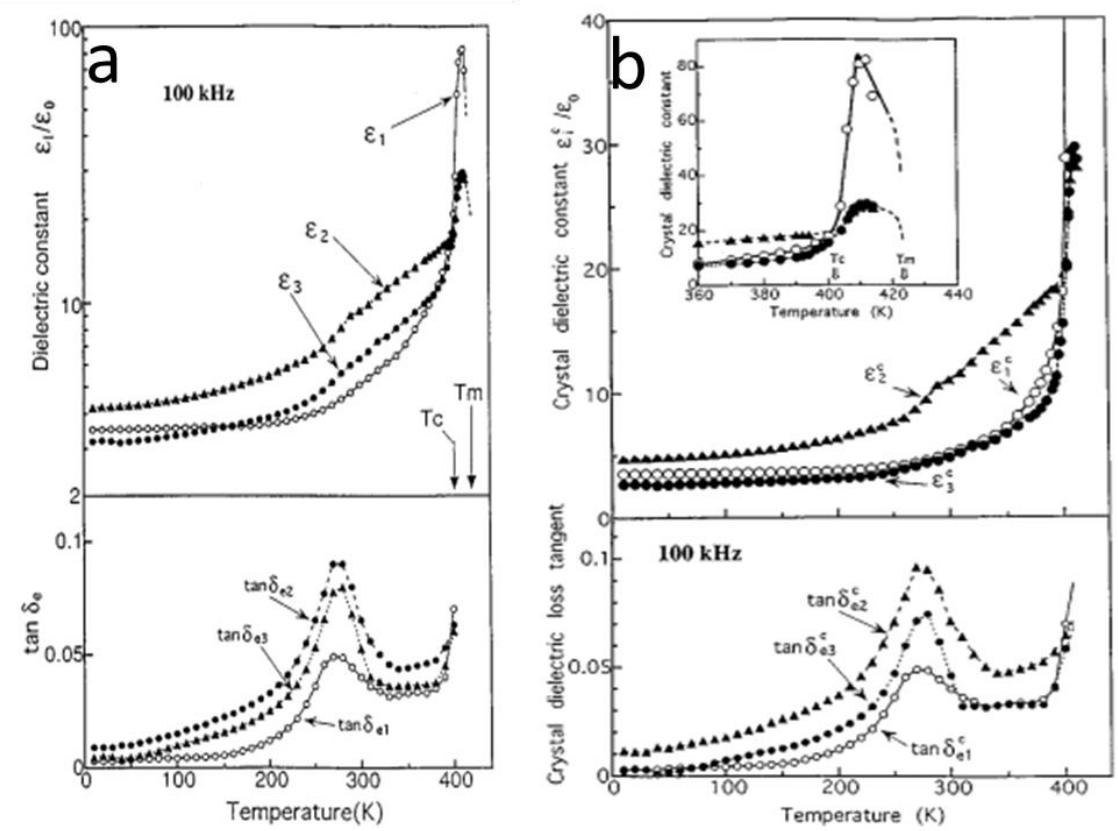

Figure 2.6 Dielectric temperature spectra of poled PVDF-TrFE (75/25 mol. %): (a) films; (b) calculated values for a single crystal.[68]

In conclusion, at low electric fields, the contribution of dipoles to the dielectric polar response in the crystalline regions is minor compared to that of amorphous region. Dielectric frequency spectra for PVDF and PVDF-TrFE exhibit α_a relaxation process at high frequency (~ 1 MHz) related to the motion of non-crystalline molecules, while for α-PVDF another relaxation process exists at low frequency (~ 1 Hz). Dielectric temperature spectra for PVDF show two relaxations; β- (glass transition) and α_c (crystalline molecules motion), while for PVDF-TrFE, apart from β-relaxation Curie transition can be clearly seen. Highly oriented PVDF-TrFE shows dielectric anisotropy, $\varepsilon_{a\text{-axis}}$ is larger than the other two in the whole temperature range below Curie transition

temperature, while $\varepsilon_{c\text{-}axis}$ increases steeply near Curie transition arising from the change of chain conformation (from all-trans to trans-gauche).

2.3 Blends among fluoropolymers

Binary polymer blends can combine the desirable characteristics of two different polymers and thus blending is a common way to modify the properties of specific polymers. Miscibility is an important issue related to the evaluation of blends. PVDF blends with amorphous polymers containing carbonyl group (e.g. polymethyl methacrylate PMMA) exhibiting miscibility in the whole composition range. Contributions from the hydrogen bonding between the double-bonded oxygen of the carbonyl group and the acidic hydrogen of the CH_2-CF_2 group,[69-71] however, crystallization of PVDF and the induced ferroelectric polarization are suppressed with the addition of amorphous polymers.[70, 72] As a result, in order to maintain or even enhance ferroelectric properties, blending with fluoropolymers is more likely to be effective.

Tanaka *et al.* [73] investigated the miscibility of PVDF/PVDF-TrFE blends. Based on the two distinct fusion peaks in the DSC heating run, PVDF was found to be immiscible with PVDF-TrFE regardless of the composition of the copolymer. Gregorio *et al.* [74] came to the same conclusion, but they assumed that PVDF and PVDF-TrFE displayed miscibility on a lamellae level. Figure 2.7 shows the SEM morphology of regions near the spherulite centre for PVDF and PVDF/PVDF-TrFE 50/50 blends. Pure PVDF showed spherulite morphology, while blends displayed homogenously distributed irregular texture, suggesting that PVDF-TrFE molecules are segregated in the regions

between the PVDF spherulites. Despite the immiscibility, strong interaction occurs in the PVDF/ PVDF-TrFE blends, which presumably enhances the ferroelectric properties in the blends.

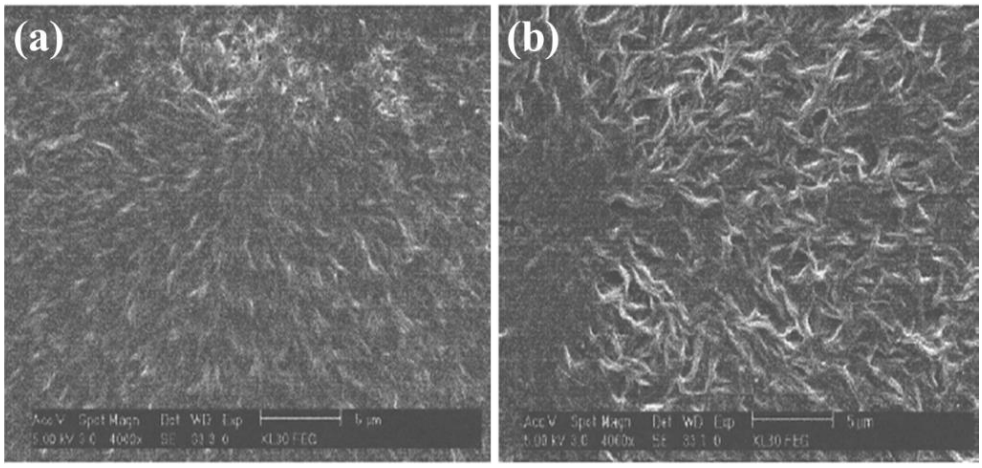

Figure 2.7 SEM morphology of region near spherulite centre: (a) pure PVDF; (b) PVDF/ PVDF-TrFE 50/50 wt. % blends.[74]

Contradiction exists with regard to PVDF/polyvinyl fluoride (PVF) blends. Natta *et al.* [75] reported isomorphism in PVDF/PVF blends. Whereas Guerra *et al.* [76] reported the immiscibility of PVDF/PVF blends not only in the crystalline region (two distinct endotherms in DSC) but also in the amorphous region (combined relaxation peaks in DMA). The reason for this could be the different crystalline phases of PVDF induced by different chain conformation. PVF takes all-trans chain conformation, in Natta's work PVDF was β-phase, while in Guerra's work PVDF was γ-phase, which could give rise to different conclusions for PVDF/PVF blends. Apart from chain conformation diversity, Datta *et al.* [77-80] also pointed out that the H-H defect content difference in PVDF and poly(vinylidene fluoride-tetrafluoroethylene) PVDF-TFE influenced the miscibility of

PVDF/PVDF-TFE blends. As long as H-H defect content difference is larger than 12 mol. %,[77, 78, 80] PVDF and PVDF-TFE are immiscible.

Co-crystallization was observed in PVDF-TrFE blends among different composition.[73] However, such co-crystallization phenomenon only occurred in PVDF-TrFE with small compositional difference (for example, PVDF-TrFE 52/48 and 65/35 mol. % as well as PVDF-TrFE 65/35 and 73/27 mol. %). PVDF-TrFE 52/48 and 73/27 mol. % blends exhibited phase separation both in ferroelectric and paraelectric phase.[73]

Extremely rigorous requirements are needed to achieve miscibility of blends among fluorine polymers, for example, similar chain conformation and thus crystalline phases of PVDF, even defect content in polymer chains, all of which determine the miscibility of the final binary blends. Though PVDF is immiscible with PVDF-TrFE, strong interaction occurs between them forming a homogenous morphology without phase separation. Miscibility of PVDF/PVF blends is affected by the phase of PVDF; β-PVDF with all-trans chain conformation is miscible with PVF. H-H defect content diversity in polymer chains of PVDF and PVDF-TFE also plays an important role in the miscibility of binary blends, as long as the H-H defect content difference is above 12 mol. % immiscible blends will be formed. Moving to PVDF-TrFE blends, small compositional difference (52/48 and 65/35 mol. % as well as 65/35 and 73/27 mol. %) exhibit co-crystallization behaviour while blends with large compositional (52/48 and 73/27 mol. %) difference are partially miscible.

2.4 Enhanced electric properties of ferroelectric polymer composites loaded with inorganic fillers

Ever-increasing demand for flexible electronic devices with excellent properties, like high energy density dielectric–based capacitors, requires a combination of dielectric ceramic particles and polymer matrices.[81, 82] Ceramic materials (for example, barium titanate BTO) possess large dielectric constant, high ferroelectric polarization as well as excellent thermal stability.[83, 84] However, their applications are impeded by the low electric breakdown voltage, extreme processing conditions and high stiffness.[85] Meanwhile, polymers can be easily fabricated into required shapes and have high break down electric field (PVDF, > 400 kV/mm).[86] But the intrinsic values of dielectric constants for polymers are a few orders of magnitude lower than those of ceramic materials (PVDF, $\varepsilon' \sim 10$). Thus, composite materials which integrate high dielectric constant ceramic particles with the mechanical flexibility of polymers provide promising new materials.

2.4.1 Crystallization behaviour difference of PVDF induced by inorganic fillers

Inorganic fillers normally act as nucleation agents in the crystallization process of semi-crystalline polymers,[87, 88] accordingly, the crystallization rate increases and sometimes the melting temperature increases.[89, 90] Dillon and co-workers[88] investigated the structure and morphology of PVDF composites with montmorillonite (MMT) based nanoclay, where the nanoclay showed obvious nucleating effect, increasing the melting (T_m, from 155 to 165 ℃) and crystallization (T_{cry}, from 125 to 145 ℃) temperatures, which is consistent with the work of Priya *et al.* [91]. However, the increase of T_m is not

always observed.[92] Meanwhile, the addition of nanoclay promotes crystallization of β-phase; similar promotion was also reported in PVDF composites with other inorganic fillers, for instance, BTO nanofibers,[93] functionalized BTO nanoparticles,[94] carbon nanotubes[95] and functionalized graphene sheet[96]. Considering such phase transformations, the change in the melting temperature is complicated. Values of melting temperature for α- and β-PVDF are not differentiated. Martins *et al.* [97] suggested that α- and β-PVDF showed indistinguishable melting temperature in the range of 167-172 ℃ while other researchers[88, 98, 99] believed that β-PVDF should have a higher melting temperature than α-phase due to the more densely packed all-trans chain conformation. To make things more complicated, Lanceros-Méndez group[100] reported the melting temperature of poled β-PVDF films, as 156.3 ℃, much lower than the common values for α-PVDF. For most PVDF composites, the formation of β-phase is not favoured by the addition of fillers,[101-104] which is actually beneficial for energy density of dielectric-based capacitors due to the inhibition of ferroelectric switching.[105, 106]

Apart from nucleation effects, the existence of inorganic fillers also influences the crystalline orientation of polymer matrices in the process of uniaxial stretching. He *et al.*[107] reported that the existence of organosilicate favoured the formation of β-PVDF during solid state drawing, which led to the improved piezoelectric and pyroelectric performance of PVDF/organosilicate composites. Coates and co-workers[108] reported the improved dielectric performance of solid-state oriented polypropylene (PP) /multiwalled carbon nanotube (MWCNT) nanocomposites, where the dielectric improvement arose from the orientation of MWCNT and the neighbouring molecular chains of PP. Todorov *et al.* [109] used in-situ WAXS and SAXS techniques to investigate

structural evolution mechanism for poly(ethylene terephthalate) (PET) composites with titanium dioxide (TiO_2) and silica (SiO_2) nanoparticles (0.3 wt. %). For both neat PET and PET composites, three stages are involved during the structural evolution (Figure 2.8): stage 1 is the evolution of amorphous region into mesophase before the occurrence of necking phenomenon, where the nanoparticles show stress concentrating effect; stage 2 is the formation of necking zone when the polymer molecular chains orient rapidly producing voids and cracks resulting from the debonding of the nanoparticles coupled with the quick increment of mesophase and the transformation from mesophase to periodical mesophase; stage 3 involves propagation of the necking zone along with elongation of voids and the final achievement of periodical mesophase. The role of nanoparticles is to facilitate the formation of periodical mesophase making it occur at an earlier stage and reach higher fraction compared to neat PET, thus contributing to more preferred orientation for PET composites.[109]

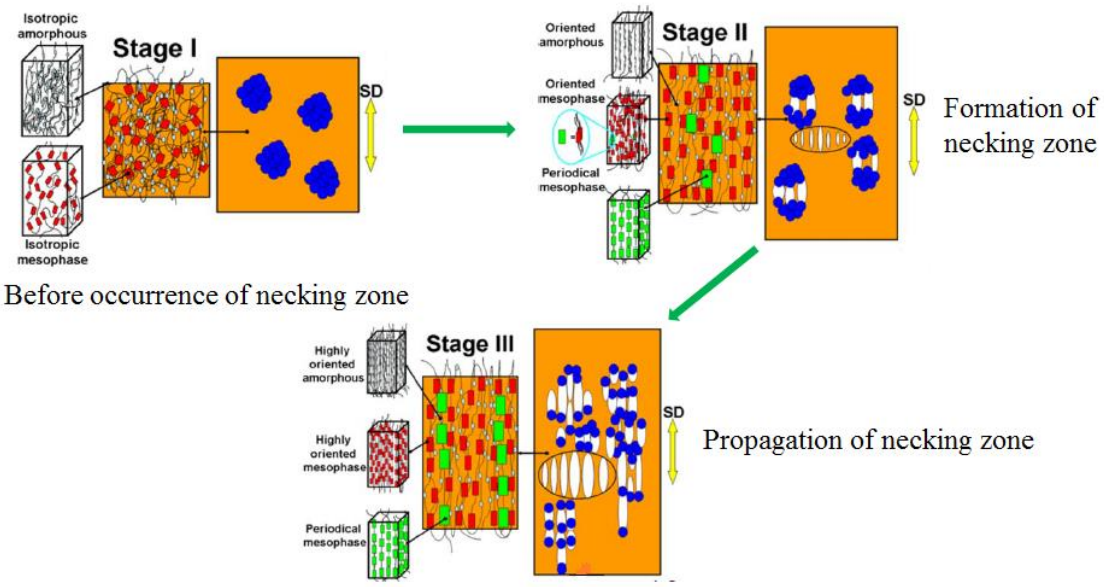

Figure 2.8 Schematic illustration of structure evolution during uniaxial stretching (reproduced from[109]).

To summarize, the crystallization process of PVDF is influenced by the inorganic fillers which act as nucleation agents facilitating the crystallization process and making the T_{cry} shift to higher temperature, and some specific fillers (for example, nanoclay) promote the crystallization of the β-phase. Meanwhile, the addition of inorganic fillers accelerates the formation of periodical mesophase and induces larger amounts of periodical mesophase, which improves the crystalline orientation of polymer matrices in the uniaxial stretching process.

2.4.2 Interfaces between polymer matrices and inorganic fillers

The interfaces between polymer matrices and inorganic fillers are strongly dependent on the surface area of inorganic fillers. Nano-scale fillers (at least one dimension is less than 100 nm) are selected to obtain greater surface area. Dang[106] put forward a representative model, filling a unit cube with smaller ones, to explain the effect of nano-scale fillers on the surface area (Figure 2.9). It is clearly seen that when the side length decreases from 10 μm to 5 nm, the surface area increases four orders of magnitude from 0.6 to 1200 m^2.

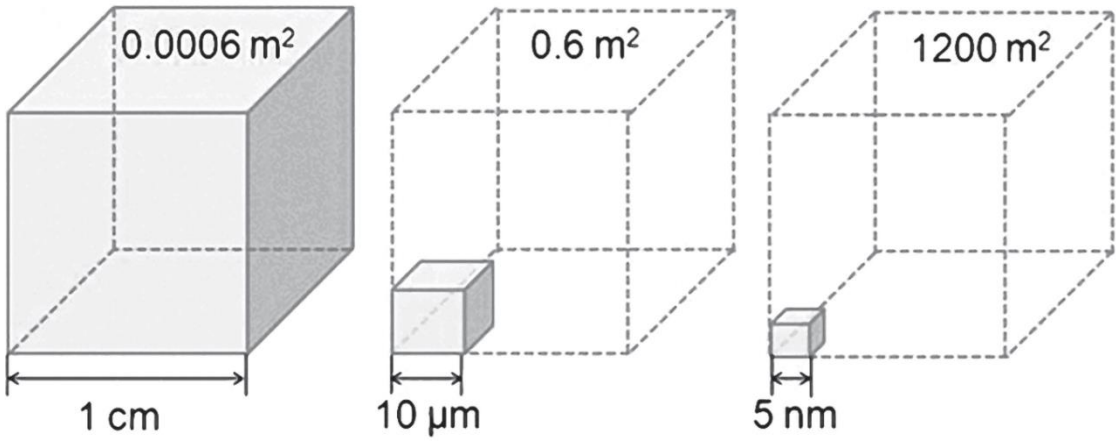

Figure 2.9 A schematic diagram for great surface area induced by the nano-scale fillers[106].

Due to the existence of greater surface area, the properties of interfaces are neither similar to the polymer matrices nor to the inorganic fillers. Tanaka[110] put forward a multicore model to describe interfaces based on the nanoparticles embedded in polymer matrices (Figure 2.10). In the multicore model, interfaces are made up by three layers, of which the nearest one to nanoparticles is the bonded layer. This layer bonds nanoparticles with polymer matrices tightly either through covalent, ionic or hydrogen bonds or van der Waals forces. The outside bonded layer is the bound layer where the polymer chains are connected to the bonded layer and the particle surface. Out of the bound layer is the loose layer which is loosely linked to the bound layer. In all these layers, including the loose layer, polymer chain mobility is different from the polymer matrices, which improves the properties of nanocomposites.

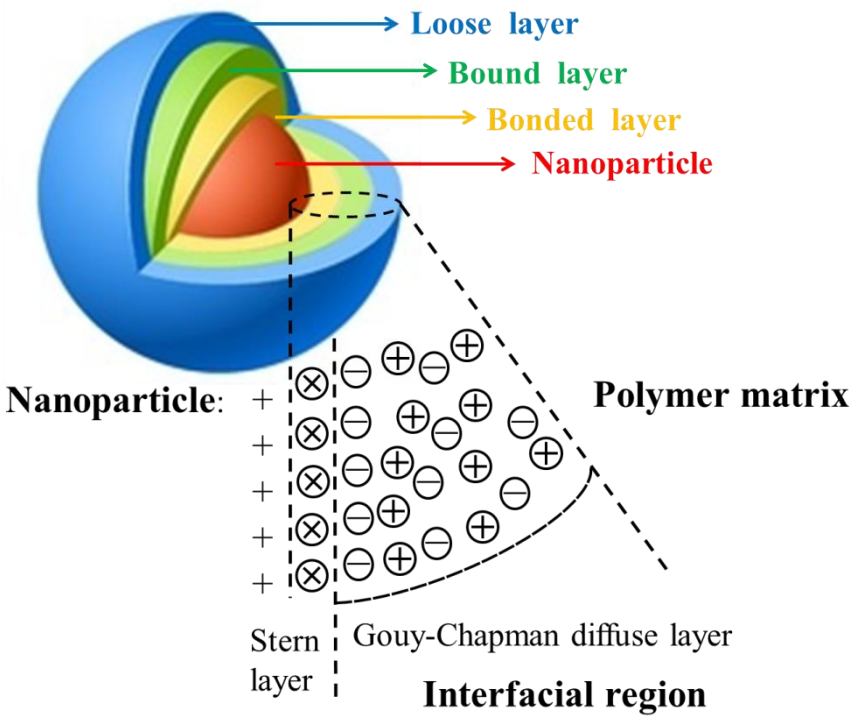

Figure 2.10 A schematic diagram of the multi-core model and corresponding distribution of injected charges for polymer nanoparticle composites (reproduced from[106, 110]).

Apart from chemical factors, electrical characteristics can also form the interfaces, as shown in Figure 2.10; whole interfacial region is marked as Gouy-Chapman diffuse layer.[110] Positive charged nanoparticles make the interfacial region form a diffuse electric layer covering all three layers defined by the chemical viewpoint (Figure 2.10). This diffuse electric layer can be driven by the polymer polarization; electronic polarization linked with the dipole motion and the permanent dipole orientation related to the molecular chain motion. For solid electrolyte polymers, mobile charges can also form the diffuse electric layer with positive and negative ions. Due to the different morphology and crystalline structure, the properties of interfacial region are quite different from both nanoparticles and polymer matrices, and considering the diffuse charge distribution layer, interfacial polarization can enhance or even dominate the dielectric properties for composites materials.[111]

2.4.3 Dielectric properties of ferroelectric polymer/inorganic fillers composites

Apart from the increased dielectric permittivity, high dielectric breakdown strength, defined by the maximum value of applied electric field without the occurrence of short-circuit, is also required for the energy storage application. Increasing the ratio of inorganic fillers is effective in achieving large dielectric permittivity, however, the high surface energy of inorganic materials results in the agglomeration and incompatibility with polymer matrices, inducing severe dielectric loss and poor dielectric breakdown strength.[112] Therefore, it is crucial to control the volume ratio of inorganic fillers (normally lower than 60 vol. %[113]) and, meanwhile, applying surface modification to inorganic fillers is effective in minimizing phase separation and particle aggregation.[114]

In addition, the size and shape of inorganic fillers also determine the properties of composites materials.[114, 115]

Surface modification of inorganic fillers

Ogitani *et al.* [116] employed phosphoric acid type surfactants to modify lead magnesium niobate-lead titanate (PMN-PT) and increased the dielectric constant of epoxy/PMN-PT (71 vol. %) from 43 to 70. However, the residual surfactants were detrimental to the dielectric properties; resulting in high dielectric loss and leakage current. Thus, binding surface modifiers to inorganic fillers via robust chemical bonds is favourable.[117, 118]

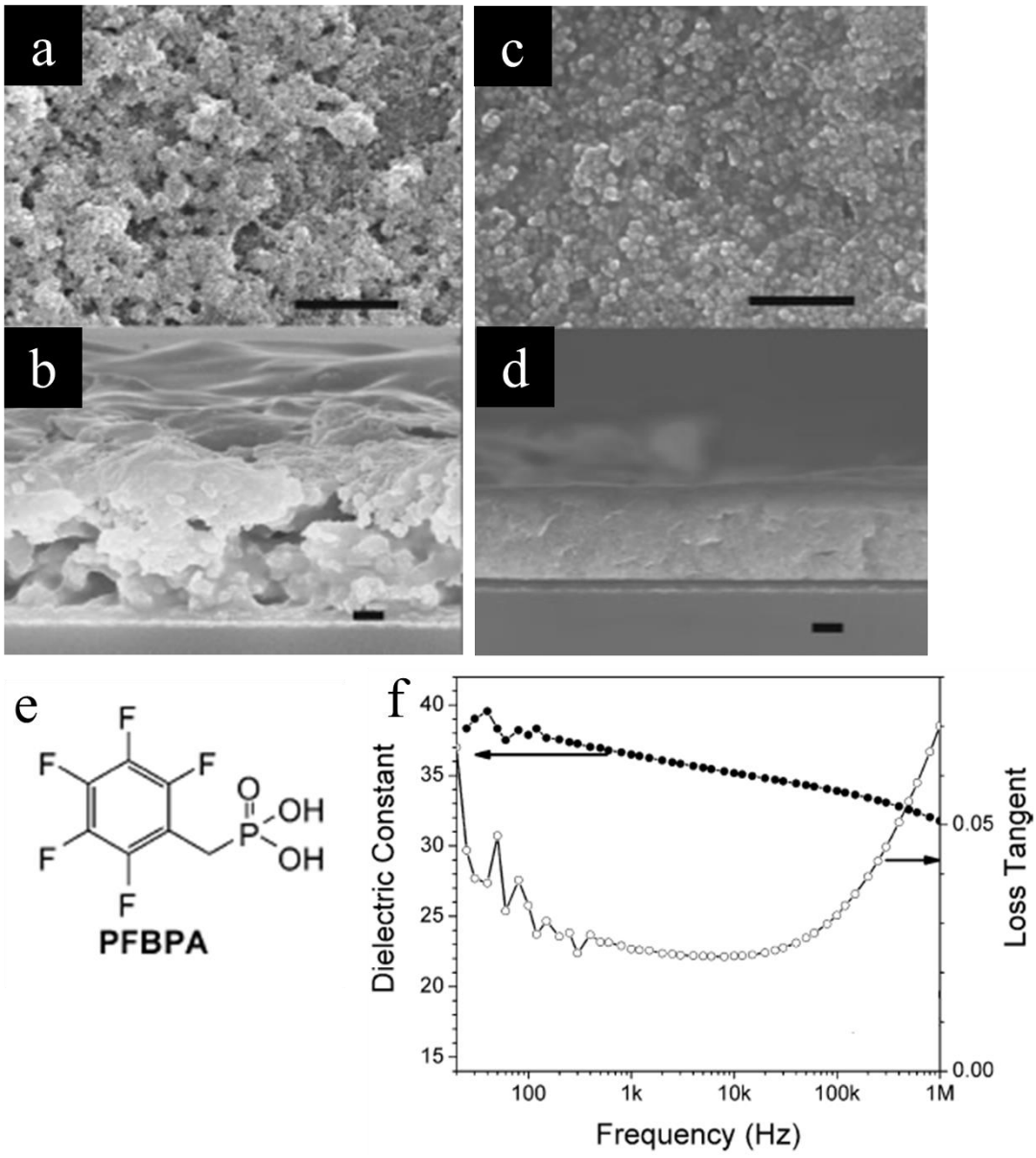

Figure 2.11 SEM images of surface and fractured cross-section for thin spin-coated nanocomposites films: (a, b) PVDF-HFP/BTO 50 vol. %; (c, d) PVDF-HFP/PFBPA-BTO 50 vol. %. All scale bars are 1 μm. (e) Molecular structure of pentafluorobenzyl phosphonic acid PFBPA that used to modify BTO in poly(vinylidenefluoride-hexafluoropropylene) PVDF-HFP matrix. (f) Dielectric frequency dependence of PVDF-HFP/PFBPA-BTO 50 vol. % nanocomposites thin films (reproduced from[118]).

As depicted in Figure 2.11, nanocomposites with unmodified BTO exhibit severe aggregation and defects while the ones with modified BTO are more uniform and

display much better BTO dispersion. As a result, even for 30-50 nm BTO fillers, PVDF-HFP/PFBPA-BTO 50 vol. % composites have large dielectric constant (ε_r=37 at 1kHz) and low dielectric loss (< 0.07). But a comparison of the dielectric properties induced by surface modification was not reported in this work. Zhou *et al.* [119] investigated such comparison, as shown in Figure 2.12, crude BTO nanoparticles (85-100 nm) (c-BTO) were surface hydroxylated using H_2O_2 (h-BTO); fractured cross-section of PVDF/h-BTO showed less holes due to the strong interaction between the filler and matrix. Composites loaded with hydroxylated BTO possessed lower dielectric constants than those loaded with c-BTO (Figure 2.12(d)), which was due to the smaller polarization resulting from the restricted chain mobility of PVDF/h-BTO composites due to the hydrogen bonds. Additianally, the dielectric loss of PVDF/h-BTO composites was lower than that of PVDF/c-BTO composites. Moreover, PVDF/h-BTO composites showed higher dielectric breakdown strength, which is consistent with PVDF/h-$Ba_{0.6}Sr_{0.4}TiO_3$ nanofiber composites,[120] whereas the dielectric constants of PVDF/h-$Ba_{0.6}Sr_{0.4}TiO_3$ composites increased compared with composites loaded with non-treated fillers; the authors linked such increase to the less air introduction arising from decreased defects. Despite the contradictary influence on dielectric permittivity, surface modification does promote the interaction between the fillers and polymer matrices, reducing the dielectric loss and increasing dielectric breakdown strength.

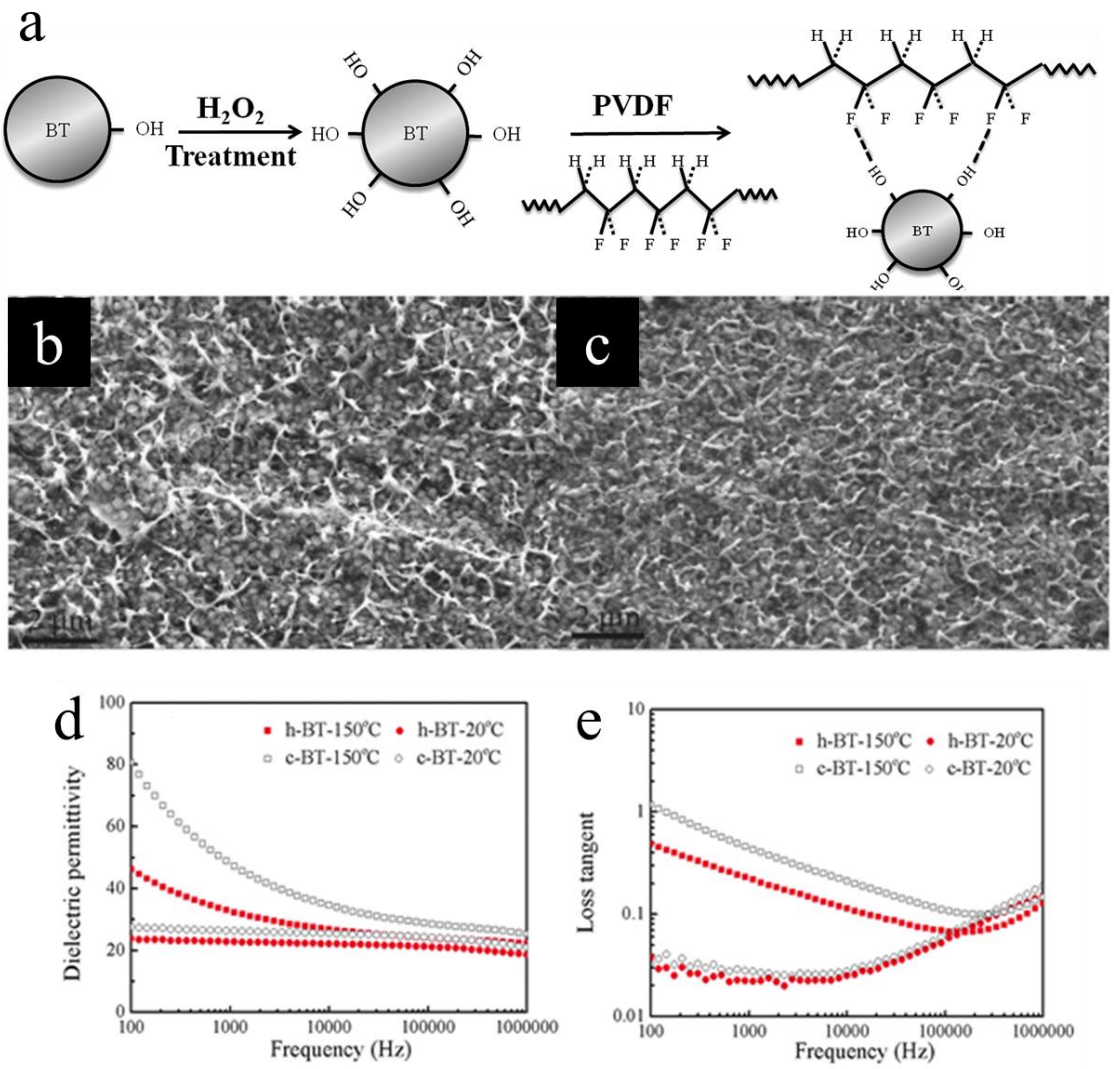

Figure 2.12 (a) Schematic diagram of BTO hydroxylation and the formation of hydrogen bond in PVDF/h-BTO composites; (b, c) fractured cross-section of PVDF/c-BTO and PVDF/h-BTO with 30 vol. % inorganic fillers; (d, e) frequency dependence of dielectric permittivity and loss tangent of PVDF/c-BTO and PVDF/h-BTO loaded with 30 vol. % inorganic fillers at different temperatures (20 and 150 °C) (reproduced from[119])

Size and shape of inorganic fillers

Interfacial area increases with decreasing particle size; however, ferroelectric particles show size dependence of polarization. As predicted by theoretical models,[121] the

ferroelectric polarization of BTO decreases gradually before reaching critical particle size (~ 100 nm) resulting from the phase transformation from tetragonal to cubic.

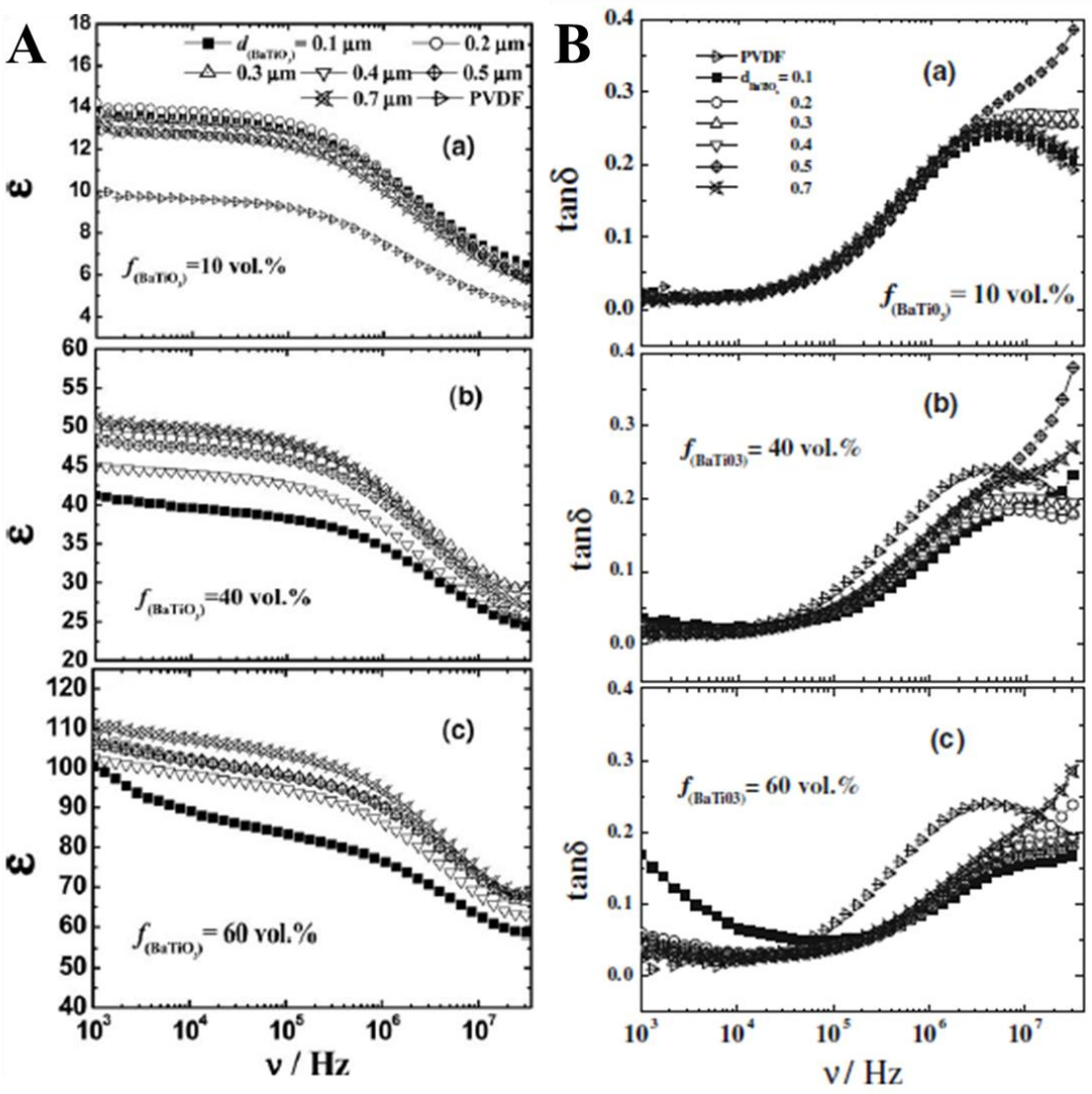

Figure 2.13 Dielectric frequency spectra of PVDF/BTO composites with different size (a) 10 vol.%; (b) 40 vol.%, (c) 60 vol.% (reproduced from[122])

Fu *et al.* [114] synthetized different grain sized BTO particles using molten-salt synthesis; P_r increased 0.18 to 0.28 C/m^2 corresponding to the increasing grain size from 400 to 600 nm. With regard to the size effect of binary PVDF/BTO composites, Dang *et al.* [122] reported that PVDF composites with 200 and 300 nm BTO exhibited larger ε' than

those with 400 and 500 nm BTO particles, meanwhile, BTO particle size makes little differences to the dielectric loss of composites (Figure 2.13).

As inorganic fillers, nanofibers with large aspect ratio have obvious benefits compared to nanoparticles. Larger dipole moments of fibre shaped fillers[123] enhance the dielectric properties of composites at lower volume ratio compared to those loaded with spherical fillers and are less detrimental to decreasing the dielectric breakdown strength [124]. Song *et al.* [125] compared the difference between epoxy based composites loaded with nanoparticles and nanofibers; as shown in Figure 2.14, composites loaded with nanofibers exhibit enhanced dielectric properties; higher dielectric permittivity, lower dielectric loss and higher dielectric breakdown strength.

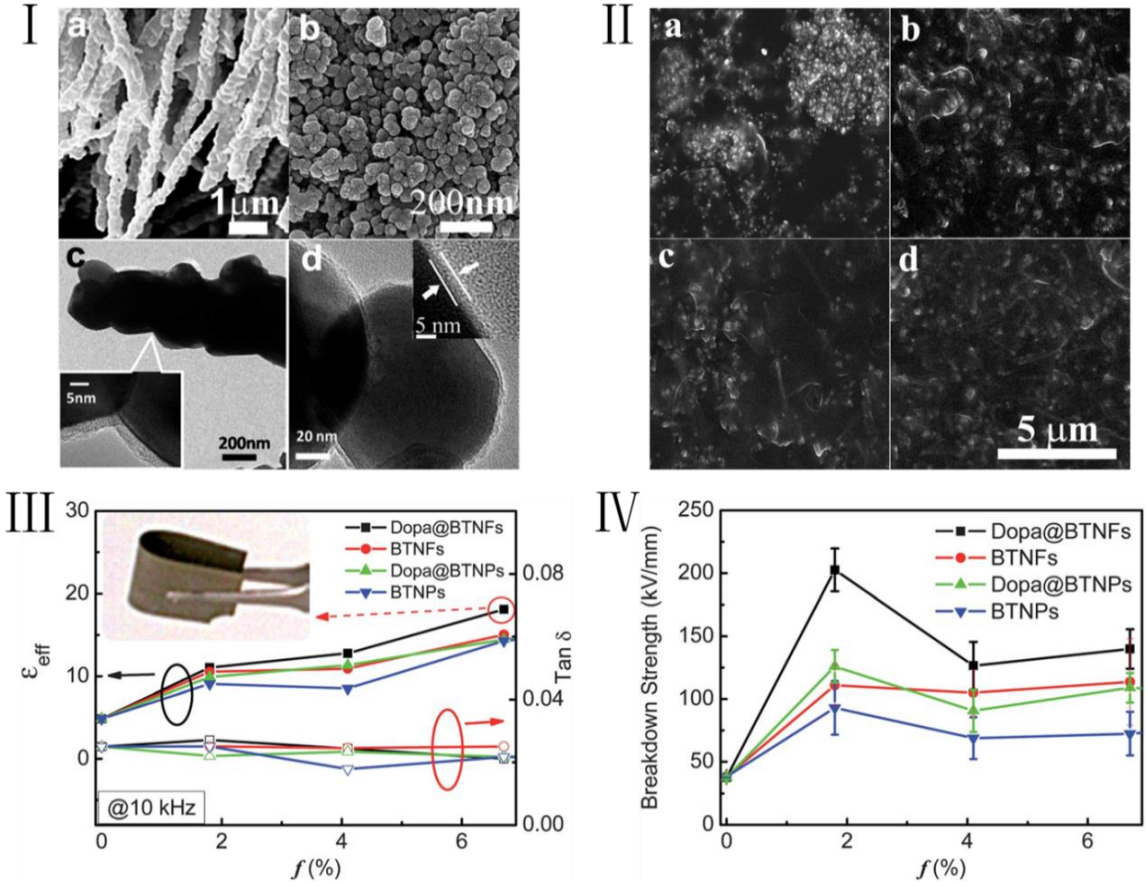

Figure 2.14 (I) SEM images of: (a) BTO nanofibers; (b) BTO nanoparticles; HRTEM images of (c) polydopamine modified BTO nanofibers Dopa@BTO nanofibers; (d) polydopamine modified BTO nanoparticles Dopa@BTO nanoparticles. (II) SEM images of fractured cross-sections for epoxy/BTO composites loaded with (a) unmodified BTO nanoparticles; (b) Dopa@BTO nanoparticles; (c) unmodified BTO nanofibers; (d) Dopa@BTO nanofibers. (III) Variations of dielectric constant ε_{eff} and loss tangent tanδ with the volume ratio of BTO inorganic fillers for epoxy based composites loaded with unmodified and polydopamine modified BTO nanoparticles and nanofibers; the inset demonstrates the flexibility of epoxy/Dopa@BTO nanofibers 6.7 vol. % composites. Figures are reproduced from[125].

Additionally, Figure 2.14 shows the combined effect of surface modification and morphology of inorganic fillers; composites loaded with dopamine modified fillers have slightly higher dielectric permittivity, lower dielectric loss and enhanced dielectric breakdown strength especially for the ones loaded with nanofibers. Figure 2.15 shows

the results of PVDF[125] and PVDF-TrFE[124] based composites with dopamine modified BTO nanofibers, Values of dielectric permittivity for PVDF and PVDF-TrFE based dopamine modified BTO nanofibers (11 vol. % and 10.8 vol. %, respectively) are twice as large as that of PVDF/10 vol. % BTO particles composites (Figure 2.13(a)) associated with the larger dipole moment of nanofiber and strong interaction between fillers and matrices due to the surface modification. In addition, the dielectric breakdown strength is maintained for PVDF and even enhanced for PVDF-TrFE.

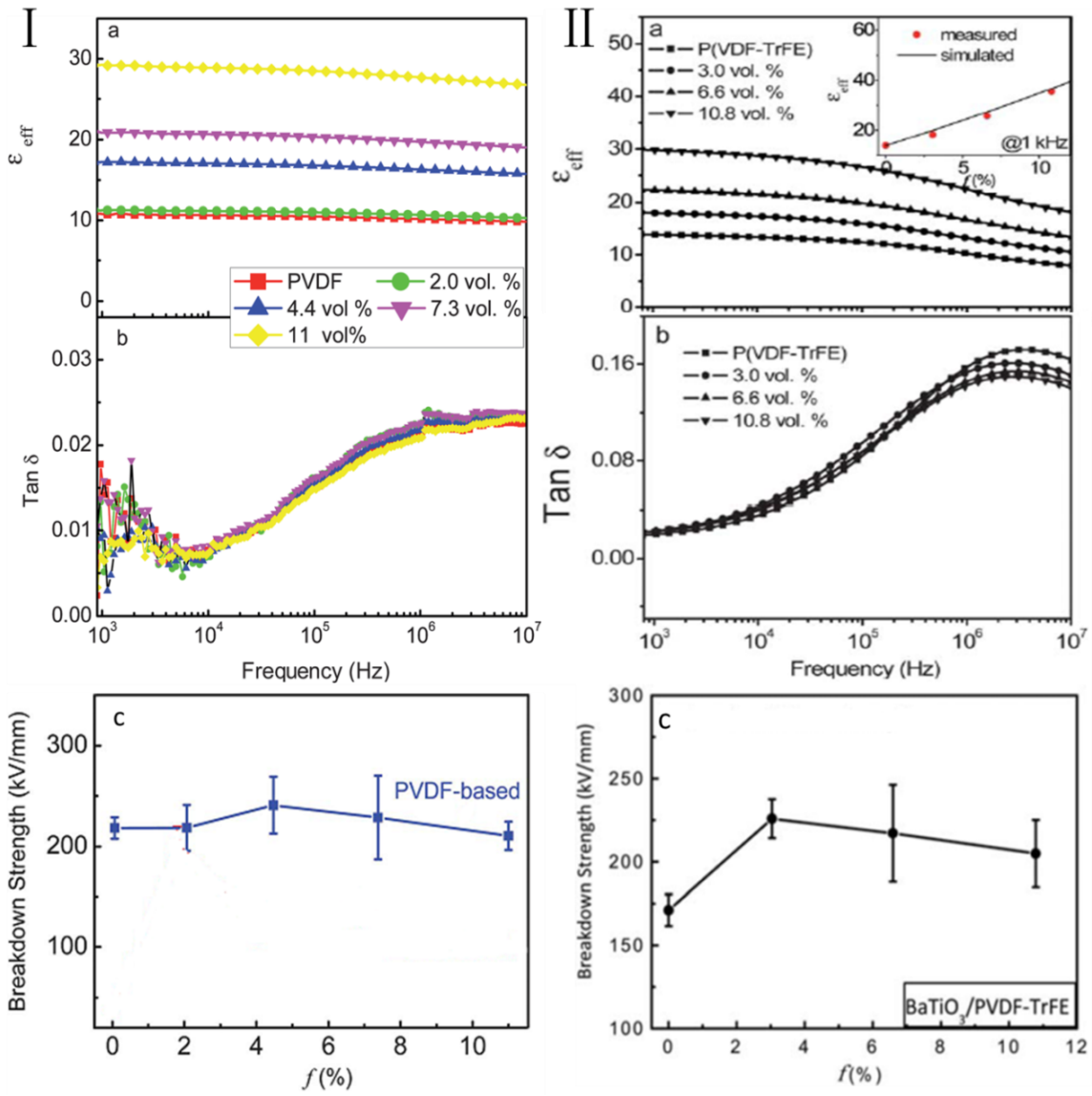

Figure 2.15 Dielectric properties of ferroelectric polymer/dopamine modified BTO nanofibers: (I) PVDF based[125]; (II) PVDF-TrFE based[124]: (a) dielectric permittivity frequency dependence ε_{eff}; (b) loss tangent frequency dependence tanδ; (c) dielectric breakdown strength as functions of volume fraction of fillers.

On account of application in the energy storage devices,[126-128] surface modification and morphology of inorganic fillers can be manipulated to enhance dielectric properties of polymer based composites. Due to the interactions between the fillers and matrices, as well as less agglomeration and defects, dielectric breakdown strength can be effectively

enhanced by surface modifying inorganic fillers. Fibre shaped fillers are more favourable to increase dielectric permittivity arising from the larger dipole moments.

2.4.4 Ferroelectric properties and enhanced energy storage of ferroelectric polymer/inorganic fillers composites

Electric capacitors are an important energy storage technology. Energy density (U_e) is crucial to the performance of electric capacitors, and is given by the relationship between the electric displacement (D) and electric field (E). Equation (1) shows the calculation of U_e, where E is the electric field and D_{max} is the electric displacement at highest electric field.[106]

$$Ue = \int_{Dmax}^{0} EdD \qquad 2.1$$

Figure 2.16 demonstrates *D-E* loops of four typical materials; linear dielectrics, ferroelectrics, relaxor ferroelectrics and anti-ferroelectrics, where the darker shaded area are the U_e. Linear dielectrics are featured for lower dielectric constants and high dielectric breakdown strengths; e.g. polyethylene (PE) ε'~ 2.4; U_e~ 2.25 J/cm^3 at 400 kV/mm,[129] biaxial-oriented polypropylene (BOPP) ε'~ 2.2; U_e~ 3.5 J/cm^3 at 600 kV/mm[130] and aromatic polyurea ε'~ 4.2; U_e~ 12 J/cm^3 at 800 kV/mm[131]. Compared to relaxor ferroelectrics, ferroelectrics are not promising candidates for energy storage devices, while the most suitable materials are anti-ferroelectrics. Details about energy storage will be discussed later.

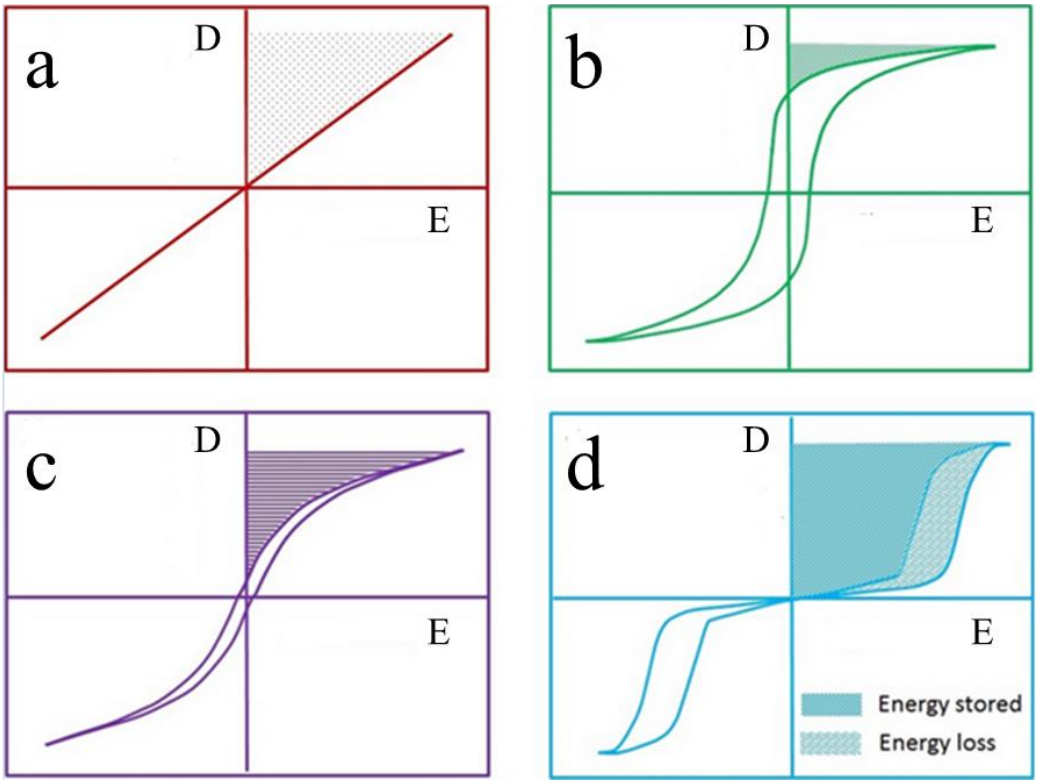

Figure 2.16 Demonstration of displacement (D) versus electric field (E) and corresponding energy storage characteristic for: (a) linear; (b) ferroelectric; (c) relaxor ferroelectrics; (d) anti-ferroelectric (figures reproduced from[132])

The ferroelectric response of composites is quite different from that of inorganic fillers arising from the hindering the of effective field by the surrounding low dielectric permittivity polymer matrices.[133] Values of remnant polarization P_r and saturated polarization P_{sat} increase significantly compared to the matrix phase due to the higher polarization of inorganic fillers (Figure 2.17).

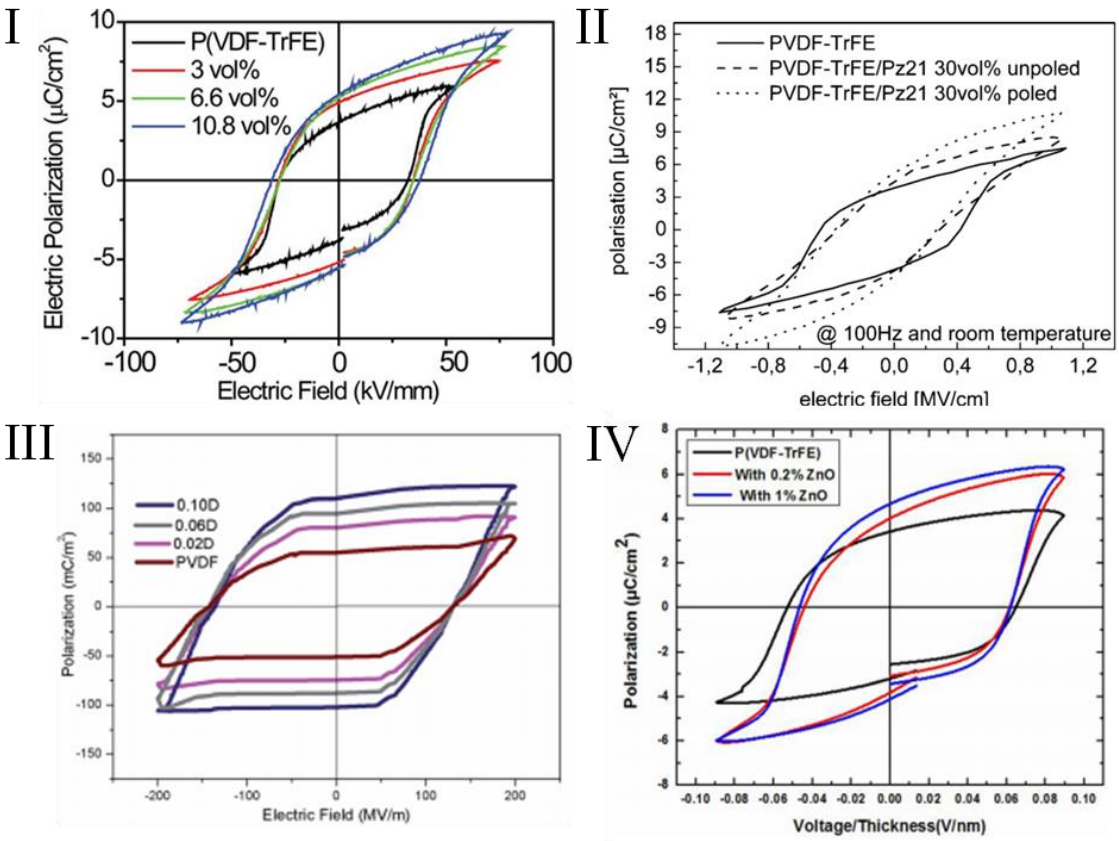

Figure 2.17 Ferroelectric enhancement arising from filler addition: (I) PVDF-TrFE loaded with dopamine modified BTO nanofiber[124]; (II) PVDF-TrFE loaded with PZT powders[134]; (III) PVDF loaded with diisopropylammonium bromide (DIPAB)[135]; (IV) PVDF-TrFE loaded with ZnO[136].

Notably increasing dielectric permittivity of composites materials makes them promising candidates for application in energy storage devices. In PVDF based composites, γ-phase is much more favourable compared to α- and β-phase.[137] Figure 2.18(a) shows *D-E* hysteresis loops for all three phases. The β-phase shows typical ferroelectric switching with high remnant polarization (about 0.04 C/m^2) and can only withstand electric field lower than 200 kV/mm, which hinders its maximum energy density. The α-phase, however, exhibited high energy loss at about 300 kV/mm arising from the phase transformation (Figure 2.18(e)). Impressively, the γ-phase can sustain

the electric field as high as 500 kV/mm and the corresponding energy density is 14 J/cm^3.

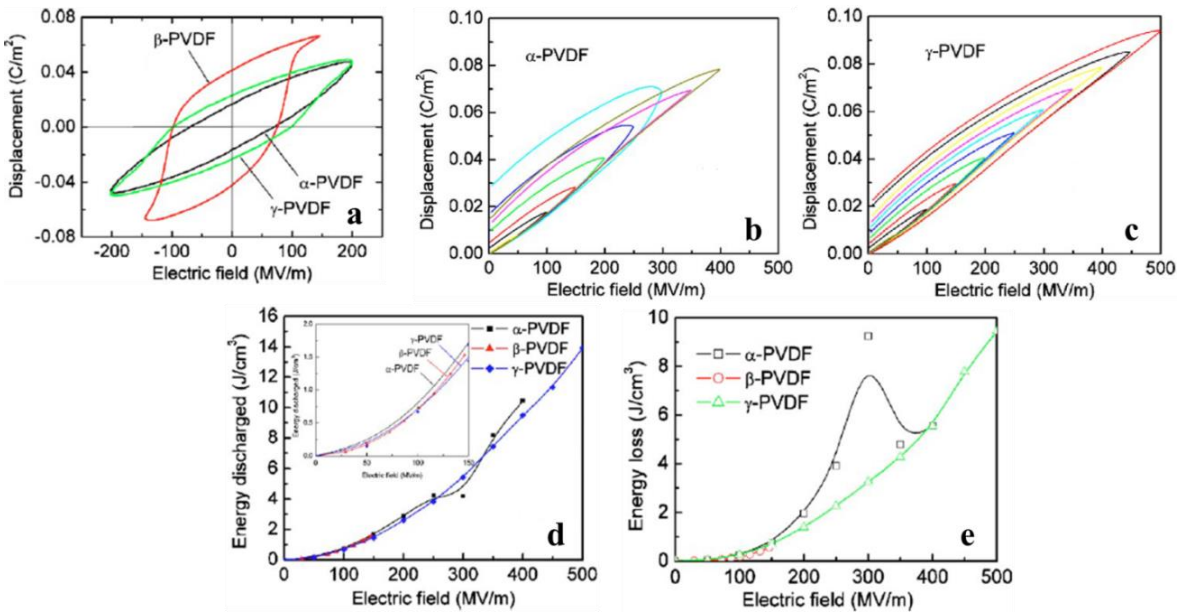

Figure 2.18 (a) D-E hysteresis loops for α-, β- and γ-phase; (b) unipolar D-E hysteresis loops for α-phase; (c) unipolar D-E hysteresis loops for γ-phase; (d) energy density for α-, β- and γ-phase; (e) energy loss for α-, β- and γ-phase (reproduced from[137])

Apart from crystalline phases, the crystal size and crystallinity are also crucial to energy density. Xia *et al.* [138] quenched PVDF-CTFE from 200 °C to different temperatures (70 °C-Q1, 25 °C-Q2, 0 °C-Q3, -94 °C-Q4 and -195 °C-Q5) attempting to fabricate films with various crystalline properties and energy storage density. It was found that crystalline size and crystallinity decreased with lowering quenching temperature; films quenched in liquid nitrogen (-195 °C-Q5) exhibited a reduced irreversible polarization due to the small crystallite size (Figure 2.19(a)). The size of crystal grains determined from polarized optical microscope for samples quenched in liquid nitrogen is about 4 μm, which is much smaller compared to 50 μm for samples crystallized at 70 °C. Meanwhile, quenching in liquid nitrogen (-195 °C-Q5) facilitated the saturated and

remnant polarization under AC field (Figure 2.19(b)), which arose from the fact that it was easier to pole the small crystallites.[138] Figure 2.19(c) also depicts the enhancement of dielectric breakdown strength. Films quenched in liquid nitrogen can withstand an electric field of 500 kV/mm. The dielectric breakdown strength of films crystallized at 70 °C is only 230 kV/mm. The high dielectric breakdown strength of samples quenched in liquid nitrogen is due to a low crystallinity. The crystallinity of samples quenched in liquid nitrogen and crystallized at 70 °C are 28.2% and 39.8%, respectively. Therefore, the reduction of crystalline size and crystallinity caused by quenching at low temperature was favourable to high dielectric breakdown strength and polarization. The energy density of PVDF-CTFE quenched in liquid nitrogen reached to 15.3 J/cm^3.

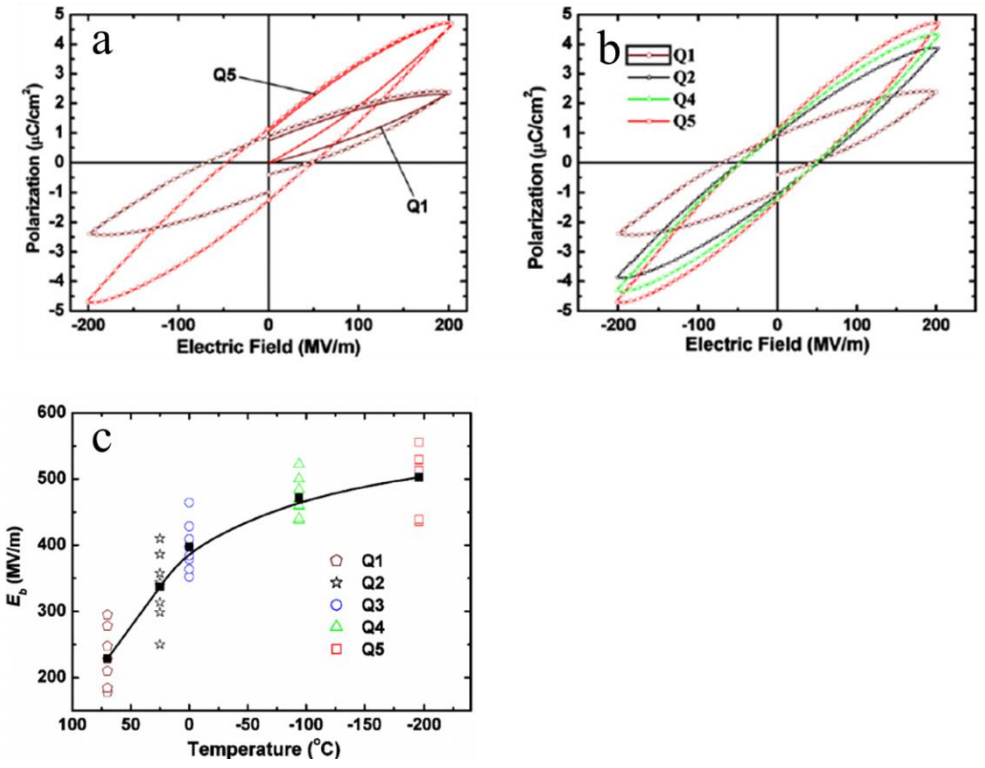

Figure 2.19 (a) Unipolar and bipolar P-E loops for PVDF-CTFE quenched at 70 °C and -195.8 °C; (b) hysteresis loops and (c) electric breakdown field for PVDF-CTFE quenched at different temperatures (reproduced from[138]).

Chapter 3 Experimental Procedure

This chapter describes the experimental techniques that were used to produce and characterize the ferroelectric films, including their functional properties.

3.1 Film preparation

The ferroelectric polymer films were produced using a DSM 15 ml X'plore micro compounder (MC 15) and then collected using an X'plore micro cast film line (Xplore Instruments, Geleen, The Netherlands), as shown in Figure 3.1. The micro compounder contains a liquid-tight and chemical resistant barrel and vertically positioned detachable twin screws, providing good mixing of polymer melt and fine dispersion of fillers. The processing temperature can be precisely controlled by six separate heating zones. During processing, the polymer powders or pellets were firstly filled into the barrel and heated above the melting points of the polymers. The melt was then extruded through a die and collected on a roller at set speeds.

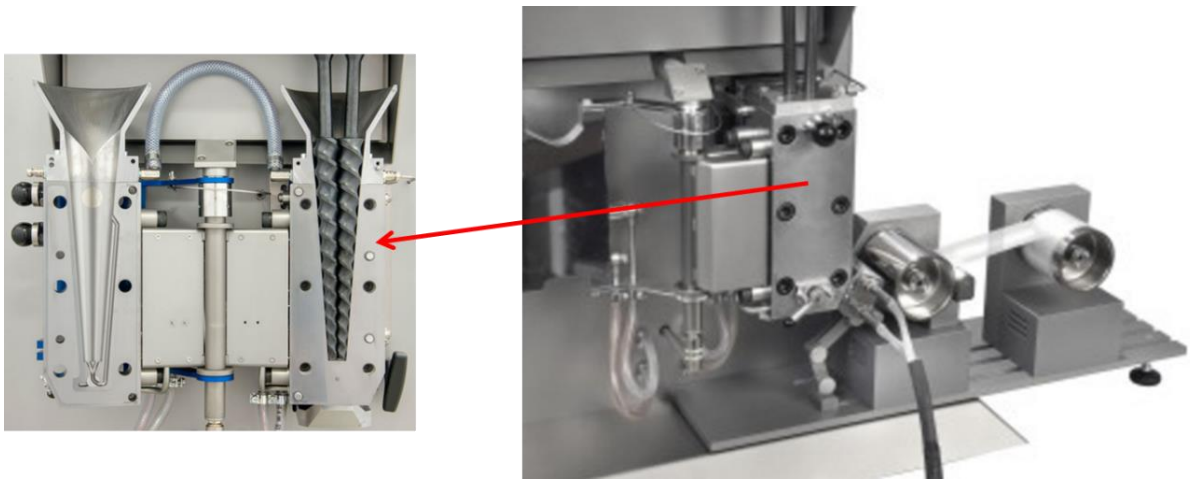

Figure 3.1 Micro compounder and cast film line (Xplore Instruments, Geleen, The Netherlands, pictures are referred on[139]).

3.2 Characterization

3.2.1 Crystalline structure and phase determination

X-ray diffraction (XRD)

XRD a common technique used to determine the crystalline phases in a material. The data is analysed using Bragg's laws $n\lambda=2dsin\theta$, where n is an integer; λ is the wavelength of X-ray beam; d is the distance between two parallel crystal planes; θ is the angle between the X-ray beam and scattering lattice planes. Figure 3.2 shows the diffractions of X-ray from three crystal planes. s_o and s represent the incident and reflected X-ray beams, respectively. The path differences between waves reflected by each continuous pair of planes are $2dsin\theta$, and equal to some integral multiple of X-ray wavelength $n\lambda$ when the Bragg condition is satisfied.

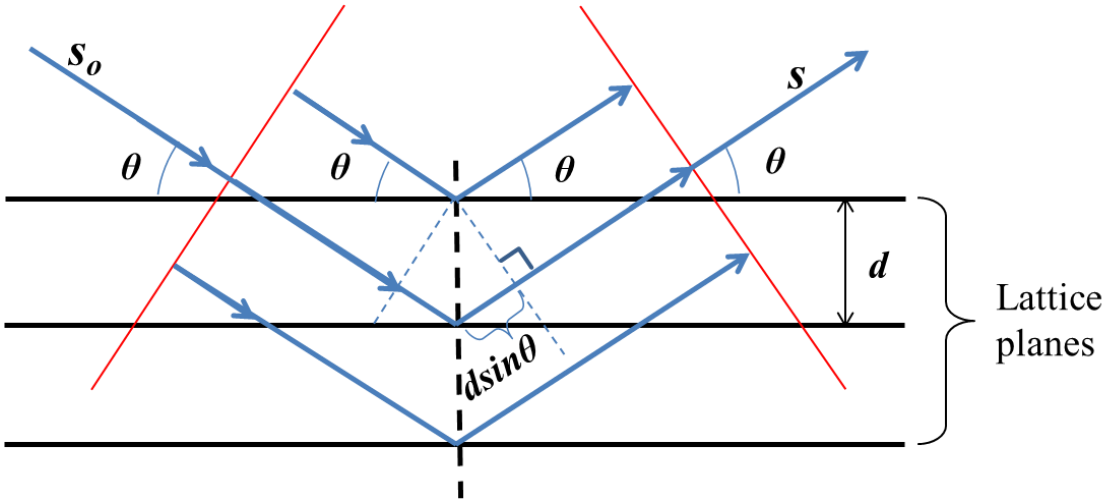

Figure 3.2 Diffraction of X-rays considered as reflection from a set of lattice planes.

In this work, the XRD diffraction patterns were collected using a reflection Bragg-Brentano θ-θ geometry X-ray diffractometer (X'Pert Pro, PANalytical, Almelo, The

Netherlands) with Cu/Kα radiation (λ=1.5418 Å) in the 2θ range of 5°-70°. During testing, the position of samples is fixed, while the tube and detector rotate at rates of -θ°/min and +θ°/min, respectively. The angle between the tube and the detector is 2θ.

Fourier transform infrared spectroscopy (FTIR)

FTIR was performed on a Tensor 27 spectrometer (Bruker Optik GmbH, Ettlingen, Germany) with a platinum attenuated total reflectance (ATR) accessory. The acquired absorbance bands are attributed to specific molecule vibrations that linked to the chain conformations of polymers, and different chain conformations lead to different crystalline phases, thereby FTIR can be used to distinguish the crystalline phases of PVDF based polymers and complement the XRD data. The FTIR scans were performed with 32 scans for one sample and a resolution of 4 cm^{-1} in the wavenumber range of 4000-400 cm^{-1}.

3.2.2 Crystalline preferred orientation

The diffraction patterns used to characterize the crystalline orientation are composed of continually azimuthal intensity distribution along the direction denoted by ψ in Table 3.1 (χ in Figure 3.4), which requires intense diffraction from at least two sets of crystal lattice planes. Typical diffraction patterns and related structure factors are depicted and summarized in Figure 3.3 and Table 3.1, respectively. The radial direction represents the spacing of crystal planes, and the length of the diffraction arcs reflects the crystalline orientation. The shorter the diffraction arcs, the higher the degree of crystalline orientation (b in Figure 3.3).

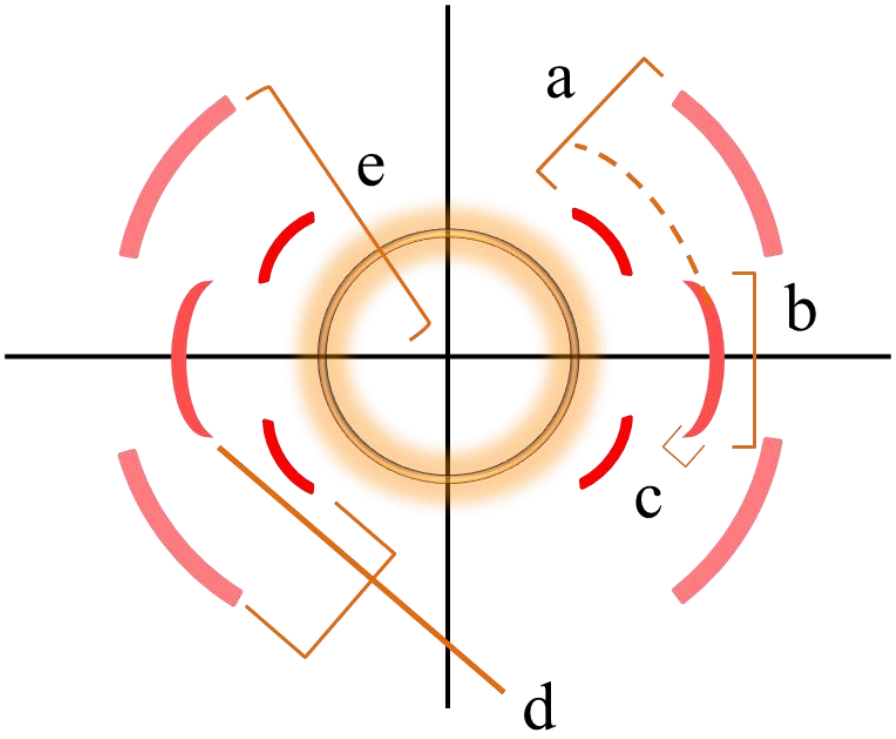

Figure 3.3 Diffraction patterns for polymer samples with marked typical characteristics (Figure reproduced from[140]).

Table 3.1 Possible features of crystalline structure that related to the marked characteristics in Figure 3.3 (Table reproduced from[140])

Characteristics of diffraction patterns	**Possible features of crystalline structure**				
	Distortion of crystal lattice	Pronounced thermal vibration of atoms, etc.	Degree of orientation	Small sized crystallites	Amorphous regions
a) Change in Bragg spacing	★★★			★	
b) Arc length of reflections (ψ)			★★★		
c) Line broadening (2θ)	★★	★		★★★	
d) Rapid decrease in intensity at large angles	★★	★★			
e) Intense background scattering	★	★			★★

The crystalline preferred orientation of films was characterized using two-dimensional wide-angle X-ray diffraction (2D-WAXD) ring patterns, which were obtained on a transmission geometry single crystal X-ray diffractometer (Kappa ApexII Duo, Bruker AXS GmbH, Karlsruhe, Germany). Two sources, Molybdenum and Copper, exist on one goniometer, which can be switched. This diffractometer uses 4-circle goniometers (Figure 3.3), $2\theta, \chi, \varphi, \Omega$, defining the relationship between lattice plane, incident X-ray

and the detector. The samples can be flexibly positioned, adjusting the centre region with the X-ray beam.

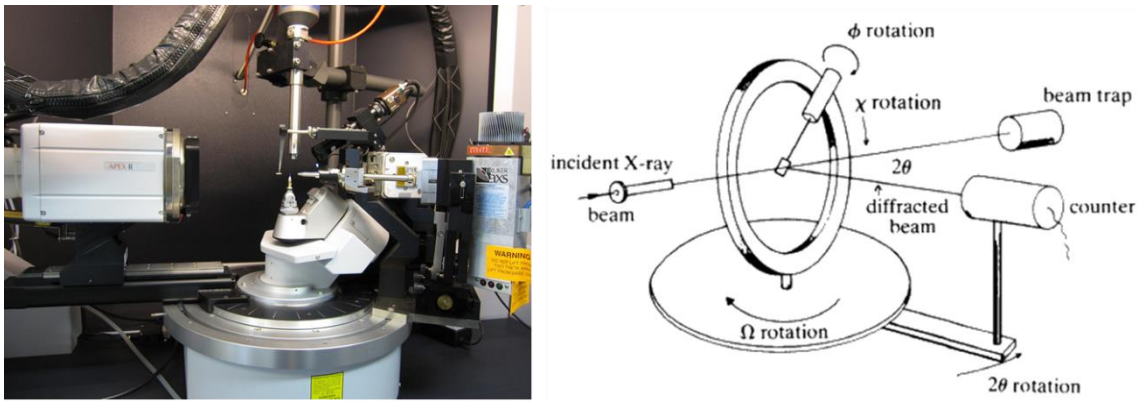

Figure 3.4 Bruker AXS Kappa ApexII Duo diffractometer and schematic diagram of 4-circle goniometers.

The Herman's orientation factor (*f*) is used to quantify the orientation degree. In Figure 3.5, the *Z*-axis is the reference direction and the angles made by a-, b-, and c-axis of the crystallite with the *Z*-axis are φ_a, φ_b and φ_c, respectively. The orientation factor, f_a, f_b and f_c represent the orientation degree of a-, b- and c-axis with respect to *Z* axis are calculated using the following Equation 3.1.

$$f_a = (3 < cos^2\varphi_a > - 1)/2$$

$$f_b = (3 < cos^2\varphi_b > - 1)/2$$

$$f_c = (3 < cos^2\varphi_c > - 1)/2 \qquad 3.1$$

The $<\cos^2\varphi_a>$, $<\cos^2\varphi_b>$ and $<\cos^2\varphi_c>$ are defined by the following Equation 3.2.

$$< cos^2\varphi_a >= cos^2\theta_{h00} < sin^2\psi_{h00} >$$

$$< cos^2\varphi_b >= cos^2\theta_{0k0} < sin^2\psi_{0k0} >$$

$$< cos^2\varphi_c >= cos^2\theta_{00l} < sin^2\psi_{00l} > \qquad 3.2$$

The $<\sin^2\psi_{h00}>$, $<\sin^2\psi_{0k0}>$, and $<\sin^2\psi_{00l}>$ are given by

$$< sin^2\psi_{h00} >= \frac{\int_0^{\pi/2} I(\psi_{h00})\, sin^2\psi_{h00} cos\psi_{h00} d\psi_{h00}}{\int_0^{\pi/2} I(\psi_{h00})\, cos\psi_{h00} d\psi_{h00}}$$

$$< sin^2\psi_{0k0} >= \frac{\int_0^{\pi/2} I(\psi_{0k0})\, sin^2\psi_{0k0} cos\psi_{0k0} d\psi_{0k0}}{\int_0^{\pi/2} I(\psi_{0k0})\, cos\psi_{0k0} d\psi_{0k0}}$$

$$< sin^2\psi_{00l} >= \frac{\int_0^{\pi/2} I(\psi_{00l})\, sin^2\psi_{00l} cos\psi_{00l} d\psi_{00l}}{\int_0^{\pi/2} I(\psi_{00l})\, cos\psi_{00l} d\psi_{00l}} \qquad 3.3$$

Here, $I(\psi_{h00})$, $I(\psi_{0k0})$, $I(\psi_{00l})$ are the intensity distributions of the h00, 0k0 and 00l diffractions on the ring patterns, θ_{h00}, θ_{0k0} and θ_{00l} are the Bragg angles for the h00, 0k0 and 00l diffractions. ψ is the angle from the equator measured on the ring patterns.

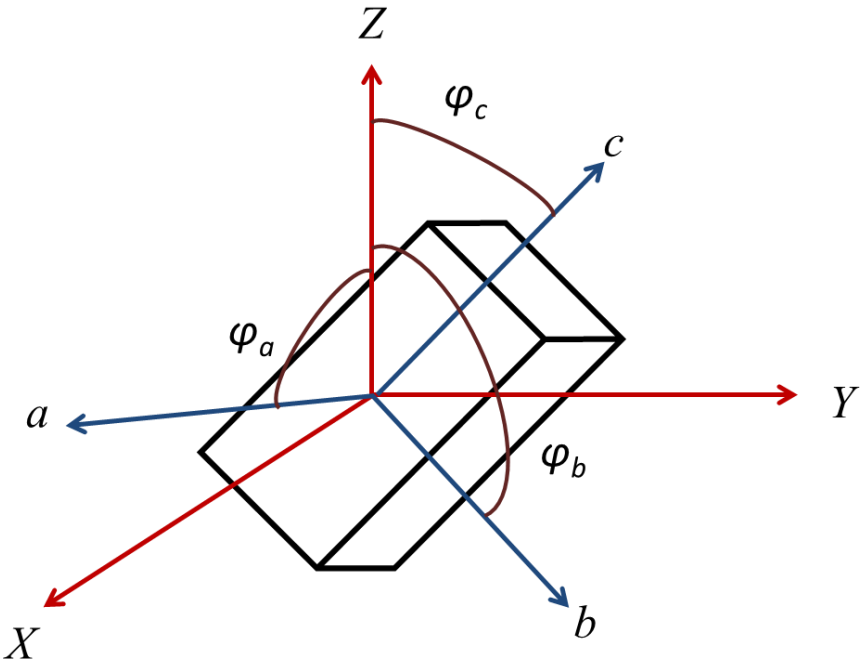

Figure 3.5 Parameters used to describe the calculation of Herman's orientation factor.

In this work, the 2D-WAXD ring patterns were analysed using FIT 2D software (European Synchrotron Radiation Facility, Grenoble, France) to obtain the azimuthal intensity plots, which were then fitted using a Gaussian function. The f_c was calculated from the Gaussian fitting plots and was used to quantitatively determine the degree of preferred orientation of polymer chain axes. If all of the polymer chains are ideally oriented along the reference direction, then $\varphi = 0°$ and $f = 1$. On the contrary, if all polymer chains are perpendicularly oriented with respect to the reference direction, then $\varphi = 90°$ and $f = -1/2$. In the case of random orientation, f will be equal to 0. The extrusion or the drawing direction was chosen as the reference direction.

3.2.3 Morphology characterization

The morphology of the gold coated samples was studied using a scanning electron microscopy (SEM) (FEI Inspect-F, Hillsboro, OR, USA). An SEM image is formed by the secondary electrons emitted from the samples due to the atom ionization under the primary beam electrons. For side and cross-section morphology, the samples were embedded in a resin. The resin blocks were pre-cracked and then cold fractured in liquid nitrogen.

3.2.4 Thermal analysis

Thermal properties of the films were characterized using a differential scanning calorimetry (DSC) (DSC4000, PerkinElmer, Massachusetts, USA). All samples were heated from 25 ℃ to 180 ℃ under a N_2 atmosphere, and the heating and cooling rates were 5 ℃/ min. From the DSC data, melting (T_m) and crystallization temperatures (T_{cys}) as well as the corresponding enthalpies (ΔH_m and ΔH_{cys}) can be determined. The crystallinity of one polymer is calculated by normalizing the measured ΔH_m value to that of the value for the same polymer with 100% crystallinity. The ΔH_m values for 100% crystalline PVDF and PVDF-TrFE are reported to be 104.6 J/g[141] and 38 J/g[142], respectively. The values of the characteristic temperature and thermodynamic parameters presented in this thesis are the average for 6 specimens.

3.2.5 Functional properties characterization

Dielectric properties

The frequency dependence of dielectric constant and dielectric loss tangent were measured using a Precision Impedance Analyser (4294A; Agilent, CA, USA) at ambient temperature in the frequency range of 100 Hz to 100 MHz with an applied maximum voltage of 0.5 V. The temperature dependence of dielectric properties was measured using an LCR meter (4284A; Agilent, CA, USA) which was connected to a homemade furnace. The electrode diameter for dielectric tests was 5 mm.

Ferroelectric properties

The ferroelectric P-E hysteresis loops were tested using a ferroelectric hysteresis measurement tester (NPL, Teddington, UK) at ambient temperature and 10 Hz. The electrode diameter for ferroelectric tests was 2 mm. Both the dielectric and ferroelectric data presented in this thesis were based on the testing of 8 different specimens.

Chapter 4 Influence of Extrusion Parameters and Drawing Condition on the Phase Transformation from Non-ferroelectric to Ferroelectric PVDF

4.1 Introduction

As stated in Chapter 2, PVDF has multiple phases (α-, β-, γ-, and δ-); the β-phase is the most favourable ferroelectric phase. Uniaxial drawing the α-phase is a common method to produce the β-phase. Table 4.1 shows the optimum drawing conditions reported in the literature. No consensus was reached on the ideal drawing condition for α to β phase transformation of PVDF. For example, drawing at a temperature of 155 °C without yielding did not develop β-phase;[143] a similar conclusion was made by Li *et al.* [144]. However, in the work of Vijayakumar *et al.* [145], almost complete phase transformation occurred even at a drawing temperature of 145 °C. This difference is due to the higher draw ratio of the latter work (6.4) compared to the former ones (~ 3). Compared to the drawing temperature and drawing rate, the draw ratio determines the formation of β-phase to a larger extent; at a temperature below 120 °C, a draw ratio of 3 can produce a fair amount of β-phase (~ 60 wt. %); a larger draw ratio (> 6) is needed if the drawing temperature is higher than 120 °C. At constant drawing temperature and draw ratio, the drawing rate makes almost no difference to the formation of β-phase.[144]

Table 4.1 Reported drawing condition for the phase transformation of PVDF.

Reference	Drawing condition_ draw ratio	Fraction of β-phase
Sajkiewicz *et al.* [146]	87 °C_ 138 mm/min_ 3.2	55 wt. %
Andre´-Castagnet *et al.* [147]	90 °C_ 5 mm/min_ 3.5	72 wt. %
Fang *et al.* [148]	25 °C_ 0.1 mm/min_ 2	Not mentioned; no α-phase peaks in XRD
Vijayakumar *et al.* [145]	65 °C_ 55.5 mm/min_ 4	74 wt. %
	145 °C_ 55.5 mm/min_ 6.4	98 wt. %
Li *et al.* [144]	100 °C_ 3 mm/min_ 3	95 wt. %
Ye *et al.* [149]	80 °C_ 10 mm/min_ 4	92 wt. %

The mechanism of the formation of β-phase during uniaxial drawing has been investigated using in-situ small-angle X-ray scattering (SAXS) and wide-angle X-ray scattering (WAXS).[150, 151] The characterization by SAXS focuses on the lamella crystals, while WAXS detects the level of crystalline block unit cell.[152] The original crystalline lamellae can be broken into smaller segments and elongated along the drawing direction, which results in mechanical yield and the orientation of the polymer chains. The phase transformation starts at the yield point as well as the formation of a fibrillar structure.[143, 150] Cavities or micro-voids can be formed during drawing.[153] Based on the reported work,[151] cavitation plays a role in the phase transformation when drawing PVDF at low temperatures (e.g. 60 °C), while at a higher temperatures (e.g. 140 °C) the phase transformation is more related to the orientation of lamellae.

In this chapter, the PVDF was firstly processed by melt extrusion at various conditions followed by uniaxial drawing. The effects of extrusion parameters as well as the drawing condition on the crystallization, crystalline orientation, thermal properties and functional properties of PVDF were investigated.

4.2 Experimental details

PVDF pellets were purchased from Sigma Aldrich Chemical Co. The average molecular weight of the PVDF was about 180 kg/mol (M_w) and 71 kg/mol (M_n) according to the supplier.

The extrusion processing conditions of the PVDF films are listed in Table 4.2. The β-phase is usually processed by solid-state drawing. The melt draw down during extrusion might have an effect on the crystallization of PVDF, which was studied using conditions 2-6. The extrusion temperature of 210 °C, about 40 °C higher than its melting point, can generate good chain mobility, which is suitable for producing films. Conditions 1 and 2 were used to study the effect of melting time.

Table 4.2 The Extrusion parameters for processing PVDF.

Extrusion condition	Temperature (°C)	Screw speed (rad)	Film collecting speed (a. u.)	Melt time (min)
1	210	100	500	15
2	210	100	500	8
3	210	100	350	8
4	210	100	750	8
5	210	75	750	8
6	210	75	1000	8

Samples of dimensions 45 mm×15 mm were cut from the PVDF films extruded under condition 3, which have a thickness ~ 45 μm. The samples were then drawn in a temperature controlled chamber attached to an Instron 5900R84 machine. The influence of drawing temperature was investigated at a constant cross head speed of 10 mm/min at 80, 100 and 120 °C, and the drawing rate effect was studied at 100 °C at 5, 10, 25 and 50 mm/min. The draw ratio of the drawn films was calculated using the following equation:

$$\text{Draw ratio} = \frac{\text{Extension}}{\text{Original length}} \qquad \mathbf{4.1}$$

4.3 Results and discussion

4.3.1 Effect of extrusion parameters on the crystallization of PVDF

Figure 4.1 shows the FTIR spectra for the as-extruded PVDF films under different conditions. All of the samples exhibited similar bands, which are listed in Table 4.3 along with the corresponding vibration mode. The bands shown in Figure 4.1 are characteristic α-phase bands. A typical β-phase band is at 840 cm^{-1}, which is assigned to the combined vibration of CH_2 bond rocking $r(CH_2)$ and CF_2 bond asymmetric stretching $\nu_a(CF_2)$. All of the extruded PVDF films showed very weak 840 cm^{-1} band, which suggests the PVDF principally crystallized into α-phase regardless of extrusion condition.

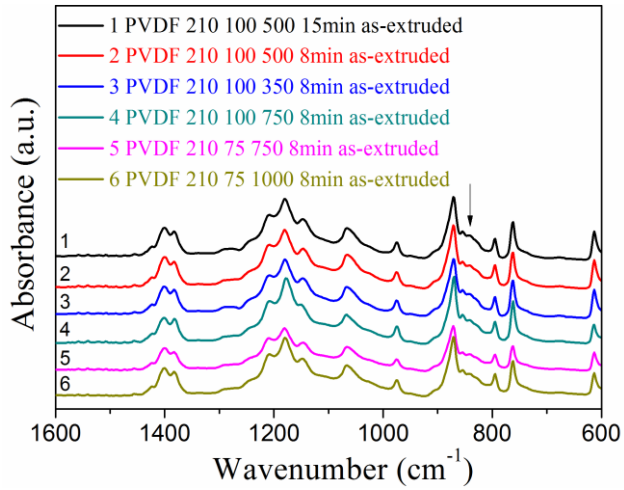

Figure 4.1 FTIR spectra for the as-extruded PVDF films under condition listed in Table 4.1.

Table 4.3 The characteristic bands and corresponding vibration modes and crystalline phase of as-extruded and annealed PVDF films.

Band (cm^{-1})	Vibration mode	Crystalline phase
974	*$\tau(CH_2)$	α
871	*$\nu_a(CC)+\delta(CCC)$	α
854	*$\gamma(CH_2)$	α
796	$\gamma(CH_2)$	α
761	$\delta(CF_2)$-$\delta(CCC)$	α

*$\boldsymbol{\tau}$, twisting; $\boldsymbol{\nu_a}$, asymmetric stretching; $\boldsymbol{\delta}$, bending; $\boldsymbol{\gamma}$, rocking vibration

4.3.2 Effect of thermal drawing conditions on the phase transformation of PVDF

Figure 4.2 shows the XRD patterns for the as-extruded (extruded under condition 3) and drawn PVDF films. The allowed X-ray diffraction peaks and the corresponding diffraction crystal planes are listed in Table 4.4.

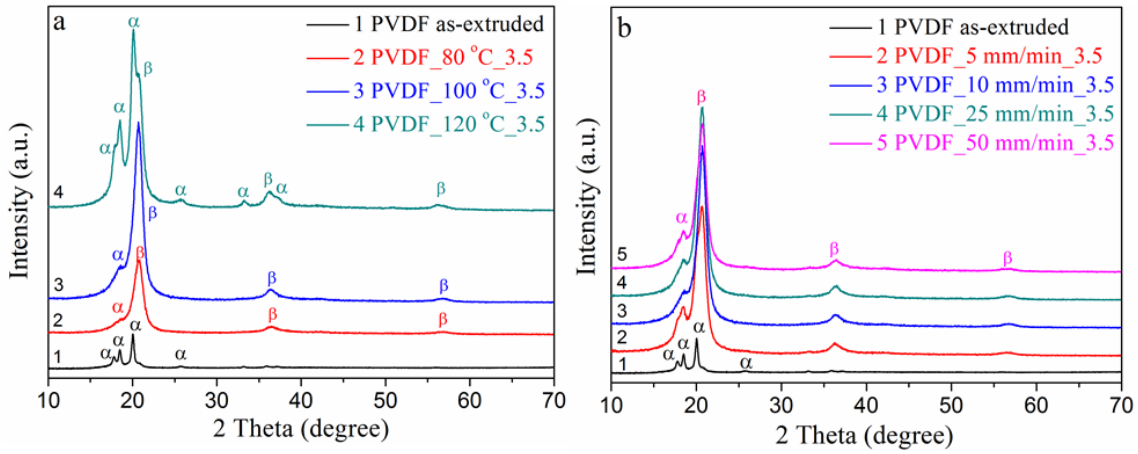

Figure 4.2 XRD patterns for: (a) as-extruded and drawn PVDF films at 10 mm/min but different temperatures 80, 100 and 120 °C; (b) as-extruded and drawn PVDF films at 100 °C

but different drawing rates 5, 10, 25 and 50 mm/min. The as-extruded PVDF films were produced using condition 3 in Table 4.2.

Table 4.4 Typical X-ray diffraction for PVDF reported in literature

	Crystal plane	**2θ (°) -Reference data** [12, 154-159]
α- PVDF	(100)	17.88
	(020)	18.40
	(110)	20.13
	(120)	25.77
	(021)	26.73
	(130)	33.20
	(200)	36.20
	(210)	37.44
β- PVDF	(110)/(200)	20.80
	(020)/(101)	36.50
	(221)	56.50
γ- PVDF	(101)	20.30

Characteristic XRD peaks of α-PVDF, 17.7° (100), 18.5° (020), 20.0° (110) and 25.7° (120) were clearly apparent in the XRD patterns of the as-extruded PVDF films (Figure 4.2a, b). The XRD patterns of the drawn PVDF films showed strong drawing

temperature dependence. Films drawn at the low temperatures, 80 and 100 °C, exhibited a strong β-phase peaks at 2θ=20.8°, which is reflected by (110)/(200) crystal planes (Figure 4.2a), indicating that the as-extruded PVDF films largely transformed into the ferroelectric β-phase after drawing at 80 and 100 °C, but not entirely due to the existence of small shoulder peaks at 2θ=18.6° (α-phase). The 120 °C drawn films, however, clearly suggested the coexistence of the α- and β-phases. The observed results are consistent with reported work;[160] higher drawing temperature correlated to higher chain mobility, which could make polymer chains relax back during drawing, thus generating less effective formation of the β-phase at the same draw ratio. Figure 4b reveals the drawing rate influence on the phase transformation, which is less obvious than that of drawing temperature. All of the films drawn at 100 °C presented a strong characteristic β-phase peak at 2θ=20.8° regardless of drawing rate. But the shoulder peak at around 18.6° is more apparent for films drawn at 5 mm/min than the others, which can be explained that the phase transformation from α- to β- is a process of crystal deformation and recrystallization which needs large stress when using a higher drawing rate. More details related to the fraction of β-phase will be discussed later using FTIR spectra.

Apart from crystalline phase transformation from α- to β-phase, PVDF exhibits evolution of morphology and crystalline orientation in the process of drawing (Figure 4.3). The strain-stress curve of PVDF was terminated due to the ductile fracture (strain > 375%), and showed a typical yield point at a strain of about 8%. The whole strain stress curve is not smooth and shows typical strain hardening, both of which are ascribed to the deformation of α-phase crystallites and recrystallization of β-phase crystallites. The

initial as-extruded α-phase PVDF films displayed spherulite crystals and almost random orientation, determined from 2D-WAXD data which shows three nearly full rings at diffraction angles of 18.1°, 20.0° and 26.6°. The inner one at 18.1° corresponds to overlapped diffraction from the peaks at 17.7° (100) and 18.5° (020). The other two rings at 20.0° and 26.6° correspond to the (110) and (021) diffraction peaks, respectively. Along with the strain increase, the as-formed spherulites showed deformation but not dramatic enough to induce an obvious change in the 2D-WAXD. Further spherulite deformation generated preferred orientation identified from the equatorially concentrated diffraction of (hk0) crystal planes, which suggests the polymer chains were aligned along the drawing direction. At this stage, the diffraction rings of α-phase were still detected. The final formed drawn films displayed a finely aligned fibril structure. Moreover, the 2D-WAXD patterns show obvious diffraction ring at 20.8° (110)/(200), which is characteristic of the β-phase. The accurate content of α-phase will be calculated later using FTIR data.

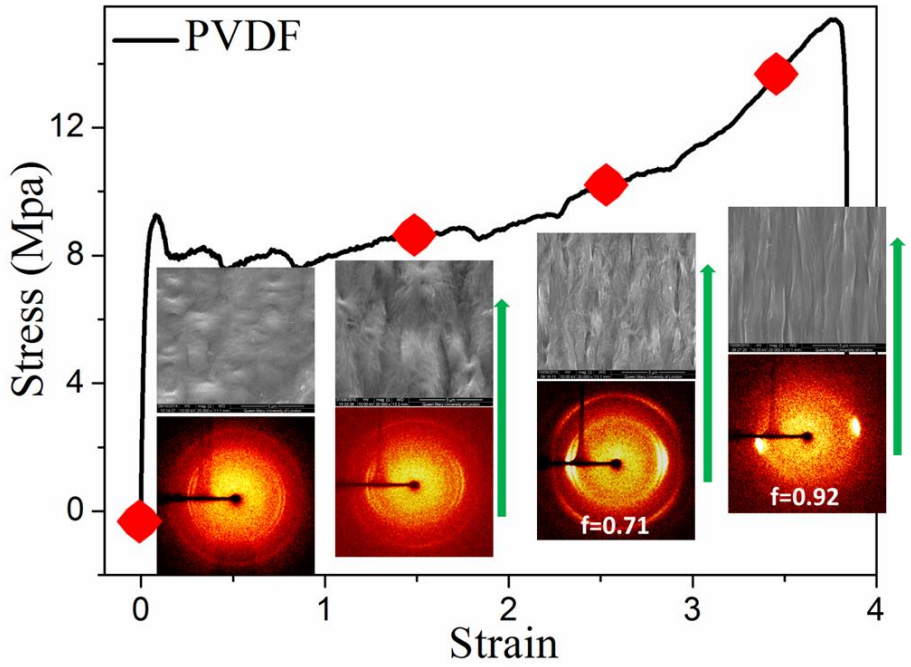

Figure 4.3 Strain-stress curves and chosen SEM morphology and 2D-WAXD ring patterns obtained during uniaxial drawing of PVDF at 100 °C and 10 mm/min. The Herman's factor values were listed in the 2D-WAXD patterns and arrows indicate the uniaxial drawing direction.

The influence of drawing condition on the crystalline preferred orientation is illustrated in Figure 4.4. To a certain extent, all of the patterns display a mixture of α- and β-phase diffraction peaks, which is consistent with 1D-WAXD data. Films drawn at 80, 100 °C and 10 mm/min exhibit the diffraction rings from the predominant β-phase crystals (Figure 4.4b), while the 120 °C drawn samples show strong diffraction from the (021) plane of α-phase crystals, and four bright arcs about 45° from the equatorial direction (Figure 4.4c), suggesting highly oriented α-phase crystals. The (021)α diffraction rings in films drawn at 100 °C 5, 25 and 50 mm/min are blurred without showing obvious arcs, indicating a high fraction of β-phase. The degree of preferred crystalline orientation was evaluated using Herman's factor *f* which is influenced by the drawing rate; a low drawing rate cannot generate enough stress to deform the α-phase spherulites,

but a too high drawing rate hinders the alignment of β-phase crystals. The deformation of α-phase and the alignment of β-phase require an appropriate drawing rate. Thus, drawing at 100 °C and 10 mm/min are optimum conditions to produce oriented ferroelectric β-phase PVDF.

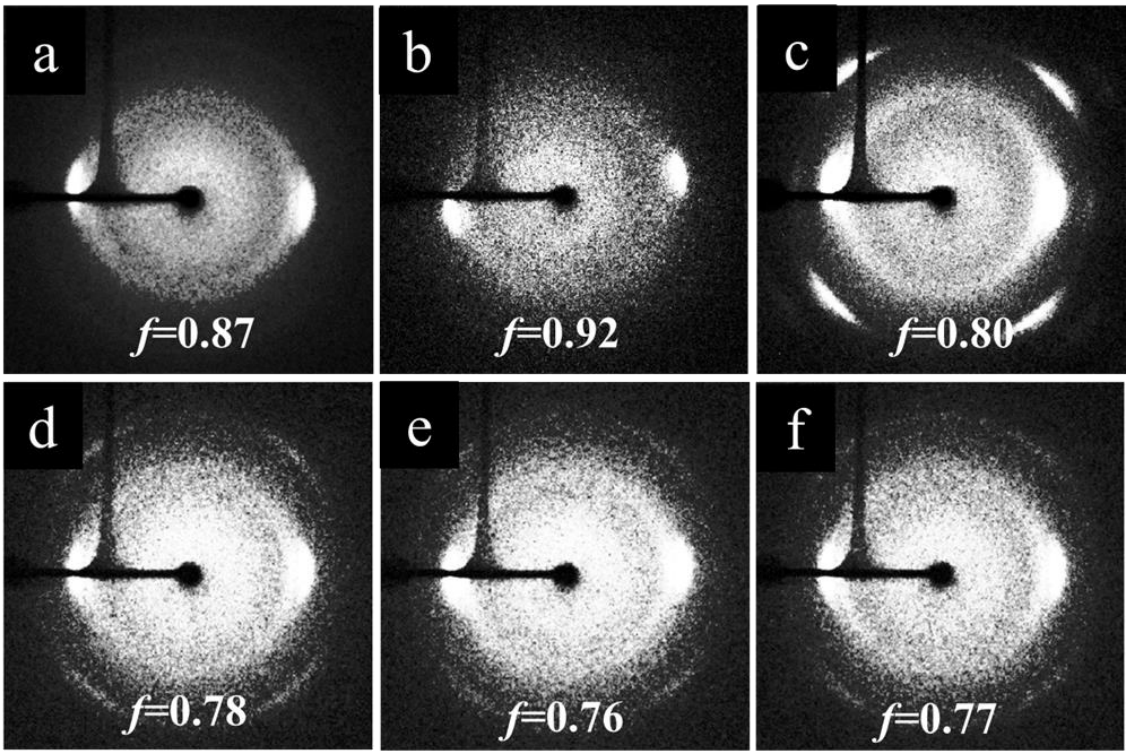

Figure 4.4 2D-WAXD patterns for drawn PVDF films with Herman's factor *f* listed at the bottom: (a) drawn at 80 °C_10 mm/min; (b) 100 °C_10 mm/min; (c) 120 °C_10 mm/min; (d) 100 °C_5 mm/min; (e) 100 °C_25 mm/min and (f) 100 °C_50 mm/min.

Molecular vibration of the as-extruded and drawn PVDF films was analysed by FTIR (Figure 4.5). The positive contribution of the rocking vibration of the CH_2 group ($r(CH_2)$) and negative contribution of the asymmetric stretching of the CF_2 group ($v_s(CF_2)$) are associated with the formation of the characteristic β-phase band at about 840 cm^{-1}. The band at 766 cm^{-1} is typical of α-phase and related to the bending vibration

of CF_2 group ($\delta(CF_2)$) and skeletal bending vibration of C(F)-C(H)-C(F) backbone (δ(CCC)).

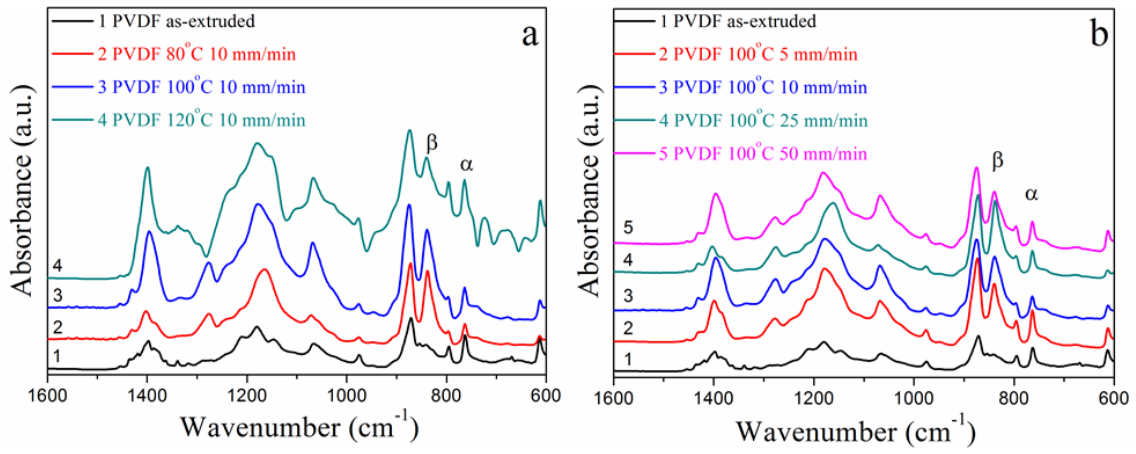

Figure 4.5 FTIR spectra for: (a) as-extruded and drawn PVDF films at 10 mm/min but different temperatures 80, 100 and 120 °C; (b) as-extruded and drawn PVDF films at 100 °C but different drawing rate 5, 10, 25 and 50 mm/min.

The fraction of β-phase ($F(\beta)$) in PVDF films was also obtained using the following equation:

$$F(\beta) = \frac{A_\beta}{\left(\frac{K_\beta}{K_\alpha}\right)A_\alpha + A_\beta} = \frac{A_\beta}{1.26 \times A_\alpha + A_\beta} \qquad 4.2$$

Equation 4.2 is built on the assumption that FTIR follows the Lambert-Beer law, where A_α and A_β correspond to the measured absorbance at 766 cm^{-1} and 840 cm^{-1}. The calculated $F(\beta)$ values are listed in Table 4.5. It is clearly seen that the drawing temperature largely affects the content of β-phase. At the same draw ratio of 10 mm/min, the $F(\beta)$ values for drawn films at 80 °C and 100 °C (~ 80%) were significantly higher than that of films drawn at 120 °C (~ 50%), which is consistent with XRD data. With regard to the drawing rate, films drawn at 5 mm/min showed a $F(\beta)$ of

only 65%, the other drawing rates made little difference to the β-phase content and all of the $F(\beta)$ values were in the range of 70-80%.

Table 4.5 Fraction of β-phase $F(\beta)$ for as-extruded (condition 3) and drawn PVDF films

Samples	$F(\beta)$
As-extruded PVDF	8±1%
Drawn PVDF 80 °C 10 mm/min	82±3%
Drawn PVDF 100 °C 10 mm/min	78±2%
Drawn PVDF 120 °C 10 mm/min	50±2%
Drawn PVDF 100 °C 5 mm/min	65±1%
Drawn PVDF 100 °C 25 mm/min	78±2%
Drawn PVDF 100 °C 50 mm/min	75±3%

4.3.3 Thermal analysis of as-extruded and drawn PVDF films

Figure 4.6 shows the DSC first heating curves for as-extruded and drawn PVDF films. The obtained values of melting temperature T_m, the enthalpy of fusion ΔH_f and crystallinity χ are listed in Table 4.6. The enthalpy of fusion of 100% crystalline PVDF used to calculate the crystallinity χ is assumed to be the same for all crystalline forms, 104.6 J/g.[161] From Figure 4.6 and Table 4.6, the melting behaviour varies between the as-extruded and drawn samples. The as-extruded PVDF films showed two obvious melting peaks and the main fusion peak was recorded a higher temperature compared to the drawn films. There are two possible explanations for this behaviour. Firstly, it is due to the existence of the smaller or imperfect crystallites in the drawn films, which have

lower melting temperature and less enthalpy of fusion. Then, the double melting peaks could be associated with a mixture of α- and β- phases. However, controversies exist regarding to the values of T_m for α- and β-PVDF. Martins *et al.* [97] suggested that α- and β-PVDF phases have indistinguishable melting temperatures in the range of 167-172 ℃, while other researchers [88, 98, 99] believed that β-PVDF should have a higher melting temperature than the α-phase due to the more densely packed all-trans chain conformation. To make things more complicated, Lanceros-Méndez group [100] reported the melting temperature of poled β-PVDF films, as 156.3 ℃, much lower than the common values for α-PVDF. Melting temperature values are governed by the crystallization of polymers, thereby different processing methods and conditions induce different melting temperatures as well as the heating rate during the DSC measurement. In this work, both the WAXD and FTIR data show the α-phase crystallization in the as-extruded PVDF films so that the lower melting temperature peak corresponds to the fusion of imperfect crystals. It is clearly seen in Table 4.6 that the drawn PVDF films show lower melting temperatures. No significant changes in the crystallinity of PVDF after drawing, all have about 50 wt. % (α- and β-phases combined), suggesting that the β-phase was transformed from the as-crystallized α-phase and nearly no recrystallization from the amorphous region.

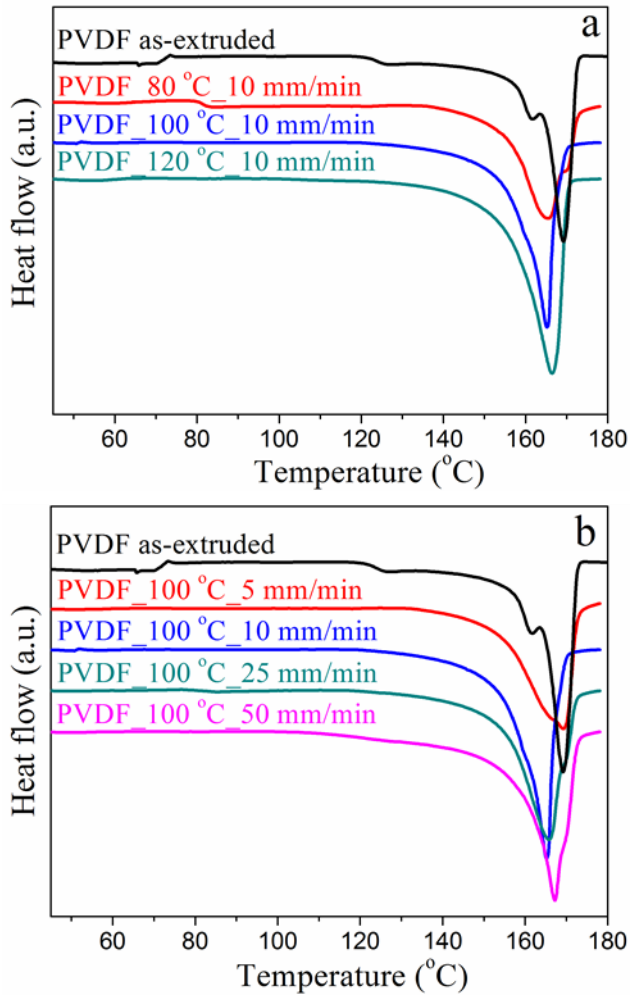

Figure 4.6 DSC first heating curves for: (a) as-extruded and drawn PVDF films at 10 mm/min but different temperatures 80, 100 and 120 °C； (b) as-extruded and drawn PVDF films at 100 °C but different drawing rates 5, 10, 25 and 50 mm/min.

Table 4.6 Thermodynamic parameters acquired from DSC data for the as-extruded and drawn PVDF films.

Samples	Melting temperature (T_m)	Enthalpy of fusion ΔH_f (J/g)	Crystallinity χ
As-extruded PVDF	161.4/169.1±1	52.9±3	51±2%
Drawn PVDF 80 °C	165.3±1	53.1±2	51±1%
Drawn PVDF	165.3±2	54.6±2	52±2%
Drawn PVDF	166.5±1	53.0±3	51±3%
Drawn PVDF	169.1±2	52.6±2	50±1%
Drawn PVDF	165.5±1	51.9±3	50±2%
Drawn PVDF	167.2±1	52.4±2	50±1%

4.3.4 Dielectric and ferroelectric properties of as-extruded and drawn PVDF films

Figure 4.7 shows the comparison of the dielectric temperature spectra for the as-extruded (extruded under condition 3) and drawn PVDF films (drawn at 100 °C and 10 mm/min). Both the as-extruded and drawn samples showed relaxation peaks (Figure 4.7b, d) at about -25 °C and 100 Hz which correlates to the glass transition of the amorphous regions and the corresponding glass transition temperatures T_g shifted to lower values with decreasing testing frequency.

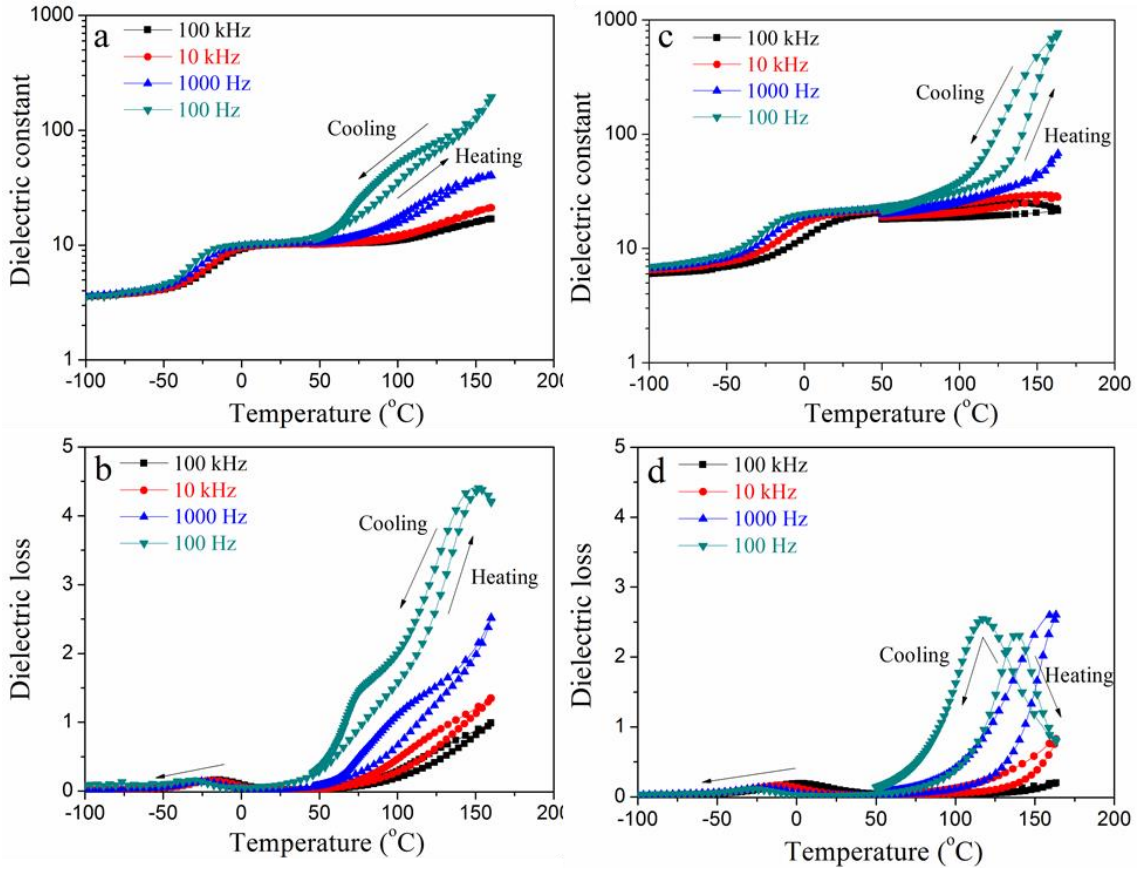

Figure 4.7 Temperature dependence of dielectric permittivity for the as-extruded and drawn PVDF films at four frequencies 100 kHz, 10 kHz, 1000 Hz and 100 Hz: (a) real part of dielectric permittivity of as-extruded PVDF films; (b) dielectric loss of as-extruded PVDF films; (c) real part of dielectric permittivity of PVDF drawn films at 100 °C and 10 mm/min and (d) dielectric loss of PVDF drawnfilms at 100 °C and 10 mm/min.

Figure 4.8 shows the dielectric temperature spectra of the as-extruded and drawn PVDF films measured at 100 Hz. The dielectric loss showed obvious peaks at about 150 °C, corresponding to the partial melting of the polymer, which appeared to occur at a higher temperature for the as-extruded samples, consistent with the DSC data, indicative that the as-extruded films have higher melting temperatures than those of the drawn films. Additionally, the dielectric loss peak due to the glass transition for the as-extruded sample seemed more intense and was at a lower temperature position. Random

molecular orientation in the as-extruded samples contributes to a sharper glass transition loss peak. And the lower T_g is ascribed to more motions of chain segments in the as-extruded films.

The dielectric constant of the drawn samples was higher as compared to the as-extruded samples, except for the temperature range of 75-130 °C, where the as-extruded samples showed a broad and step-like peak (Figure 4.8). Recall that the DSC data of the as-extruded samples showed two melting peaks corresponding to the fusion of imperfect and well-crystallized crystals, respectively. The broad dielectric constant peak at 75-130 °C is assigned to the melting peak of imperfect crystals in the as-extruded samples. And the larger dielectric constant for the drawn samples is due to the formation of polar β-phase compared to the predominant α-phase in the as-extruded samples,[138] which is also confirmed from the dielectric frequency dependence curves shown in Figure 4.9. The reported values of dielectric constant for solution casted α- and β-PVDF films are 8 and 12, respectively.[138]

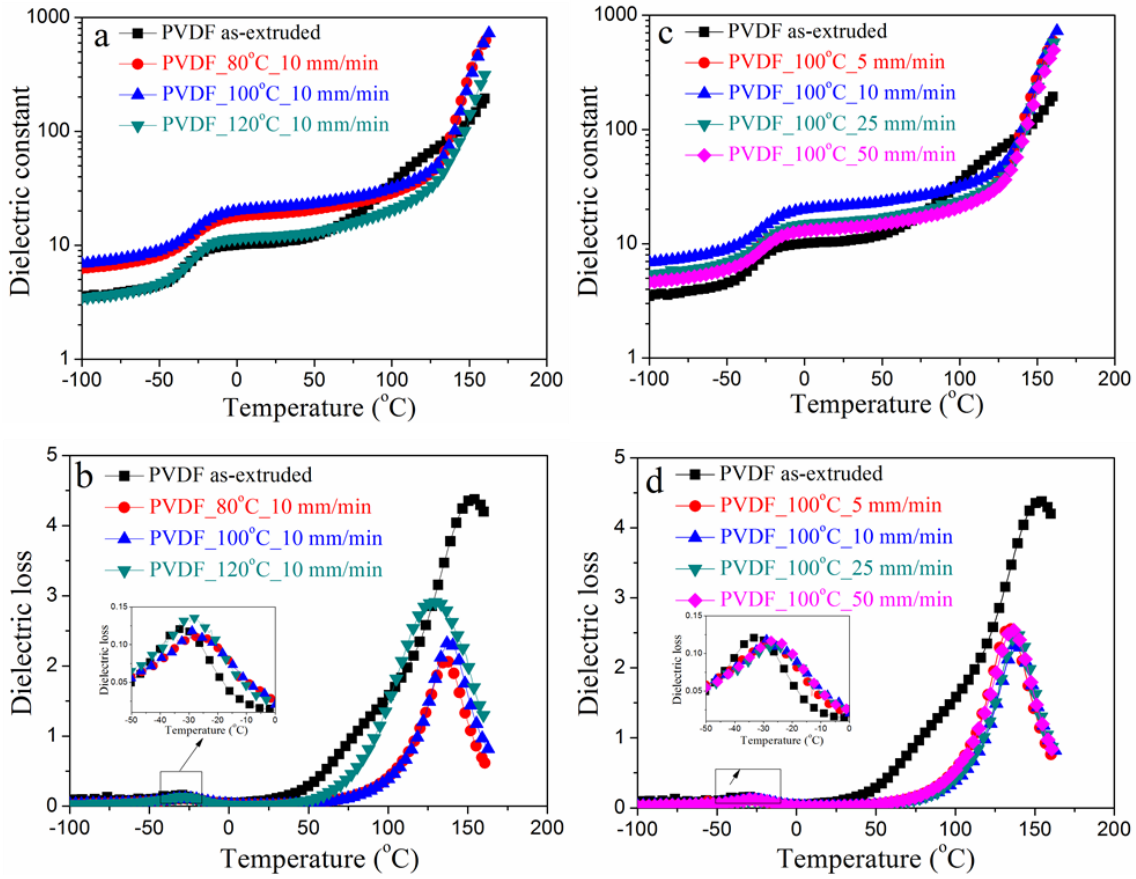

Figure 4.8 Comparison of dielectric temperature spectra for as-extruded and drawn PVDF films measured at 100 Hz: (a) real part of dielectric permittivity and (b) dielectric loss for as-extruded and drawn PVDF films at 10 mm/min but different temperatures 80, 100 and 120 °C； (c) real part of dielectric permittivity and (d) dielectric loss for as-extruded and drawn PVDF films at 100 °C but different drawing rates 5, 10, 25 and 50 mm/min.

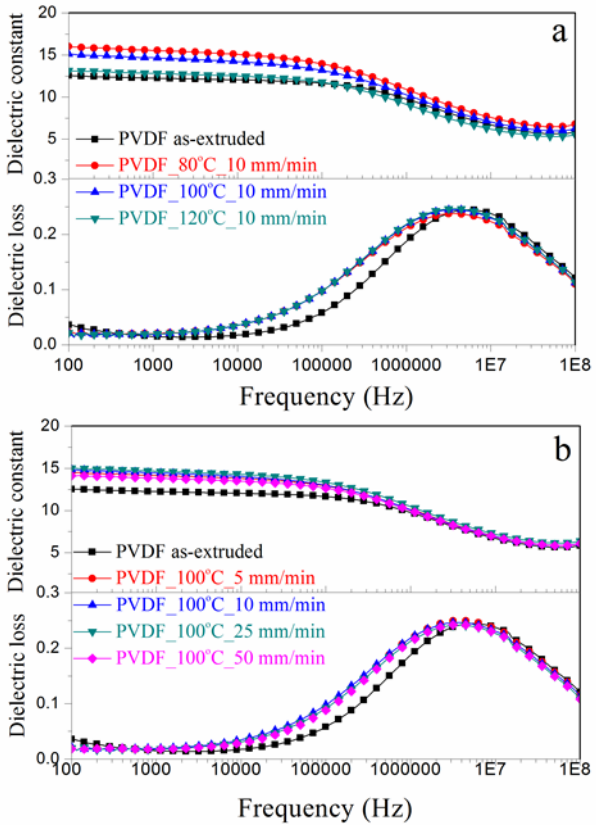

Figure 4.9 The dielectric constant and loss as a function of frequency at room temperature: (a) the as-extruded and drawn PVDF films at 10 mm/min but different temperatures 80, 100 and 120 °C; (b) the as-extruded and drawn PVDF films at 100 °C but different drawing rates 5, 10, 25 and 50 mm/min.

The ferroelectric properties for PVDF before and after drawing are shown in Figure 4.10. The as-extruded PVDF films electrically broke down at about 200 kV/mm. As analysed before, the as-extruded PVDF films crystallized predominantly into the α-phase. With increasing applied electric field, the non-polar α-phase PVDF changes into the polar δ-phase that gives rise to the ferroelectric response. The ferroelectric hysteresis loops were not saturated and the electric displacement showed current leakage. By drawing, the PVDF films could stand a maximum applied electric field of about 400 kV/mm and the acquired PE loops were saturated above 280 kV/mm. The remnant polarization for PVDF drawn at 100 °C and 10 mm/min is about 0.096 C/m^2. The

spontaneous polarization of β-PVDF is reported to be 0.13 C/m^2 based on the rigid dipole model.[15] From DSC data, the crystallinity of the PVDF films drawn at 100 °C and 10 mm/min was about 50%, consequently, the estimated value of remnant polarization is about 0.065 C/m^2, which is much lower than the obtained experimental value. The reasons for this could be, firstly, the enthalpy of fusion for a fully crystalline β-phase PVDF is lower than the 104.6 J/g used to calculate the crystallinity based on DSC data; however, the accurate value is not available in the literature; secondly, apart from the crystalline dipoles, dipoles in the amorphous region and/ or the interfaces between the crystalline and amorphous parts could also be polarized and contribute to the remnant polarization.

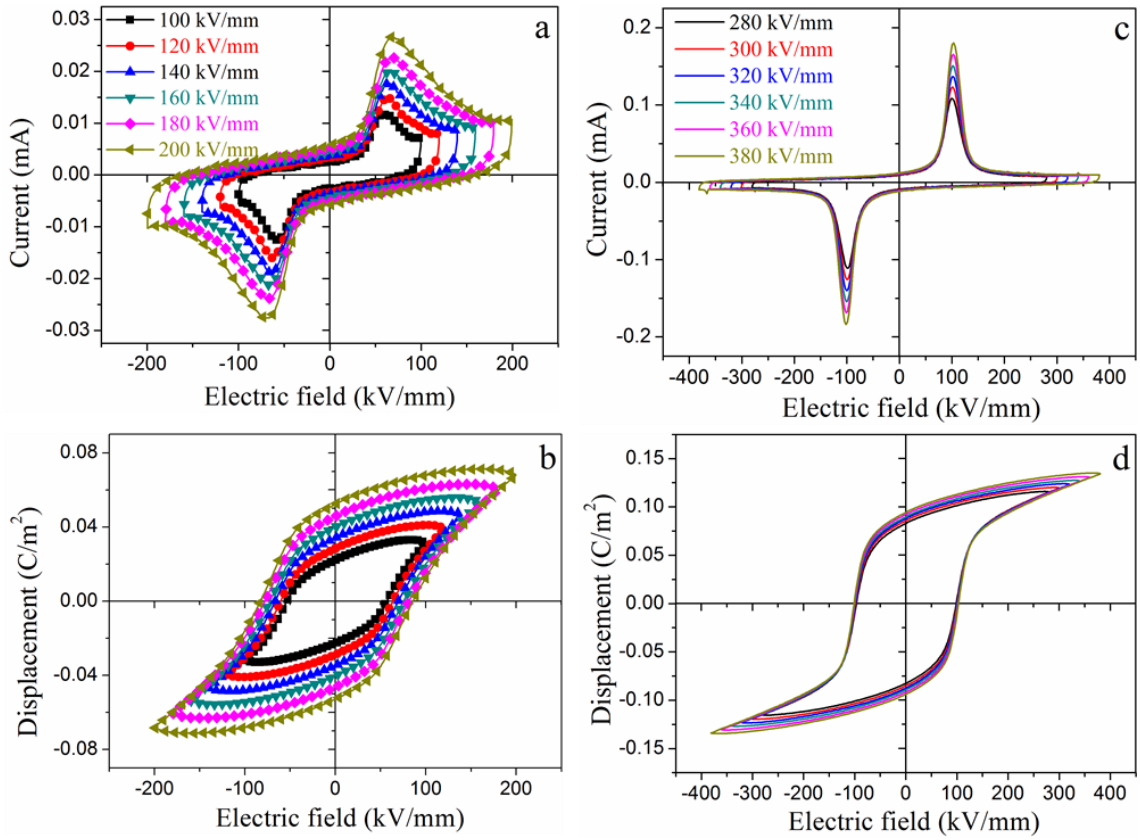

Figure 4.10 Ferroelectric hysteresis loops for: (a, b) as-extruded PVDF; (c, d) drawn PVDF at 100 °C and 10 mm/min, measured at room temperature and 10 Hz.

A comparison of ferroelectric properties of the drawn PVDF films is shown in Figure 4.11. All of the drawn films showed well-defined ferroelectric hysteresis loops, with a coercive field of about 100 kV/mm and remnant polarization of about 0.10 C/m^2, and no obvious difference can be observed.

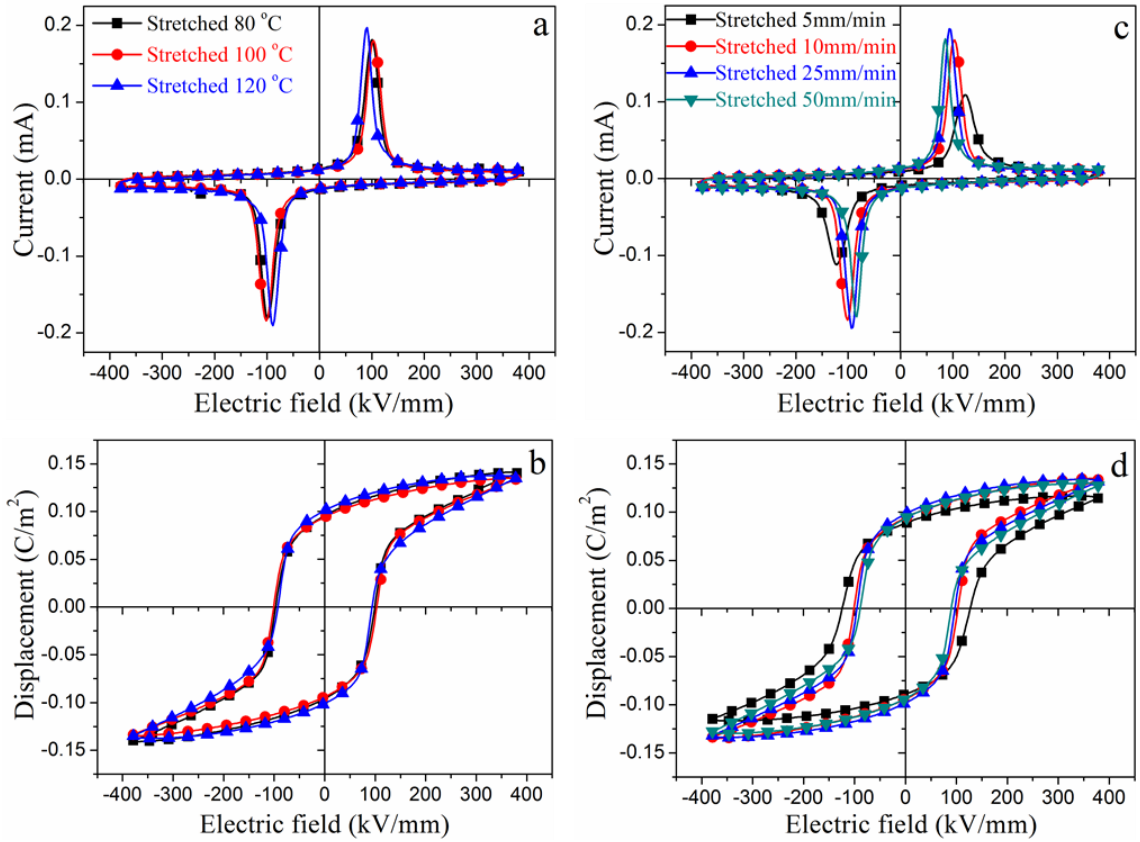

Figure 4.11 Comparison of ferroelectric hysteresis loops for drawn PVDF at 380 kV/mm: (a, b) films drawn at 10 mm/min but different temperatures 80, 100 and 120 °C; (c, d) films drawn at 100 °C but different drawing rates 5, 10, 25 and 50 mm/min. The ferroelectric hysteresis loops were measured at room temperature and 10 Hz.

4.4 Conclusions

The processing, characterization and functional properties of PVDF are presented in this chapter. The melt extruded PVDF films mainly crystallized into non-ferroelectric α-phase regardless of the processing conditions. The ferroelectric β-phase PVDF was obtained by high temperature drawing of the α-phase of as-extruded films. Both the α- and β-phase existed in the drawn films.

The fraction of β-phase was influenced by the draw ratio, drawing temperature and drawing rate. The formation of β-phase requires a minimum draw ratio of 3. Upon increasing the drawing temperature to above 100 °C, the induced high chain mobility could only orientate the α-crystals along the drawing direction, but did not make the chain conformation change to form the β-phase. At the same draw ratio and drawing rate (draw ratio 3, drawing rate 10 mm/min), films drawn at 120 °C contained only 50% β-phase, lower than that of films drawn at 80 °C and 100 °C (~ 80%). Films drawn at 100 °C and 5 mm/min contained only 65% β-phase, which increased to 80% with increasing drawing rate to 10 mm/min, but any further increase in the drawing rate made no difference on the content of β-phase.

Regarding crystalline features, drawing changed the spherulites to a fibril structure and caused the polymer chains to orientate along the drawing direction, resulting in preferred crystalline orientation. The overall crystallinity calculated using the values of the enthalpy of fusion did not alter after drawing. However, the melting temperatures of the drawn films were lower than that of as-extruded films, as determined from both the DSC data and dielectric temperature spectra. Moreover, the dielectric temperature

spectra also indicated higher glass transition temperatures for the drawn films. The dielectric constant values of the drawn films were higher compared to the as-extruded films because of their higher β-phase content.

The drawn films showed significantly higher ferroelectric remnant polarization and less current leakage as compared to the as-extruded films. It is believed that the improvement in the ferroelectric properties is mainly ascribed to their higher β-phase content and preferred orientation.

Chapter 5 Processing and Characterization of Free Standing Highly Oriented Ferroelectric Polymer Films with Remarkably Low Coercive Field and High Remnant Polarization

5.1 Introduction

It was confirmed in Chapter 4 that PVDF exhibits an obvious disadvantage for ferroelectric applications in that it cannot simply crystallize into the ferroelectric β-phase. This problem was perfectly solved through introducing another comonomer during the synthesis of PVDF, for example, trifluoroethylene (TrFE) or tetrafluoroethylene (TFE), serving as defects, which makes the all-trans chain conformation become more stable than the trans-gauche conformation. Accordingly, the copolymers, PVDF-TrFE and PVDF-TFE can easily crystallize into ferroelectric β phase, even when simply cooled from the melt state.[15] In this chapter, the processing of highly aligned and highly crystalline PVDF-TrFE films is described as well as their structure characterization and functional properties.

The processing method can significantly influence the crystalline orientation, degree of crystallinity, as well as the crystalline phases formed. Melt extrusion is a common method used to produce oriented flexible chain polymers. Many studies[162-168] related to melt extrusion have been conducted on polyethylene (PE) which has the same all-trans chain conformation as that of PVDF-TrFE (50-80 mol. % VDF), giving rise to a similar

crystallographic structure; orthorhombic unit cell in which the values of a-, b-, and c- are 7.4 Å, 4.94 Å and 2.54 Å (PE)[166] and 9.05 Å, 5.12 Å and 2.55 Å (PVDF-TrFE 70/30 mol. % [26]). Well-stacked untwisted lamellae crystallites are formed in the extruded PE films as well as a preferred orientation of the c-axis along the extrusion direction.[164] With regard to PVDF-TrFE extruded films, Furukawa[21] reported that PVDF-TrFE 78/22 mol. % extruded films exhibited a sharp switching current peak due to the well-aligned lamellae, but the characterization of crystalline orientation and E_c value were not reported, and the P_r of as-extruded films was only 0.03 C/m^2. Lovinger *et al.* [169] reported extruded PVDF-TrFE 52/48 mol. % films poled at 70 kV/mm at room temperature showed preferred orientation, which they assumed was produced by the poling and not the extrusion.

In this chapter, it is shown that preferred orientation does exist in extruded PVDF-TrFE (51/49 mol. %) films even without poling (Figure 5.1). Then the melt extrusion processing temperature (190 °C) was optimized to produce highly crystallised and orientated films. The E_c of highly oriented films was 24 kV/mm, which is half of the commonly reported value for bulk films (50 kV/mm). The P_r of the annealed optimized extruded films was 0.099 C/m^2, which is close to the theoretical limit of 0.102 C/m^2.

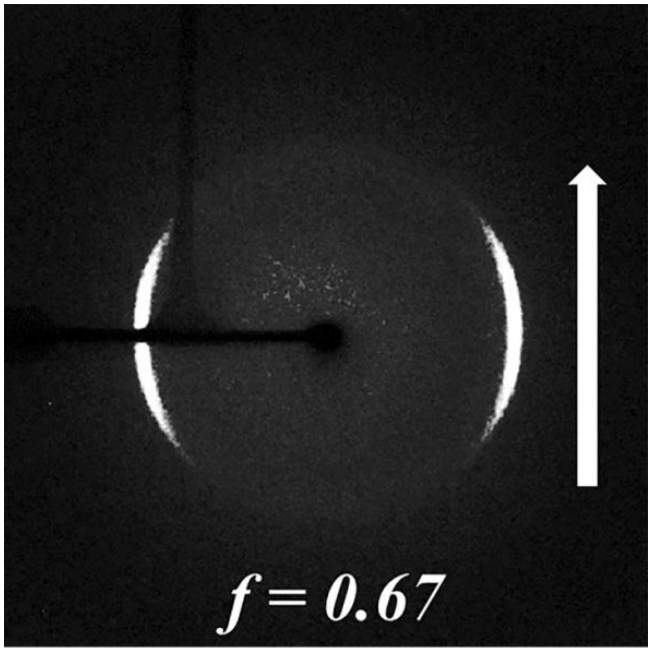

Figure 5.1 2D-WAXD ring pattern of extruded PVDF-TrFE 51/49 mol. % films, the displayed arcs suggests the preferred orientation in the extruded films.

5.2 Experimental details

PVDF-TrFE pellets, with the molecular composition of 77/23 mol% were purchased from Piezotech S.A.S, (France). The molecular weights reported by other researchers are M_w and M_n 210 and 100 kg/mol, respectively.[142] The PVDF-TrFE films were extruded at 170℃, 175 ℃, 190 ℃, 205 ℃ or 210 ℃. The screw speed was 75 rpm. A 200 μm slit die was connected to the extruder. The take up speed was 180 mm/min at ambient conditions. Films extruded at 190 ℃ were clamped and annealed at 140 ℃ for 24 hours. The thickness of extruded films was about 10-35 μm. For dielectric and ferroelectric measurements, gold electrodes (~ 100 nm thick) were evaporated on both sides of the films, and the diameters of electrodes for dielectric and ferroelectric testing were 5 mm and 2 mm, respectively.

5.3 Results and discussion

5.3.1 Crystalline preferred orientation

Figure 5.2 shows 2D-WAXD ring patterns of the PVDF-TrFE films extruded at different temperatures. In Figure 5.2a-e, all of the samples exhibit equatorial 110 and 200 reflections, suggesting that their c-axes were preferentially oriented along the extrusion direction. The corresponding diffraction angle is $2\theta = 20.12°$. The 190 ℃ extruded films had the narrowest arcs. The preferred orientation of the films was quantified using Herman's orientation factor (*f*) using a Gaussian fit. Calculated values of *f* are listed at the bottom of Figure 5.2. For the films extruded at 170 ℃, *f* is 0.65, indicating moderate crystalline preferred orientation. It increased to 0.72 for the 175 ℃ extruded films. After peaking at 0.89 for the 190 ℃ extruded films, *f* slightly decreased to 0.81 for the 205 ℃ extruded films and further declined to 0.57 for the 210 ℃ extruded films. The change of the *f* values indicates the degree of orientation of the polymer chains is strongly related to the extrusion temperature and more details will be discussed later in the section 5.3.2 on morphology determination. Figure 5.2f shows the diffraction pattern with X-ray beam along the extrusion direction (i.e., through the thickness of the film). The complete ring in Figure 5.2f indicates the random orientation of the b-axis about the c-axis in the extruded PVDF-TrFE films.

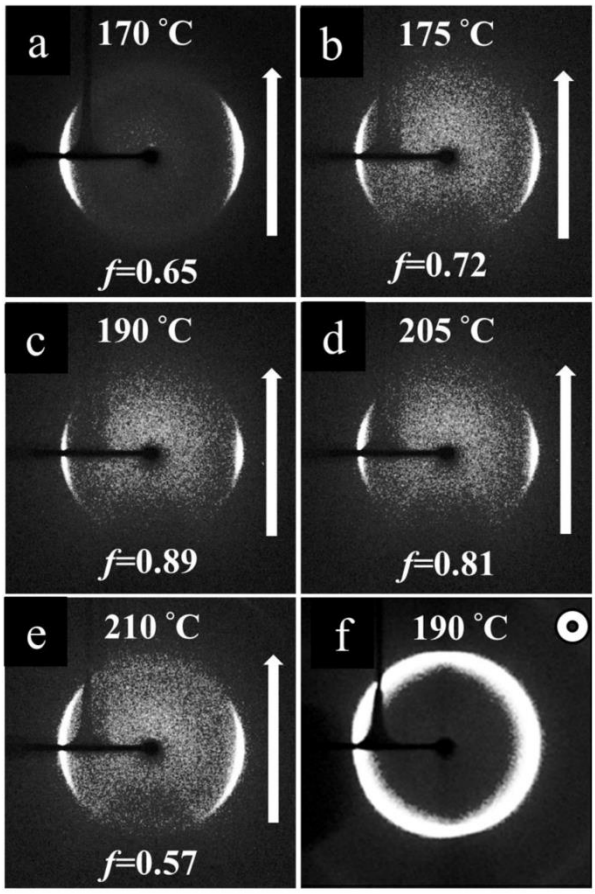

Figure 5.2 2D-WAXD ring patterns for PVDF-TrFE films extruded at: (a) 170 ℃; (b) 175 ℃; (c) 190 ℃; (d) 205 ℃ and (e) 210 ℃. Arrows indicate the extrusion direction, and the X-ray beam was parallel with the normal to the film surface. Values of Herman's orientation factor (f) are listed at the bottom. (f) 2D-WAXD ring pattern for the cross-section of PVDF-TrFE films extruded at 190 ℃, and X-ray beam was parallel to the extrusion direction.

5.3.2 Morphology determination

Film surface, side and cross-section SEM images were used to determine the structure of the crystallites in the 190 ℃ extruded films (Figure 5.3a-c). Surface morphology displayed well-ordered lamellae oriented perpendicular to the extrusion direction (Figure 5.3a), which is consistent with the XRD data showing the narrowest equatorial 110 and 200 reflections (Figure 5.2c). The side region morphology (Figure 5.3b) of the

extruded films is similar to that displayed by the film surface, while the cross-section region (Figure 5.3c) along the extrusion direction exhibits a flat morphology, which is consistent with the random orientation of the crystallites concluded from the XRD data (Figure 5.2f). Lamellae crystallites are formed by folded chains and grow in the direction along the largest temperature gradient, which is the extrusion direction during processing. According to the XRD data (Figure 5.2a-e), the polymer chain axes are also along the extrusion direction. Combining this with the SEM images, the extruded PVDF-TrFE films crystallize into edge-on lamellae crystallites (as illustrated in Figure 5.3d). The cubic shape shown in Figure 2d is only for graphic simplification. As shown in Figure 5.3c the face side of the lamellae have polyhedral shape. The thickness of the lamellae crystallites are about 10 nm, which is consistent with the value that calculated using the Scherrer equation and the XRD data (12 nm).

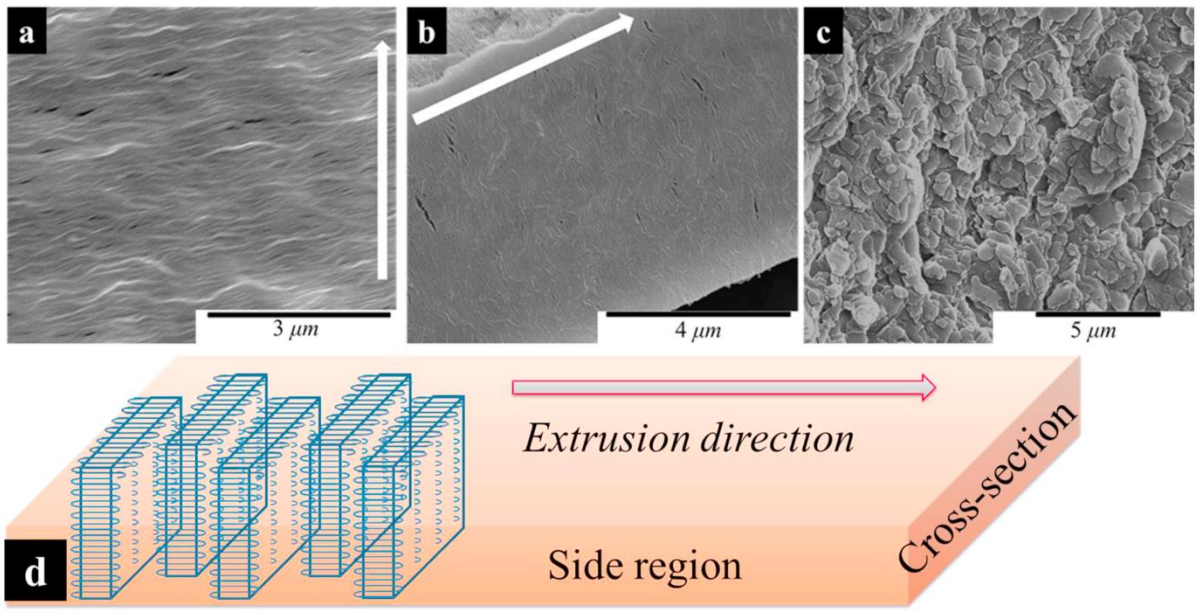

Figure 5.3 Structure determinations for 190 ℃ extruded films: (a) film surface SEM image; (b) side region along the extrusion direction SEM image; (c) cross-section perpendicular to the extrusion direction SEM image; and (d) corresponding schematic diagram of edge-on lamellae.

Figure 5.4 shows the comparison of surface morphology for PVDF-TrFE films extruded at different temperatures. When PVDF-TrFE was extruded at 170 ℃, due to its relatively high viscosity, the polymer chains were difficult to mobilize under the extension flow. As a result, the PVDF-TrFE crystallized into slightly aligned long needle-like lamellae (Figure 5.4a). The surface morphology changed to a twisted lamellae morphology when the extrusion temperature was increased to 175 ℃ (Figure 5.4b). A high proportion of the lamellae oriented perpendicular to the extrusion direction, suggesting planar extension flow along the extrusion direction and uniaxial preferred orientation. As discussed before, the 190 ℃ extruded films exhibited well-ordered lamellae oriented perpendicular to the extrusion direction (Figure 5.4c). The films extruded at 205 ℃ and 210 ℃ (Figure 5.4d and 5.4e) displayed more twisted or tilted lamellae morphology compared to the film extruded at 190 ℃ (Figure 5.4c), especially the films extruded at 210 ℃.

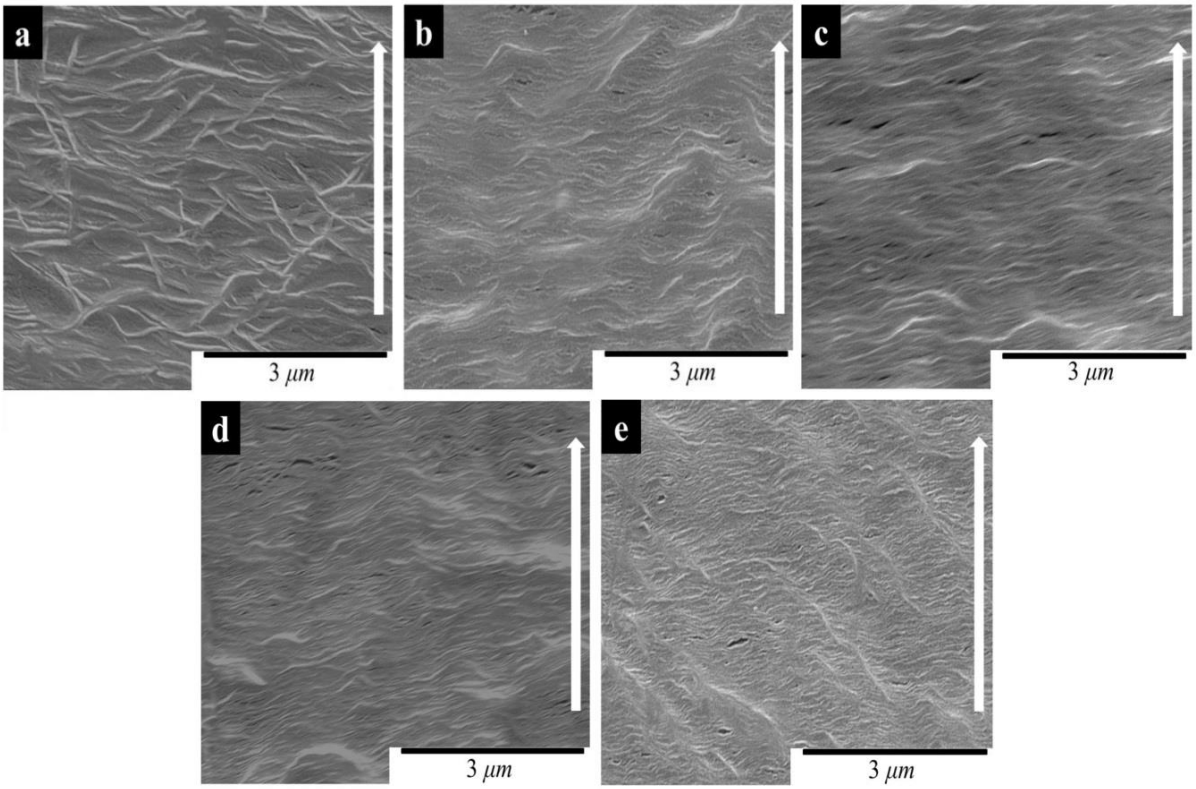

Figure 5.4 Surface SEM images of PVDF-TrFE extruded at different temperatures: (a) 170 ℃; (b) 175 ℃; (c) 190 ℃; (d) 205 ℃; (e) 210 ℃. Arrows indicate the extrusion direction.

At the lower extrusion temperatures (below 175 °C) the higher viscosity of the films produced longer chain relaxation times at the die exit. When the extrusion temperature was above 175 ℃, the chain mobility was high enough for extension flow. However, with further increasing temperature, shorter chain relaxation times prejudiced preferred orientation. The 170 ℃ and 210 ℃ extruded films will not be discussed further in this chapter because of the much less preferred orientation compared to the other three films.

5.3.3 Thermal analysis

Figure 5.5 shows the DSC first heating scans for the PVDF-TrFE films extruded at different temperatures. The characteristic temperature values and thermodynamic parameters obtained from DSC are listed in Table 5.1. A sample crystallized during a DSC cooling process that had not experienced extension flow was chosen as a reference. The extruded films show a higher Curie point T_c and lower melting temperature T_m compared to the reference sample. Large amounts of gauche bonds possessing higher potential energy are formed during the Curie transition. The higher T_c indicates well-ordered all-trans chains in the extruded films. The T_c increased from 132.8 to 134.0 ℃ when the extrusion temperature increased from 175 to 190 ℃. A further increase of the extrusion temperature to 205 ℃ did not make a significant difference (only 0.2 ℃ higher). Considering the morphological features of the films (Figure 5.4), the 190 ℃ extruded films displayed more planar lamellae texture, indicating higher preferred orientation compared to the film extruded at 175 ℃, which resulted in a higher T_c. The level of preferred orientation did not significantly alter the T_m values, and they were all at about 147.5 ℃ for the PVDF-TrFE extruded films. The higher T_m of the reference sample is ascribed to the slower cooling rate during the DSC experiments compared to the extrusion processing allowing more time to array polymer chains forming larger crystallites. Both the extrusion and reference samples showed similar values of the enthalpy of fusion ΔH_f, which indicates that the degree of crystallinity of all of the films was similar. Koga *et al.* [170] reported the ΔH_f of PVDF-TrFE 74/26 mol. % films annealed at 140 ℃ for 1 hour as 33.47 J/g. They concluded that annealed films had a high degree of crystallinity of above 90%. Using their data, the crystallinity of the PVDF-TrFE extruded films in this work is estimated to be about 80%. The values of the

enthalpy of Curie transition ΔH_c for the extruded films were larger than that of the reference sample, and their Curie transition peaks were sharper; both of which suggest that the lamellae of extruded films are formed by more regular all-trans chains. If polymer chains were less regular, a larger amount of gauche bonds and/or chain kink would exist, thereby making the Curie transition peak broader and shift to lower temperature due to the unavoidable accompany of chain rotation and chain twist during the conformation change from all-trans to trans-gauche.[170]

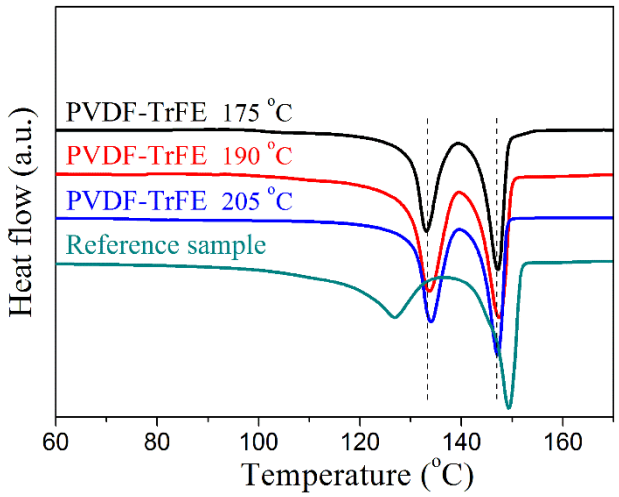

Figure 5.5 DSC first heating scans of the PVDF-TrFE extruded films. A DSC second heating scan was chosen as a reference to highlight the orientation effect on thermal parameters.

Table 5.1 Characteristic temperature and thermodynamic parameters from DSC for films extruded at different temperatures and second heating reference samples.

	$*T_c$ (℃)	$*T_m$ (℃)	$*\Delta H_c$ (J/g)	$*\Delta H_f$ (J/g)
Reference	127.1±1	149.2±1	20.66±2	30.11±2
Extruded @175 ℃	132.8±1	147.4±1	25.28±2	29.19±1
Extruded @190 ℃	134.0±1	147.7±1	28.93±1	28.98±2
Extruded @205 ℃	134.2±1	147.4±1	29.25±1	28.91±2

$*T_c$: Curie point; T_m: melting temperature; ΔH_c: enthalpy of Curie transition; ΔH_f: enthalpy of fusion.

5.3.4 Ferroelectric properties

Figure 5.6 shows the ferroelectric properties of the PVDF-TrFE extruded films with a maximum field of 150 kV/mm; the E_c and P_r values are listed with the Current-Electric field (IE) curves (Figure 5.6a) and Polarization displacement-Electric field (PE) loops (Figure 5.6b), respectively. The Herman's orientation factor f values are also listed in Figure 5.6a to emphasize the relationship between preferred orientation and ferroelectric properties. The PE loops are saturated, which was confirmed by the invariance of the current peak position above a certain maximum applied electric field (~ 120 kV/mm). The PE loops for the extruded films were nearly square, except for the 175 ℃ extruded films. The larger value of P_r for these films is an artefact arising from current leakage at such a high electric field (150 kV/mm), which is confirmed by the inset in Figure 5.6a. Comparing the ferroelectric data for the 190 and 205 ℃ extruded films, the former ones

exhibited lower E_c (and slightly lower P_r), which can be explained by the fact that the 190 ℃ extruded films exhibited easier ferroelectric switching because of the high preferred orientation of their lamella structure. The preferred orientation also influences the dielectric properties of the extruded films (Figure 5.7). The 190 ℃ extruded films, which had the highest preferred orientation, exhibited the lowest dielectric constant.

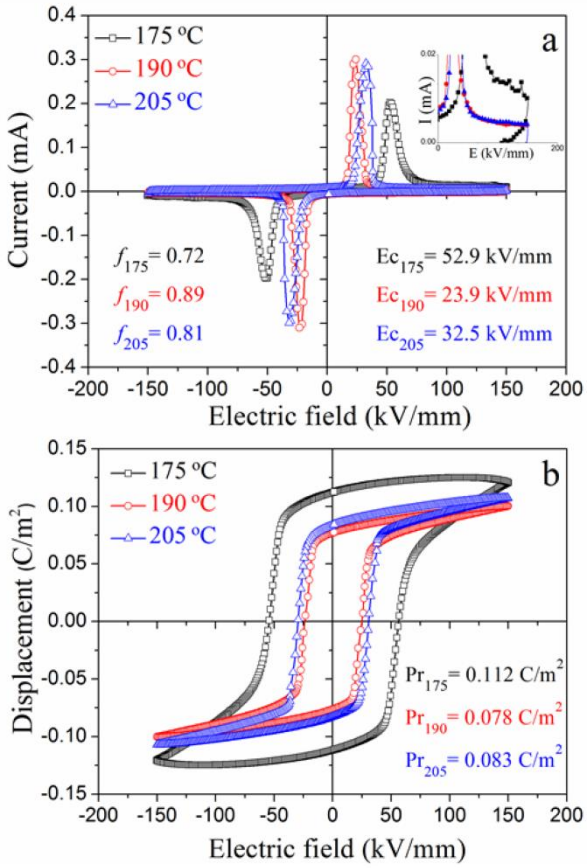

Figure 5.6 Ferroelectric reversal of PVDF-TrFE extruded films: (a) IE curves; (b) PE loops; the inset in (a) corresponds to IE curves at I < 0.02 mA, 0<E≤150 kV/mm.

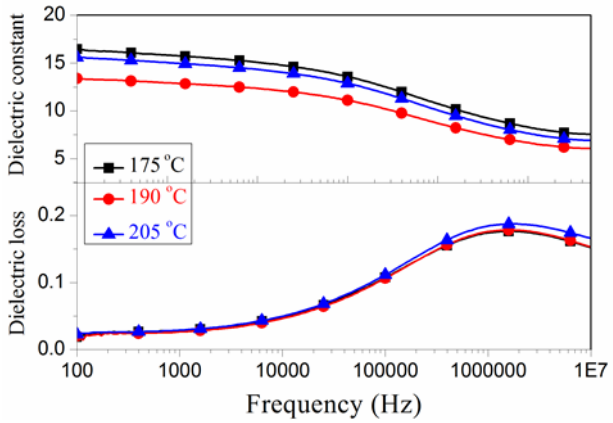

Figure 5.7 The frequency dependence of dielectric permittivity for films extruded at different temperatures.

From the IE curves, it can be observed that the extruded films exhibited well defined switching current peaks. The position of switching peak for the 190 ℃ extruded PVDF-TrFE films occurs at a lower electric field and a slightly higher maximum current compared to the other extruded films, suggesting easier ferroelectric switching. The value of E_c for the PVDF-TrFE 190 ℃ extruded films was 24 kV/mm, half of the value commonly reported for bulk materials (~ 50 kV/mm[28, 43]). Note that the E_c of the less oriented 175 ℃ extruded films, 52.3 kV/mm, is similar to that typically reported for PVDF-TrFE (films prepared by either hot compression or solution casting).

The theoretical value of the spontaneous polarization P_s of β-PVDF based on a rigid dipole model using the dipole moment and unit cell volume is $P_s = 2\mu_v/abc = 0.13$ C/m^2.[15] The P_s of PVDF-TrFE decreases with increasing molecular ratio of TrFE, which is due to a decrease of the dipole moment and the expansion of the unit cell volume.[28] Using the neutron data for PVDF-TrFE reported by Legrand *et al.*,[26] the average dipole moment of PVDF-TrFE 77/23 mol. % monomer is estimated to be $\mu = \mu_v \times (1\text{-}x/2) = 6.2\times10^{-30}$ Cm (where x is equal to the content of TrFE, 0.23); unit cell parameters are

a=8.95 Å, b=5.07 Å and c=2.55 Å. Assuming a rigid dipole model, the theoretical value of P_s for PVDF-TrFE 77/23 mol. % is 0.107 C/m^2 which is consistent with the reported results for PVDF-TrFE 75/25 mol. % and PVDF-TrFE 72/28 mol. %.[45 171] Assuming perfect in-plane c-axis orientation and random b-axis orientation, the maximum possible P_r is 0.102 C/m^2 for a fully crystalline material.[15] The maximum possible P_r value for the extruded films is 0.082 C/m^2 taking crystallinity into calculation (crystallinity 80%). The P_r of the 190 ℃ extruded films (0.078 C/m^2) is close to this estimated value (0.082 C/m^2).

The 190 ℃ extruded films were annealed to increase their crystallinity. It was found that the optimum annealing temperature was between the Curie and melting points at 140 ℃ for 24 hours, which is due to the high chain mobility allowing the rearrangement of polymer chains and occurrence of lamellae thickening (Figure 5.8b bottom right inset SEM). This increased the crystallinity of the PVDF-TrFE films to ~ 90% (Figure 5.8a), which improved their ferroelectric properties and P_r value increased to 0.099 C/m^2 with an E_c of 37.9 kV/mm (Figure 5.8b). The P_r value is close the estimated maximum possible P_r value (0.102 C/m^2) for 100% crystallization and perfect in-plane c-axis orientation (Figure 5.9). Due to a reduction of the preferred orientation, f decreased from 0.89 to 0.78 during annealing (Figure 5.8b), the extruded films annealed at 190 ℃ show a higher E_c (~ 38 kV/mm) compared to the as-extruded films, but still much lower than the commonly reported values for fully saturated PE loops of ~ 50 kV/mm. These results compare favourably with the results reported in the literature for free standing copolymer films. For melt compression processed films without poling, the reported P_r values range from 0.058 to 0.065 C/m^2 and E_c from 40 to 50 kV/mm (see Table 5.2).[28, 42] Poling significantly increased P_r to 0.09 C/m^2 for melt compression films.[172] The best

previously reported results for a free standing copolymer film are P_r of 0.11 C/m^2 and E_c of 55 kV/mm for a uniaxially stretched (draw ratio 5) PVDF-TrFE 68/32 mol. % film followed by a two-step annealing process 120 ℃ for 2 hours and 134 ℃ for 2 hours.[43] However, it should be noted that the P_r of 0.11 C/m^2 is higher than the rigid model estimated P_s value (0.099 C/m^2), which suggests there might be some contribution from leakage current.

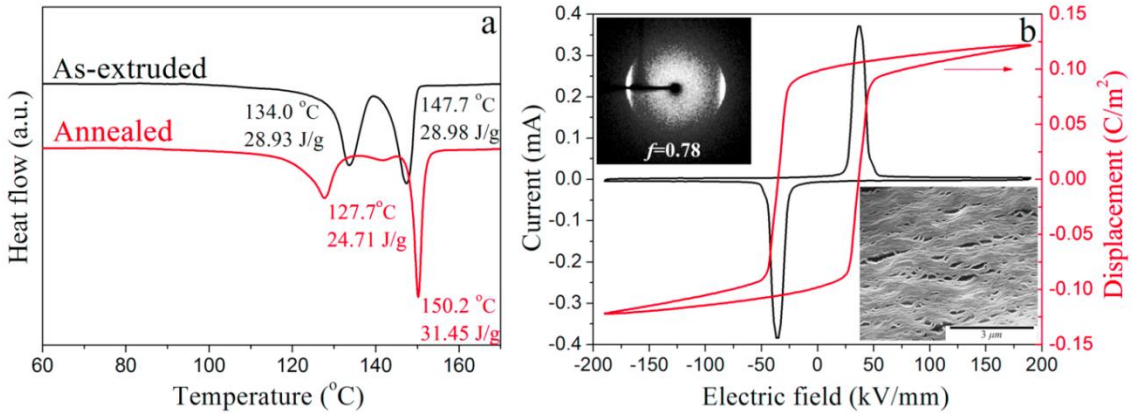

Figure 5.8 DSC comparison between as-extruded and annealed samples; (b) 2D-WAXD crystalline orientation (top left inset), SEM morphology (bottom right inset) and ferroelectric properties for annealed 190 ℃ extruded films.

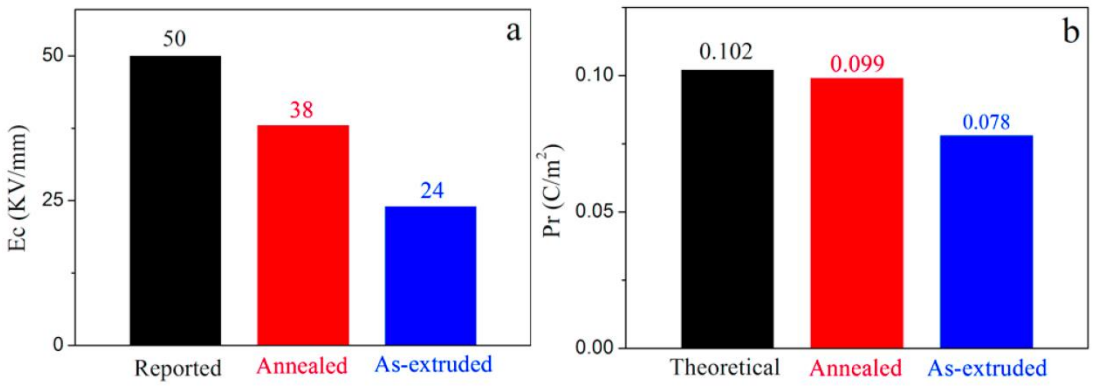

Figure 5.9 Comparison of ferroelectric properties: (a) E_c values of average reported and PVDF-TrFE 190 ℃ films; (b) P_r values of theoretical limit and PVDF-TrFE 190 ℃ films.

Table 5.2 Ferroelectric properties of PVDF-TrFE reported in the literature.

Reference	Processing methods	Orientation & thickness	Molecular ratio	E_c (kV/mm)	P_r (C/m^2)	PE loops measurement
This work	Extruded at 190 ℃	Oriented ~ 15 μm	77/23	24	0.078	150 kV/mm
	Extruded at 190 ℃; annealed 140 ℃_24 hours	Oriented ~ 15 μm	77/23	38	0.099	190 kV/mm 10 Hz
Furukawa *et al.* [173]	Solution cast	Random Not mentioned	55/45	35	0.040	80 kV/mm 300 Hz
Ohigashi *et al.* [44]	Solution cast, uniaxially stretched (five times), annealed 138 ℃_2 hours, and poled	Oriented 10-100 μm	75/25	38	0.10	Not presented
Huang *et al.* [43]	Solution cast, uniaxially stretched (five times), and annealed 120 ℃_2 hours and 134 ℃_2 hours	Oriented ~ 20 μm	68/32	55	0.11	150 kV/mm 10 Hz
Davis *et al.* [28]	Melt compression	Random ~ 40 μm	65/25	50	0.058	80 kV/mm 60 Hz
Davis *et al.* [28]	Melt compression	Random ~ 40 μm	73/27	40	0.065	100 kV/mm 60 Hz
Christie *et al.* [172]	Melt compression; poled at 150 kV/mm	Random ~ 30 μm	73/27	50	0.090	150 kV/mm 104 Hz

It is well known that the macroscopic nucleation-growth model, which involves domain nucleation and subsequent forward and sideways growth of domains, fits the ferroelectric switching behaviour of most ferroelectrics.[21, 174] With regard to PVDF-TrFE, the ferroelectric switching is produced by the rotation of polymer chains[9, 174], which is predominantly influenced by the chain packing and the interrelated lamellae crystallites. Figure 5.10 shows the FTIR spectra for PVDF-TrFE films with different degrees of preferred orientation. The corresponding wavenumber values are listed in Table 5.3. The characteristic band at about 1170 cm^{-1} is mainly assigned to the asymmetric stretching of the CF_2 group ($v_a(CF_2)$).[175] The positive contribution of the wagging vibration of CH_2 group ($\omega(CH_2)$) and the negative contribution of asymmetric stretching of CC group ($v_a(CC)$) are associated with the formation of the characteristic band at about 1400 cm^{-1}.[175] The 190 ℃ extruded films exhibited a highest wavenumber (1176 cm^{-1}) of $v_a(CF_2)$ band and a lowest wavenumber (1392 cm^{-1}) of $\omega(CH_2)$-$v_a(CC)$ band (Table 5.3). On the basis of Hooke's law, the vibration frequency is determined by the force constant and the atom mass. Therefore the highest frequency of $v_a(CF_2)$ and lowest frequency of $\omega(CH_2)$-$v_a(CC)$ bands indicate the largest force constant, which suggests that the strongest bonds exist between C-F and C-C. Polymer chains align nearly perfectly along the extrusion direction in the 190 ℃ extruded films. The parallel chain packing enables the F atoms in one molecular chain be attracted to the H atoms in its neighbouring chain, thereby generating the intermolecular dipole-dipole interaction. Such intermolecular interaction gives rise to a close chain packing. This is in line with the perfect alignment of lamellae crystallites in the 190 ℃ extruded films. More ordered chain packing significantly decreases the pinning sites[174, 176] for domain walls in PVDF-

TrFE, which promotes the ferroelectric polarization reversal and further reduces the coercive field.

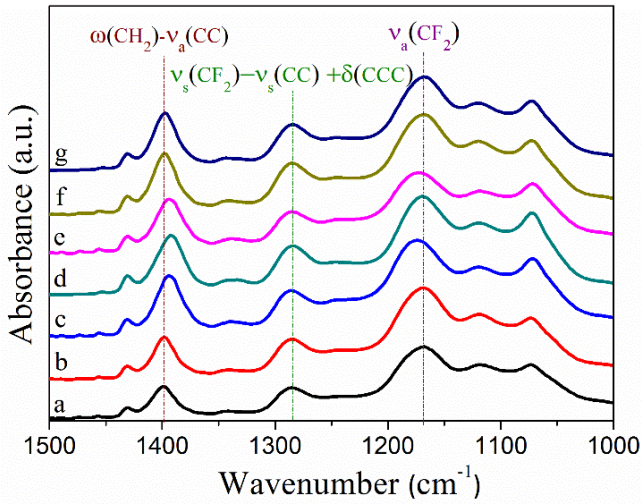

Figure 5.10 FTIR spectra of the PVDF-TrFE films with different degrees of preferred orientation: (a) 170 °C; (b) 175 °C; (c) 190 °C; (d) 190 °C annealed; (e) 205 °C; (f) 210 °C; (g) hot pressed films with random orientation.

Table 5.3 The assignment and position of the characteristic bands for PVDF-TrFE films with different degrees of preferred orientation

	Bands assignment and position (cm^{-1})		
	*$\omega(CH_2)$-$\nu_a(CC)$	*$\nu_s(CF_2)$-$\nu_s(CC)+\delta(CCC)$	*$\nu_a(CF_2)$
170 °C films	1398	1284	1168
175 °C films	1398	1284	1169
190 °C films	1392	1284	1176
190 °C; annealed films	1393	1284	1169
205 °C films	1394	1284	1174
210 °C films	1398	1284	1168
Hot pressed films	1398	1284	1168

*$\boldsymbol{\omega}$, wagging vibration; $\boldsymbol{\nu_a}$, asymmetric stretching vibration; $\boldsymbol{\nu_s}$, symmetric stretching vibration; $\boldsymbol{\delta}$, bending vibration

5.4 Conclusions

Highly crystalline and oriented PVDF-TrFE films can be produced by melt extrusion, with the polymer chain axis along the extrusion direction. The crystalline structure and orientation level can be controlled by changing the extrusion temperature. The optimum extrusion temperature was found to be 190 ℃. The 190 ℃ extruded PVDF-TrFE films exhibited a well stacked edge-on lamella structure with remarkable ferroelectric properties. The coercive field was 23.9 kV/mm and the remnant polarization (0.078 C/m^2) was close to the estimated remnant polarization value assuming perfect in-plane

c-axis orientation and 80% crystallinity (0.082 C/m^2). After annealing at 140 ℃ the crystallinity of the films was increased (~ 90%) and the ferroelectric properties further improved with P_r of 0.099 C/m^2 and E_c of 37.9 kV/mm. This work demonstrates for the first time the extrusion processing of highly aligned ferroelectric copolymer films with pronounced ferroelectric properties, with a significantly low coercive field and high remnant polarization, using extrusion, a highly scalable processing route.

Chapter 6 Nanoscale Interfacial Electroactivity in PVDF/PVDF-TrFE Blended Films with Enhanced Dielectric and Ferroelectric Properties

6.1 Introduction

In this chapter, PVDF was blended with PVDF-TrFE using melt extrusion. On the basis of Chapter 5, melt extruded PVDF-TrFE films exhibited remarkable ferroelectric properties due to high crystallinity and highly preferred crystalline orientation. It was speculated that the presence of PVDF-TrFE could enhance the crystallization of PVDF into β-phase and generate preferred orientation of its polymer chains.

6.2 Experimental details

6.2.1 Materials

PVDF was purchased from Sigma Aldrich Chemical Co. The average molecular weight of the PVDF was about 180 kg/mol (M_w) and 71 kg/mol (M_n). PVDF-TrFE of composition 77/23 mol% was purchased from Piezotech S.A.S, (France). The average molecular weight of the PVDF-TrFE was 210 kg/mol (M_w) and 100 kg/mol (M_n).[142]

6.2.2 Sample preparation

PVDF and PVDF-TrFE were melt-blended using mini-extruder at 205 ℃ and 60 rpm for 10 min. The weight ratios of PVDF/PVDF-TrFE were set as 100/0, 90/10, 80/20, 70/30, 60/40 and 0/100. A slit die with gauge of 200 μm was used to produce films. The

films were collected by a roller at 180 mm/min and ambient temperature. The films were then clamped and annealed at 100 ℃ for 2 hours. The thickness of the films was about 20 μm. For the electrical measurements, gold was vacuum sputtered on both sides of the films to form electrodes.

6.3 Results and discussion

6.3.1 Crystalline phases and preferred orientation of PVDF/PVDF-TrFE blended films

The FTIR spectra of the blended films are shown in Figure 6.1a. For pure PVDF, the strong α-phase characteristic bands at 1211, 1179, 1145, 1066, 976, 871, 854, 795, 764 and 613 cm^{-1} can be seen in line (1). FTIR cannot clearly distinguish the β- from the γ-phase since several of their characteristic bands overlap.[40, 177] For example, the typical 840 cm^{-1} β-phase band could also be a superposition of bands for the β- and γ-phases.[40, 178] However, the exclusive γ-phase bands at 1234, 1117, 833 and 812 cm^{-1} are not apparent in line (1),[57] which means that only the β-phase contributed to the formation of the band at 840 cm^{-1}. To sum up, pure PVDF films mainly crystallized into the α-phase with a small amount of the β-phase (～ 8 wt. % as shown in Figure 6.1b).

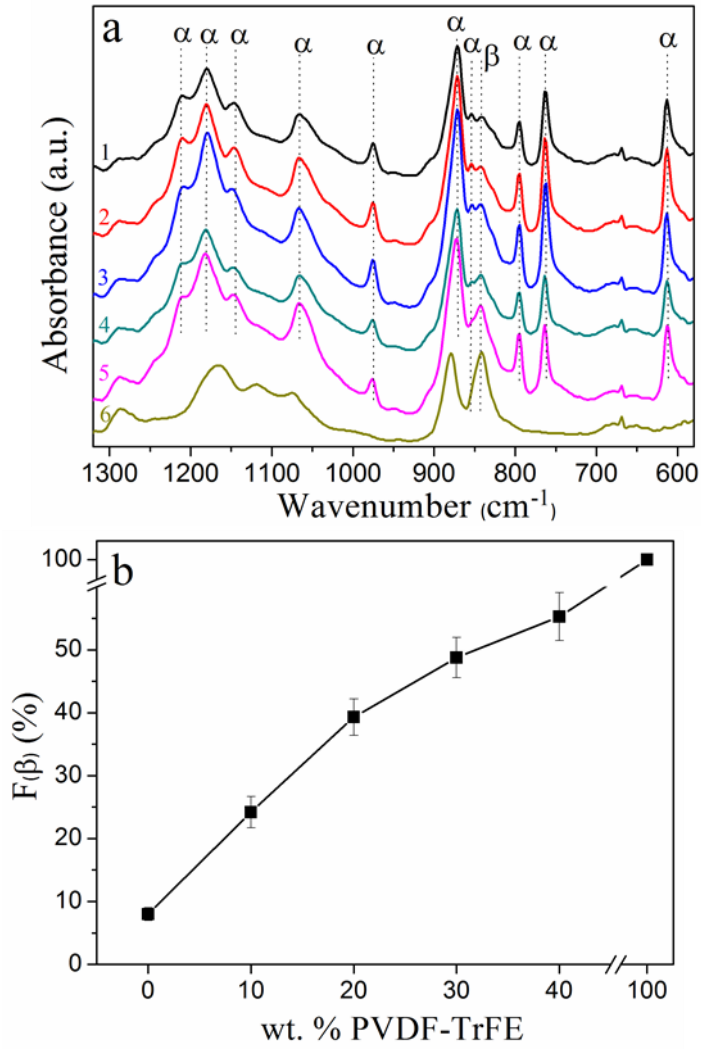

Figure 6.1 (a) FTIR spectra of: (1) PVDF/PVDF-TrFE 100/0; (2) PVDF/PVDF-TrFE 90/10 wt.%; (3) PVDF/PVDF-TrFE 80/20 wt.%; (4) PVDF/PVDF-TrFE 70/30 wt.%; (5) PVDF/PVDF-TrFE 60/40 wt.%; (6) PVDF/PVDF-TrFE 0/100; (b) F(β) of pure PVDF and blended films as a function of wt. % PVDF-TrFE.

For pure PVDF-TrFE, strong characteristic β-phase bands at 1167, 878 and 840 cm^{-1} can be seen in Figure 6.1a line (6). The blended films show a mixture of α- and β-phase. The intensity of the 854 cm^{-1} band (α-phase) was considerably reduced with increasing amount of PVDF-TrFE, while the 840 cm^{-1} band (β-phase) became more obvious. Equation 6.1 was used to quantify the relative fraction of the β-phase (F(β)), assuming

that only the α- and β-phases existed.[179, 180] Equation 6.1 is built on the assumption that FTIR follows the Lambert-Beer law.[179] In Equation 6.1, A_α and A_β correspond to the measured absorbance at 764 cm^{-1} and 840 cm^{-1}, and K_α and K_β are the absorbance coefficients at 764 cm^{-1} and 840 cm^{-1}, the values of which are 6.1×10^4 and 7.7×10^4 cm^2mol^{-1}, respectively [179]. The values of F(β) for the blended films are shown in Figure 6.1b; the value of F(β) of PVDF and PVDF-TrFE are also included. The F(β) value increases to almost 40 wt. % for PVDF/PVDF-TrFE 80/20 wt. % blended films, which shows that the introduction of PVDF-TrFE promotes the crystallization of PVDF into the β-phase.

$$F(\beta) = \frac{A_\beta}{\left(\frac{K_\beta}{K_\alpha}\right)A_\alpha + A_\beta} \qquad 6.1$$

Figure 6.2 shows 1D-WAXD patterns for the pure PVDF, PVDF-TrFE, and the blended films. The three main peaks for the pure PVDF films, at 2θ=17.82°, 18.48° and 20.05°, suggest that PVDF mainly crystallized into the α-phase,[12, 154-159] consistent with the FTIR data which shows no traces of the γ-phase but about 8 wt.% of the β-phase. The shoulder peak for PVDF at 2θ=20.08° also indicates the existence of a small amount of β-phase in pure PVDF films. For the pure PVDF-TrFE films, one strong (110)/(200) reflection peak at 2θ=20.12° was observed. Two other peaks at 2θ= 35.5° and 40.9° were extremely weak and broad, which indicates a high preferred orientation for the pure PVDF-TrFE films.[158]

Similar to PVDF, the blended films showed three XRD peaks. The intensity of the characteristic (020) α-PVDF peak at about 18.5° significantly reduced with PVDF-TrFE content, especially for the blended films containing more than 20 wt. % PVDF-TrFE.

The weakening of this peak indicates that the amount of the α-phase was reduced and/or the preferred orientation of the crystallites increased with the presence of PVDF-TrFE. Combined with the FTIR data, it can be confirmed that there was a reduction in the α-phase and a corresponding increase in the β-phase PVDF.

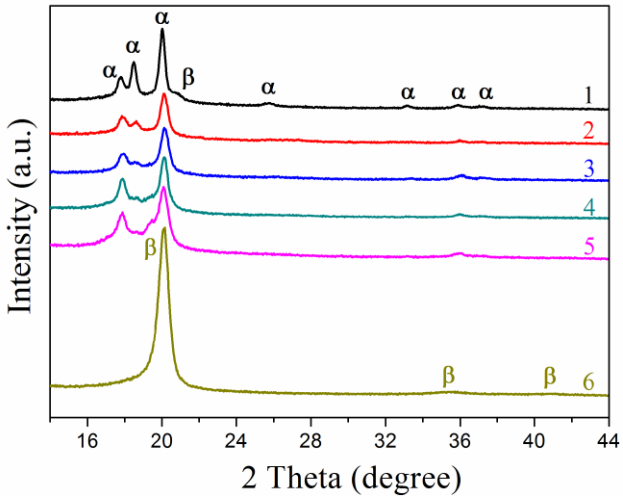

Figure 6.2 1D-WAXD of: (1) PVDF/PVDF-TrFE 100/0; (2) PVDF/PVDF-TrFE 90/10 wt.%; (3) PVDF/PVDF-TrFE 80/20 wt.%; (4) PVDF/PVDF-TrFE 70/30 wt.%; (5)PVDF/PVDF-TrFE 60/40 wt.%; (6) PVDF/PVDF-TrFE 0/100.

The preferred orientation results for the PVDF and PVDF-TrFE films obtained from 2D-WAXD analysis are shown in Figure 6.3. From inner to outer, the WAXD reflections of the PVDF, calculated from Figure 6.3, are 18.1°, 20.0° and 26.6°. The ring at 18.1° consists of the overlapping 17.81° $(100)_\alpha$ and 18.48° $(020)_\alpha$ reflections. The reflection at 26.6°, though not obvious in Figure 6.2, is associated with the $(021)_\alpha$ plane, which is characteristic of the α-phase. As clearly seen in Figure 1d, the crystalline phase of PVDF-TrFE is well oriented, with the $(110)_\beta/(200)_\beta$ reflections concentrated towards the equatorial region, indicating that the polymer chain axis (c-axis) is oriented parallel to the extrusion direction.[181] In comparison, the reflections of PVDF are more

uniformly distributed, implying low preferred orientation. The orientation difference can be explained by the fact that PVDF-TrFE exhibits a longer relaxation time in the melt state than that of PVDF, and therefore showed a more pronounced crystal orientation during flow extension.[182]

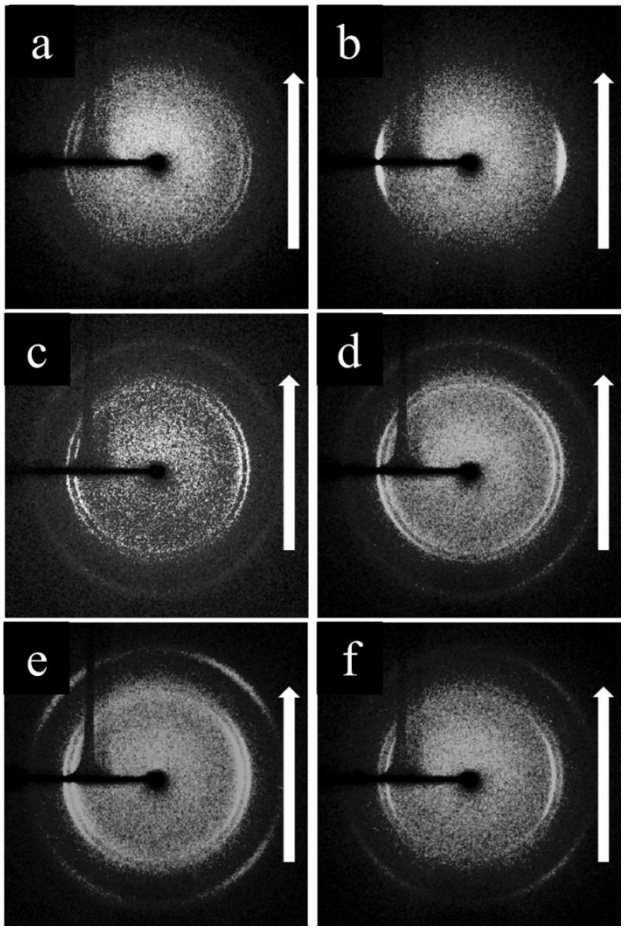

Figure 6.3 2D-WAXD profiles of: (a) pure PVDF; (b) PVDF-TrFE; (c) PVDF/PVDF-TrFE 90/10 wt. %; (d) PVDF/PVDF-TrFE 80/20 wt. %; (e) PVDF/PVDF-TrFE 70/30 wt. %; (f) PVDF/PVDF-TrFE 60/40 wt. %.measured with an incident X-ray beam in the normal direction. Extrusion direction is vertical (indicated by the arrows).

The 2D-WAXD patterns for the blended films are shown in Figure 6.3. From inner to outer, the WAXD profiles exhibit the characteristic reflections of $(100)_\alpha/(020)_\alpha$, $(110)_{\alpha+\beta}/(200)_\beta$ and $(021)_\alpha$ planes at 18.36°, 20.33° and 26.6° respectively. With

increasing amount of PVDF-TrFE, the preferred orientation of the $(110)_{\alpha+\beta}/(200)_{\beta}$ and $(021)_{\alpha}$ reflections are enhanced. The intensity as a function of azimuthal angle from -90° to +90° at the radial position of the $(110)_{\alpha+\beta}/(200)_{\beta}$ and $(100)_{\alpha}/(020)_{\alpha}$ peak for the pure PVDF, PVDF-TrFE and blended films was fitted with a Gaussian function (Figure 6.4).

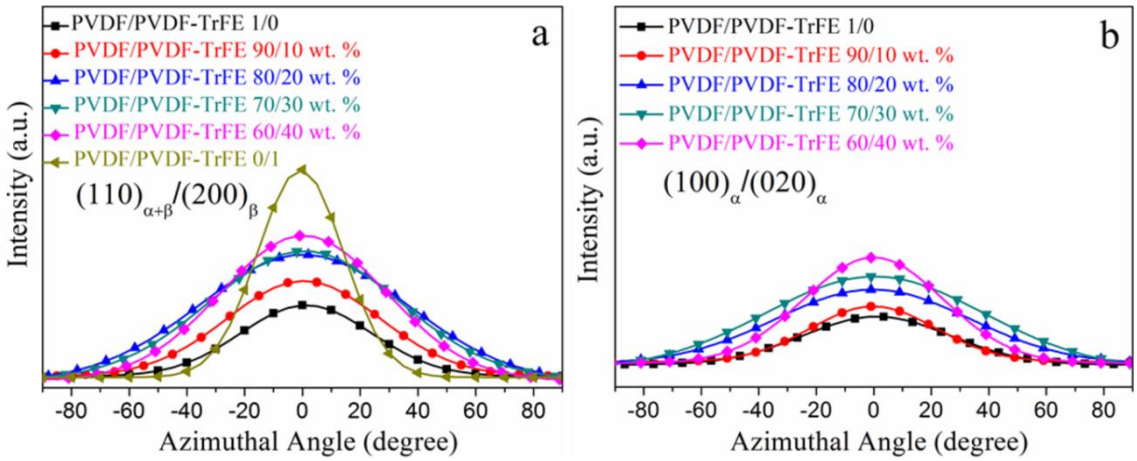

Figure 6.4 Intensity as a function of azimuthal angle at the radial position of: (a) $(110)_{\alpha+\beta}/(200)_{\beta}$ of pure PVDF, PVDF-TrFE and blended films; (b) $(100)_{\alpha}/(020)_{\alpha}$ of pure PVDF and blended films

Pure PVDF films show the least preferred orientation, corresponding to the broadest peak (Figure 6.4). For the blended films the intensity is enhanced and the peak becomes sharper radially and azimuthally with increasing amount of PVDF-TrFE, which shows that blending with PVDF-TrFE leads to increased crystallinity and higher preferred orientation for the PVDF/PVDF-TrFE blended films. Interestingly, the outermost 26.6° $(021)_{\alpha}$ reflection ring of the blended films shows preferred orientation, about 45° from the equatorial direction, which enhanced with increasing the amount of PVDF-TrFE (Figure 6.3). During extrusion, the temperature dropped quickly from 205 ℃ to room temperature, which caused the PVDF and PVDF-TrFE to crystallize simultaneously. The existence of a strong interaction between the two different polymers caused the

chains of the PVDF to orientate in the same direction as the PVDF-TrFE. Figure 6.5 depicts the orientation of the blended films formed during the extrusion processing.

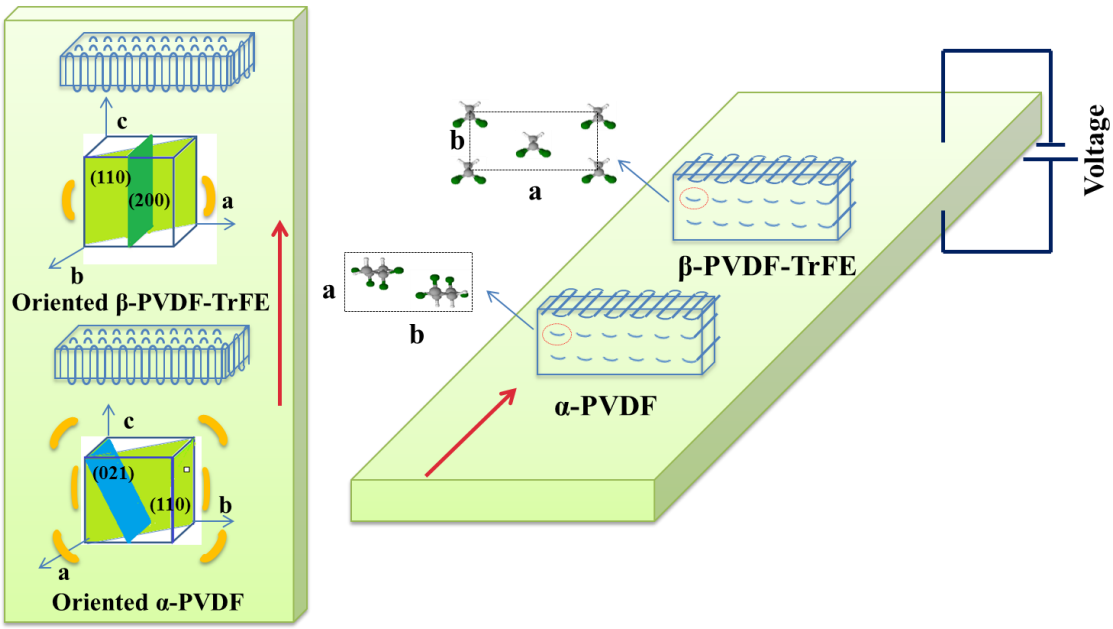

Figure 6.5 Schematic diagram illustrating the orientation of the blended films; the left reflects the film surface and can be used for the understanding of 2D-WAXD; the right reflects the cross-section region. The rectangles represent the lamellae with folded polymer chains. The red arrows indicate the extrusion direction.

6.3.2 Miscibility and crystallization behavior of PVDF/PVDF-TrFE blended films

Morphology studies

It is known that PVDF crystallizes as spherulites when prepared by melt processing,[13] while PVDF-TrFE crystallizes with stacked lamellae structure.[183] Figure 6.6a-b shows the surface morphology of the PVDF and PVDF-TrFE films. The arrow in Figure 6.6 indicates the extrusion direction. For PVDF, the lamellae tend to form spherulites with little preferred orientation, while PVDF-TrFE displays a stacked lamellar morphology.[184]. For the blended films, the two

components crystallize together without obvious phase separation (Figure 6.6c-f). Furthermore, the introduction of PVDF-TrFE produces distortion of the spherulites as can be seen in Figure 6.6f for the PVDF/PVDF-TrFE 60/40 wt. % blended film.

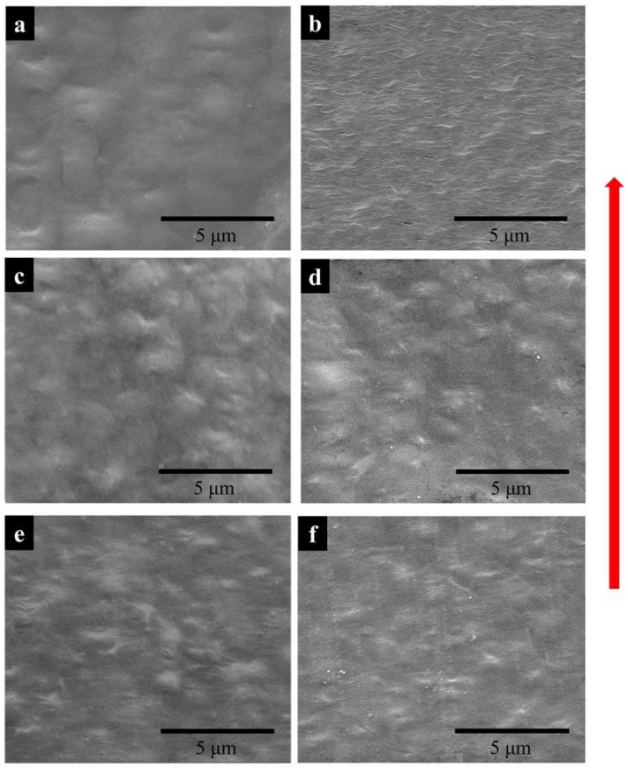

Figure 6.6 SEM of surfaces of: (a) PVDF; (b) PVDF-TrFE; (c) PVDF/PVDF-TrFE 90/10 wt. %; (d) PVDF/PVDF-TrFE 80/20 wt. %; (e) PVDF/PVDF-TrFE 70/30 wt. %; (f) PVDF/PVDF-TrFE 60/40 wt. % (arrow indicates extrusion direction).

Thermal analysis

Figure 6.7 shows the DSC scans of PVDF, PVDF-TrFE and their blends. The first heating curves are displayed in Figure 6.7a. Pure PVDF has two obvious fusion peaks at 161.3±1 ℃ and 169.9±1 ℃, which could be caused by the existence of different crystalline phases or crystallization imperfection. The melting endotherms of α- and β-PVDF are reported to be at almost the same

position, both at around 167 ℃.[179] Combined with the FTIR results for PVDF, it can be deduced that the 169.9 ℃ endotherm peak corresponds to the melting of the well-formed prevalent α-phase crystals, while the 161.3 ℃ peak can be attributed to the melting of imperfect crystalline region.[88, 185] It is seen in Table 1 that pure PVDF exhibits a ΔH_f of 43.1 J/g, indicating the crystallinity of the pure PVDF extruded films is about 41% (ΔH_f for 100% crystalline PVDF is 104.6 J/g[186]).

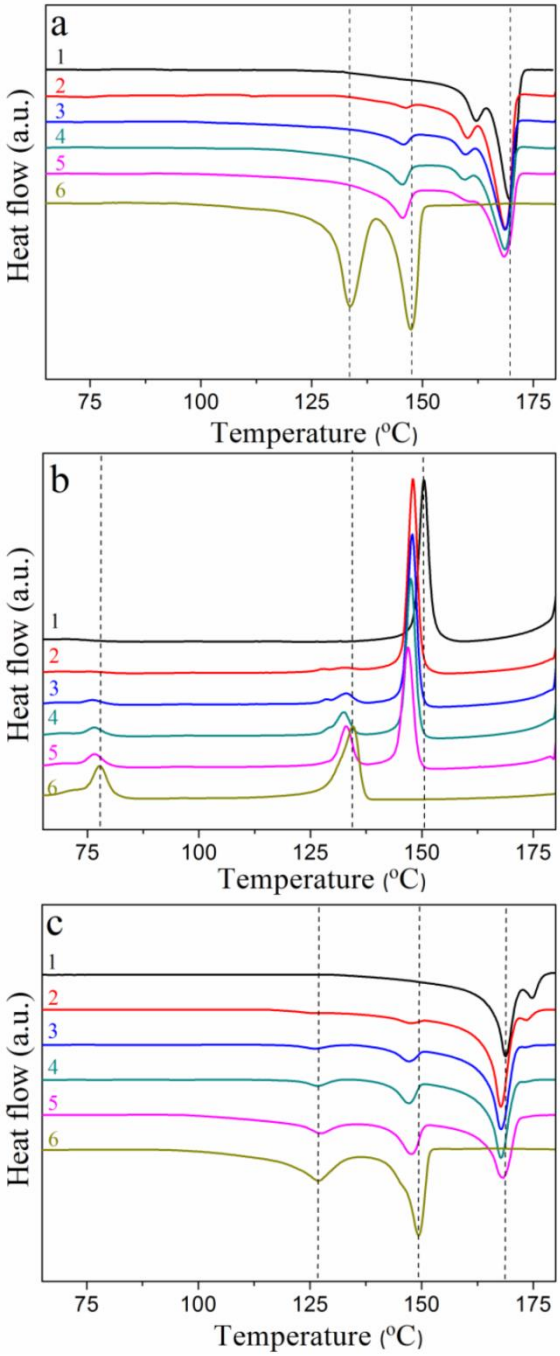

Figure 6.7 (a) First heating; (b) cooling; and (c) second heating DSC graphs of: (1) PVDF/PVDF-TrFE 100/0; (2) PVDF/PVDF-TrFE 90/10 wt.%; (3) PVDF/PVDF-TrFE 80/20 wt.%; (4) PVDF/PVDF-TrFE 70/30 wt.%; (5) PVDF/PVDF-TrFE 60/40 wt.%; (6) PVDF/PVDF-TrFE 0/100.

Apart from its fusion peak at 147.2±1 ℃, pure PVDF-TrFE shows another peak at 133.8±1 ℃ originating from the ferroelectric to paraelectric phase transition

(Curie transition). The ΔH_f of PVDF-TrFE is 29.0 J/g, suggesting a crystallinity of 76% (ΔH_f for 100% crystalline PVDF-TrFE is about 38 J/g[45]). The blended films exhibit three peaks on first heating, corresponding to the fusion peaks for PVDF-TrFE and PVDF, which proves the immiscibility of the two polymers. Interestingly, the Curie transition peak for PVDF-TrFE is diffuse and is apparent only as a shoulder on the lower temperature side of the fusion peak of PVDF-TrFE.

Figure 6.7b shows the cooling DSC curves on cooling after first heating. Pure PVDF has one crystallization peak at 150.6±1 ℃ and pure PVDF-TrFE shows two peaks at 134.6±1 ℃ and 77.8±1 ℃, resulting from the crystallization and the paraelectric to ferroelectric phase transition, respectively. All blended films exhibit three peaks. The crystallization temperatures of PVDF and PVDF-TrFE and the Curie transition in the blended films are slightly lower than those of the pure components.

Figure 6.7c shows the second heating DSC curves of PVDF, PVDF-TrFE and their blends. During the second heating pure PVDF has two fusion peaks at 168.9±1 ℃ and 174.8±1 ℃, indicating a mixture of α- and γ-phases.[177] Further evidence for the presence of the γ-phase can be found in the FTIR data presented in Figure 6.8. With regard to pure PVDF-TrFE, the peak value of the Curie transition shifts to a lower temperature (127±1 ℃) when compared to the first heating (133.8±1 ℃). The higher Curie point in the first heating indicates that the pure PVDF-TrFE crystallized into highly oriented ferroelectric crystals through the extrusion method.[187] For the blended films, the Curie transition peak was

diffuse in the first heating curves, however, a small, but clear, peak can be seen in the second heating curves. It is shown in Table 6.1 that $\Delta H_{f\ PVDF}$ of pure PVDF and blended samples during first heating are larger than those of second heating, while being lower for $\Delta H_{f\ PVDF\text{-}TrFE}$, which indicates the existence of interactions between PVDF and PVDF-TrFE in the extruded blended films. The formed crystallites exhibited similar structure and were intimately correlated. The Curie transition is achieved by the formation of gauche bonds, thereby polymer chains in PVDF-TrFE undergo severe twisting and/or tilting[187] which requires adequate space to accomplish this. However, the surroundings of PVDF crystals and the intimate coexistence of the two components restrict the space to accomplish the transition. PVDF and PVDF-TrFE crystallized more freely in the DSC slow cooling process (cooling rate 5 °C/min), which results in more phase separation and less interactions, making the Curie transition peaks more obvious than those of the extruded blended films in DSC heating curves.

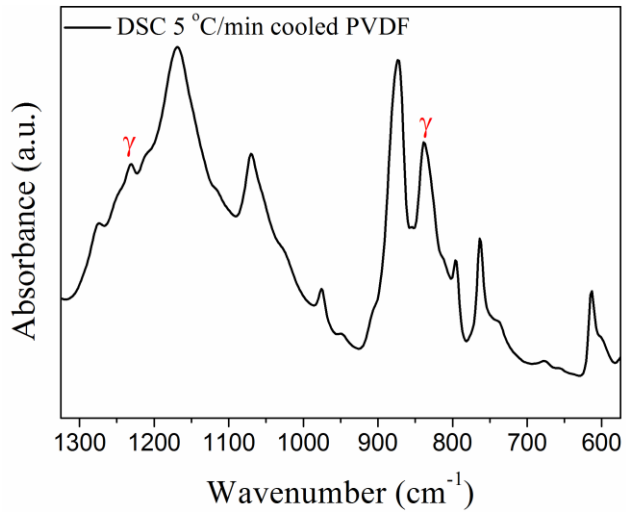

Figure 6.8 FTIR data for PVDF crystallized during DSC cooling, indicating the formation of γ-phase.

Table 6.1 The enthalpy of Curie transition and fusion of PVDF/PVDF-TrFE blended films acquired from first heating and second heating DSC curves.

	Enthalpy values of first heating (J/g)			**Enthalpy values of second heating (J/g)**		
PVDF/ PVDF-TrFE	[a)] ΔH_c PVDF-TrFE	ΔH_f PVDF-TrFE	$\Delta H_{f\ PVDF}$	ΔH_c PVDF-TrFE	ΔH_f PVDF-TrFE	$\Delta H_{f\ PVDF}$
100/0	−	−	46.3±3	−	−	43.1±2
90/10	−	7.0±1	38.0±2	9.2±1	13.1±1	31.1±1
80/20	−	6.6±1	36.4±3	9.0±1	13.6±1	32.7±1
70/30	−	17.1±2	33.0±3	7.8±1	19.6±1	32.0±1
60/40	−	15.6±1	32.5±2	12.2±2	21.0±1	31.9±1
0/100	28.7±2	29.0±3	−	26.4±3	28.8±2	−

[a)] $\Delta \boldsymbol{H}_{\mathbf{c\ PVDF\text{-}TrFE}}$: enthalpy of Curie transition of PVDF-TrFE; $\Delta \boldsymbol{H}_{\mathbf{f\ PVDF\text{-}TrFE}}$ and $\Delta \boldsymbol{H}_{\mathbf{f\ PVDF}}$: enthalpy of fusion of PVDF-TrFE and PVDF, respectively.

The above results correlated to both crystallization and morphological studies strongly demonstrate the intimate interactions between the PVDF and PVDF-TrFE. More detailed investigations of isothermal crystallization at 150 °C (PVDF crystallization temperature) and 135 °C (PVDF-TrFE crystallization temperature) were undertaken.

The DSC data recorded during isothermal crystallization at 150 °C is shown in Figure 6.9a and Figure 6.10a, and the morphology of the films is shown in Figure 6.11a. No crystallization of PVDF-TrFE occurred at 150 °C (Figure 6.9). It is evident that the rate of crystallization of the PVDF at 150 °C was increased by the addition of PVDF-TrFE

(in melt state). This is different to what is reported for PVDF/poly(1,4-butylene adipate) (PBA) blends where the crystallization rate of PVDF was reduced due to the presence of PBA.[188] To understand these differences, it is necessary to consider the morphologies of the microstructures. In the PVDF/PBA system, PVDF crystallized into progressively larger spherulites with increasing PBA content, however, in our PVDF/PVDF-TrFE blends the growth of PVDF spherulites was restricted. The isothermally crystallized PVDF showed fine spherulites. The spherulites that formed in the blends samples were smaller and less perfect compared to those in PVDF (Figure 6.11a), which is consistent with the morphology of extruded films. On the basis that there was no crystallization of PVDF-TrFE at 150 °C because the temperature was above its melting point, the enthalpy of crystallization of the blends were normalized in terms of the PVDF content ($\Delta H_{c/PVDF}$). Figure 6.10a shows that the normalized values of $\Delta H_{c/PVDF}$ for both pure PVDF and the blends are similar regardless of weight ratio, indicative of almost no hindrance to the degree of crystallinity of PVDF due to the introduction of PVDF-TrFE.

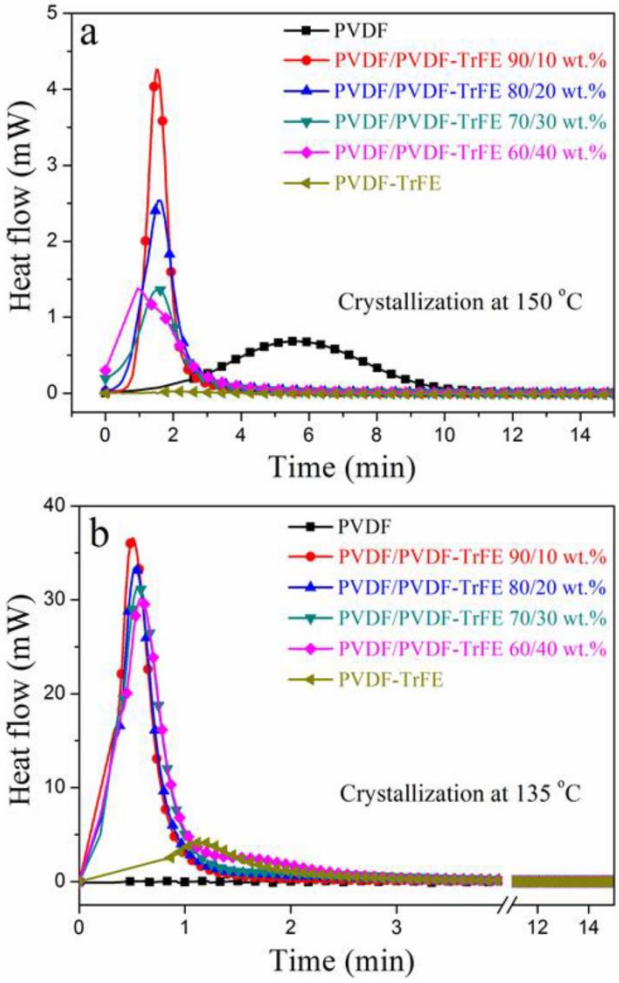

Figure 6.9 DSC heat flow as a function of time recorded during isothermal crystallization at (a) 150 °C and (b) 135 °C.

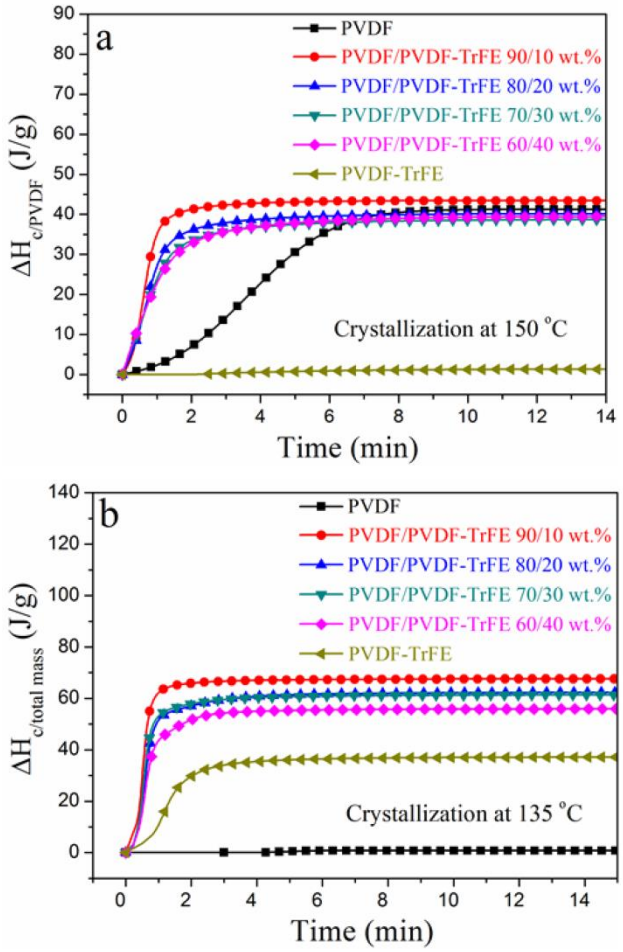

Figure 6.10 The enthalpy of crystallization (ΔH_{cry}) acquired by integrating heat flow recorded during isothermal crystallization as a function of time at: (a) 150 °C and (b) 135 °C. The ΔH_c values at 150 °C for blends materials were normalized by PVDF.

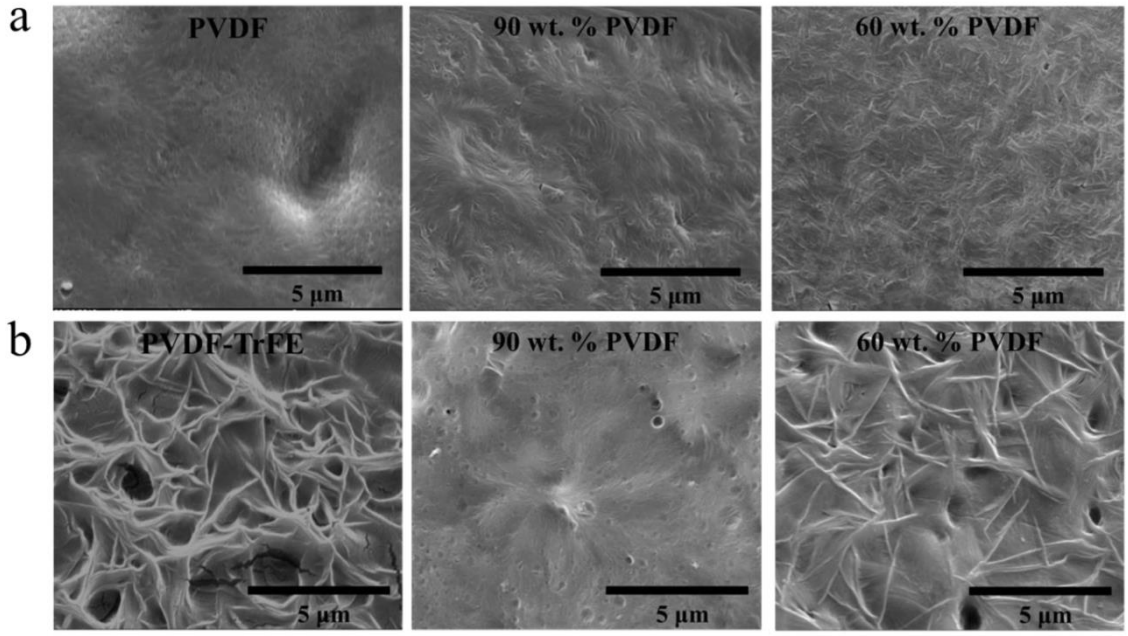

Figure 6.11 SEM morphology images for samples isothermally crystallized at (a) 150 °C and (b) 135 °C.

The non-normalized raw DSC data for samples isothermally crystallized at 135 °C are shown in Figure 6.9b and Figure 6.10b. Pure PVDF-TrFE exhibited a maximum ΔH_c of approximately 37 J/g, which represents almost complete crystallization using the reported enthalpy of fusion for 100 % crystalline PVDF-TrFE (～ 38 J/g).[45] During the isothermal crystallization at 135 °C, the PVDF continued to crystallize as demonstrated by the large enthalpies of the blends. On the other hand, the rate of crystallization at 135 °C of the PVDF-TrFE was increased in the blends compared to the pure copolymer. This can be explained by the PVDF crystallites acting as nucleation sites for the crystallization of the PVDF-TrFE. Figure 6.11b shows the morphology of samples isothermally crystallized at 135 °C, with needle-like PVDF-TrFE crystals embedded in the matrix of PVDF, which did not crystallize into a spherulitic structure. To conclude, the DSC data (Figures 6.7, 6.9-10 and Table 6.1) and the microstructural analysis (Figures 6.6, and 6.11) clearly shows that synergistic effects occurred at the nanoscale

in the blended materials at the interface between the two immiscible polymers that strongly affected the kinetics of crystallization and the microstructures that formed.

6.3.3 Electric properties of PVDF/PVDF-TrFE Blended Films

Dielectric properties

Figure 6.12a-b shows the frequency dependence of the dielectric permittivty and loss of PVDF, PVDF-TrFE and their blends. The blended films show larger dielectric constant values than those of the two pure components. One explanation for this could be enhanced interfacial polarization at the PVDF and PVDF-TrFE interfaces. Another possible explanation might be the preferred orientation of the polymer chains in the amorphous region, especially at the crystalline-amorphous interfaces.[65] The addition of PVDF-TrFE in the blended films increased the crystalline preferred orientation of the PVDF, thus causing the chains in the amorphous region to orient along the same direction, which gives rise to higher dielectric constant values than for pure PVDF.

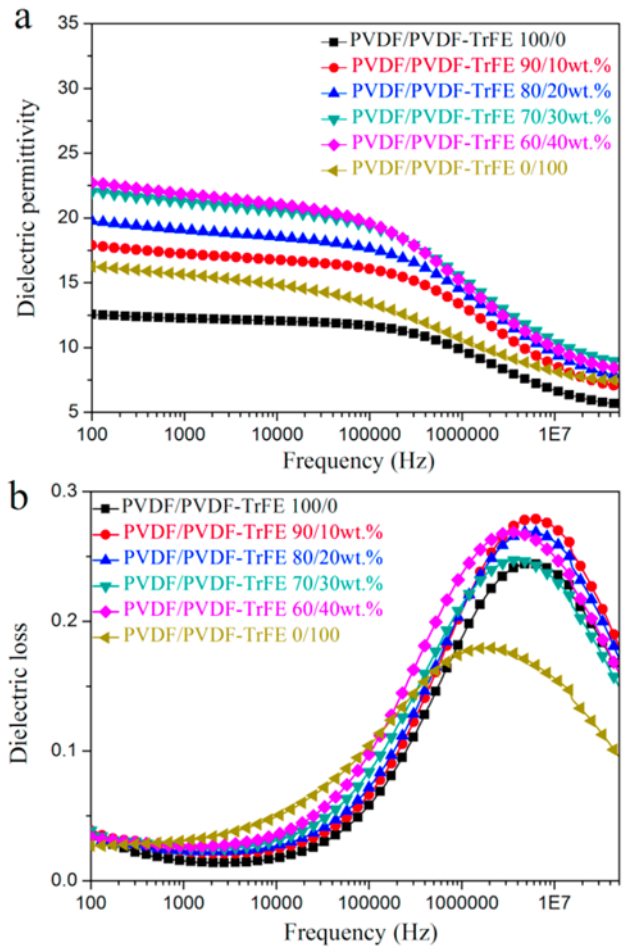

Figure 6.12 Frequency dependence of (a) dielectric permittivty and (b) dielectric loss for pure PVDF, PVDF-TrFE and blended films as a function of frequency.

Figure 6.13 shows the temperature dependent dielectric spectra for pure PVDF, PVDF-TrFE and their blends. All of the samples exhibit dielectric loss peaks at about 0 °C and 100 kHz, which is ascribed to the glass transition.[189] The dielectric permittivity of PVDF-TrFE shows an obvious peak at about 140 °C, and the peak position is frequency invariant, which suggests the existence of a Curie transition.[190] The blended films with 40 wt. % PVDF-TrFE show an inflexion in the permittivity and loss data consistent with a Curie transition (Figure 6.13 d).

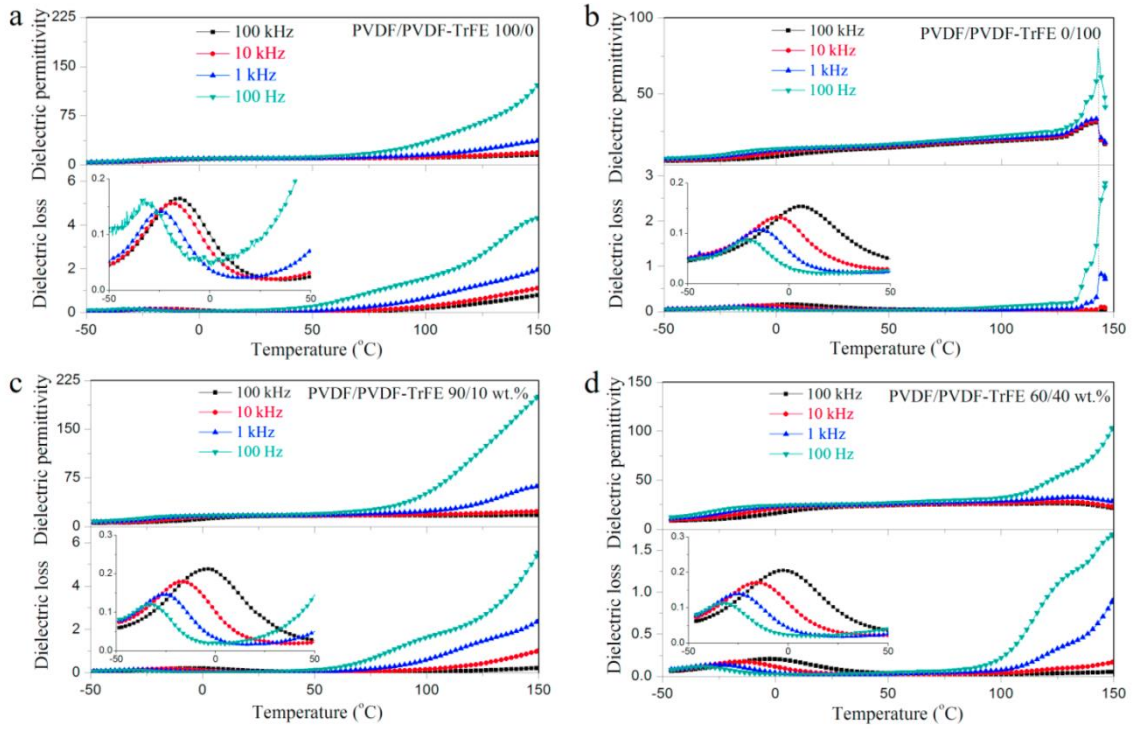

Figure 6.13 Temperature dependence of the dielectric permittivity and loss of: (a) PVDF; (b) PVDF-TrFE; (c) PVDF/PVDF-TrFE 90/10 wt. %; (d) PVDF/PVDF-TrFE 60/40 wt. %.

Ferroelectric properties

Figure 6.14 shows the ferroelectric polarization hysteresis loops for PVDF, PVDF-TrFE and the blended films. The P-E loops are saturated, which was confirmed by the invariance of the current peak position beyond a certain maximum applied electric field (~ 120 kV/mm). The PVDF-TrFE exhibits superior ferroelectric properties, with a coercive field of about 35 kV/mm and a remnant polarization of 0.09 C/m^2, which is attributed to highly preferred crystalline orientation and high crystallinity.[181] In the case of PVDF, a ferroelectric response was observed, confirmed by the presence of weak current peaks. The ferroelectric behaviour of PVDF is attributed to the presence of the small amount of β-phase (∼8 wt. %) and the transformation of the paraelectric α-phase to the ferroelectric δ-phase during the measurement.

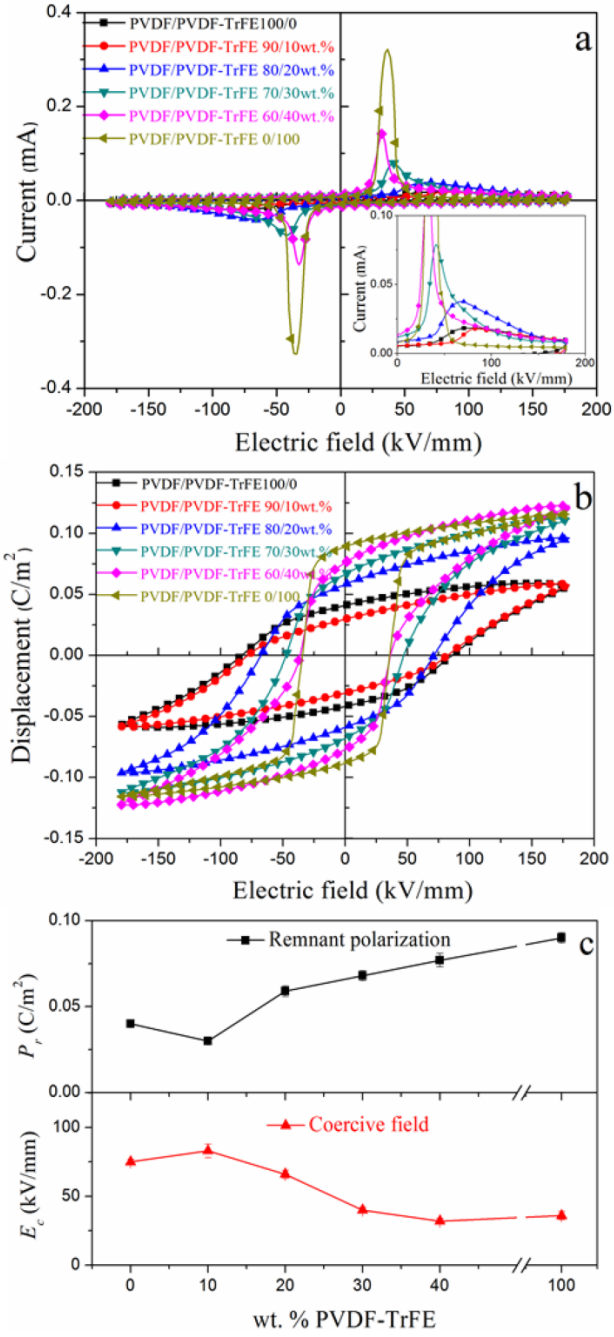

Figure 6.14 Ferroelectric properties of: (1) PVDF/PVDF-TrFE 100/0; (2) PVDF/PVDF-TrFE 90/10 wt.%; (3) PVDF/PVDF-TrFE 80/20 wt.%; (4) PVDF/PVDF-TrFE 70/30 wt.%; (5) PVDF/PVDF-TrFE 60/40 wt.%; (6) PVDF/PVDF-TrFE 0/100: (a) Current-Electric field I-E curves; (b) Polarization -Electric field P-E loops; (c) variations of remnant polarization P_r and switching field E_c as a function of wt. % PVDF-TrFE (data collected at E=180 kV/mm).

With regard to the blended films, the coercive field decreased from 83 kV/mm to 32 kV/mm with increasing the amount of PVDF-TrFE from 10 wt. % to 40 wt. % as a result of blending. The remnant polarization of the PVDF is apparently higher compared with 10 wt. % PVDF-TrFE due to the leakage current in the pure PVDF, making the remnant polarization of PVDF unrealistically high (inset in Figure 6.14a). Such leakage currents could be ascribed to the gaps or voids formed between large PVDF spherulites.[141] The introduction of PVDF-TrFE enhanced the remnant polarization for the blended films from 0.030 to 0.077 C/m^2 with increasing the amount of PVDF-TrFE from 10 to 40 wt. % (Figure 6.14c). On the basis of the data from the structural characterization, the addition of PVDF-TrFE enhanced the crystallization of ferroelectric β-phase in the blended films. This alone would not explain the enhanced ferroelectric properties of the blended films.

The theoretical value of remnant polarization for blends with 40 wt. % based on a simple rule of mixtures was calculated using following equation: $P_{\mathrm{rblends}} = \varphi_{\mathrm{PVDF}} \times P_{\mathrm{rPVDF}} + \varphi_{\mathrm{PVDF\text{-}TrFE}} \times P_{\mathrm{rPVDF\text{-}TrFE}}$, where φ and P_{r} are the volume fraction and measured remnant polarization for pure PVDF and PVDF-TrFE extruded samples. The calculated value for blends with 40 wt. % is only 0.058 C/m^2, about 25% lower than the experimental value. Similar conditions existed in the 20 wt. % and 30 wt. % blends, where the calculated values were about 20% less compared with the experimental values. Combined with the diffuse Curie transition and larger dielectric constants observed the blended films, the interaction between the two polymers and the interfaces between them could explain the enhanced ferroelectric properties for the blended films. The interfacial polarization contributes to the higher remnant polarization and more

contributions are generated at high electric fields, as indicated by the large saturated polarization of blends with 40 wt. % PVDF-TrFE.

6.4 Conclusions

Despite the immiscibility of PVDF and PVDF-TrFE, as demonstrated by the DSC results, they intimately crystallize on a fine scale (~ 40 nm) without the appearance of distinct phase separation. The rate of crystallization of PVDF and PVDF-TrFE is increased as a result of blending, as suggested by isothermal crystallization studies. With increasing amount of PVDF-TrFE, the blended films have more β-phase and increased preferred orientation, more than would be expected based on a simple rule of mixtures. Due to interfacial polarization, PVDF/PVDF-TrFE blended films have larger dielectric constant than those of the two pure components. Furthermore, the ferroelectric properties of the blended films were enhanced by the introduction of PVDF-TrFE, more than would be expected based on a simple rule of mixtures. The switching field decreased (from 75 to 32 kV/mm), while the remnant polarization increased (from 0.040 to 0.077 C/m^2) with increasing amount of PVDF-TrFE from 0 to 40 wt. %. The Curie transition was suppressed in the blended films, which may lead to increased high temperature stability for piezoelectric applications.

Chapter 7 Crystallization Kinetics and Enhanced Dielectric Properties of Free Standing PVDF/$BaTiO_3$ Composite Films

7.1 Introduction

Ferroelectric composites, integrating dielectric ceramic fillers with mechanically flexible polymers, are promising materials for flexible electronic applications. Plenty of research has demonstrated the enhanced dielectric and ferroelectric properties of composite materials. However, the mechanisms responsible for these enhancements are not completely understood. Herein, the typical dielectric materials, PVDF and $BaTiO_3$ (BTO), were used to study the effect of dielectric filler on the crystallization, phase transformation and dielectric properties of PVDF.

7.2 Experimental details

7.2.1 Materials

PVDF pellets were purchased from Sigma Aldrich Chemical Co. The average molecular weight of the PVDF was about 180 kg/mol (M_w) and 71 kg/mol (M_n). Tetragonal $BaTiO_3$ (BTO) particles with an average particle size of 300 nm were purchased from Nanostructured & Amorphous Materials, Inc. The density of the PVDF and BTO particles was 1.78 and 5.85 g/cm^3, respectively, according to the suppliers. All of the materials were used without post-treatments.

7.2.2 Sample preparation

The PVDF_BTO composites were firstly melt-blended using micro compounder at 210 ^{o}C and 100 rpm for 10 mins and then collected using a micro cast film line. These extrusion conditions were found to be optimum to produce good dispersion of the BTO particles and high crystallinity of the PVDF. The volume content of BTO in the as-extruded films was varied from 0.15 to 10 vol. %. Samples of dimensions 50×15 mm^2 were cut from the as-extruded films and solid state drawn at 100 ^{o}C and 120 ^{o}C at 10 mm/min. The chosen drawing temperatures were appropriate to enable significant chain mobility and transform the polymer to ferroelectric β-phase. The draw ratio of the films was calculated by dividing the extension by the original length.

The thickness of drawn films was about 25 μm, measured using a digital micrometer. Gold electrodes were evaporated on both sides of the films to enable dielectric and ferroelectric measurements.

7.3 Results and discussion

7.3.1 Effect of BTO addition on the PVDF crystallization

The one dimensional XRD patterns of the BTO powder, and the as-extruded PVDF and composite films are shown in Figure 7.1. The BTO powder diffraction data matches the JCPDS PDF#75-0460 data file with characteristic peaks at 2θ=44.9° (002) and 45.4° (200) and tetragonal structure (Figure 7.1(1)). The diffraction peaks in Figure 7.1(2) at 2θ=17.8° (100), 18.6° (020) and 20.0° (110) were assigned to the non-ferroelectric α-PVDF. The characteristic peak of the ferroelectric β-phase at 2θ=20.8° corresponding to the (110)/(200) reflections could not be observed as an obvious peak, but appeared as a

small shoulder in the pure PVDF and composite films, which suggests the α-phase is the predominant crystalline phase. Our previous studies showed that extruded PVDF can crystallize into small amounts of β-phase (~ 8 wt. %) as determined by FTIR technique.[191]

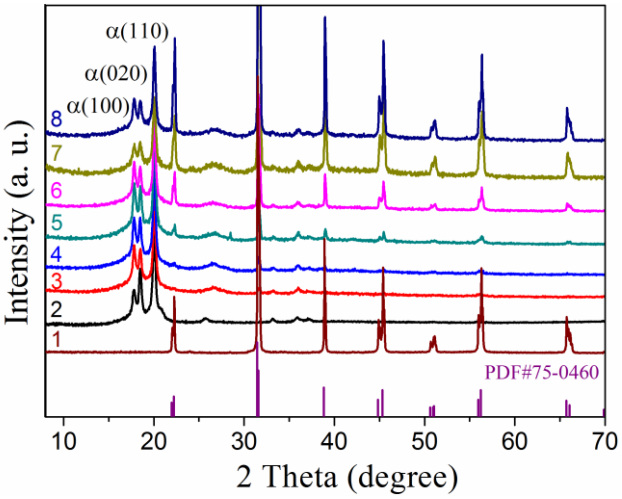

Figure 7.1 XRD patterns of: (1) BTO; (2) PVDF; (3) PVDF_BTO 0.15 vol. %; (4) PVDF_BTO 0.5 vol. %; (5) PVDF_BTO 1 vol. %; (6) PVDF_BTO 3 vol. %; (7) PVDF_BTO 5 vol. % and (8) PVDF_BTO 10 vol. %

Figure 7.2 shows SEM images of the surface of as-extruded pure PVDF and composite films. Bright white BTO particles with an average diameter of 300 nm were well dispersed in the dark grey PVDF matrix. All of the samples displayed spherulite morphology, suggesting the crystallization of α-phase, which is consistent with the XRD data (Figure 7.1). Composites with BTO content of 0.15, 0.5 vol. % crystallized into larger spherulites (diameter ~ 10 μm) compared to pure PVDF (diameter ~ 3 μm). With increasing BTO content from 5 and 10 vol. %, no clear spherulite boundaries were observed and the BTO particles started to agglomerate. However, the composites showed no holes or pores, suggesting good compatibility between the BTO particles and

PVDF matrix. There was no apparent preferred orientation in relation to the extrusion directions for any of the films.

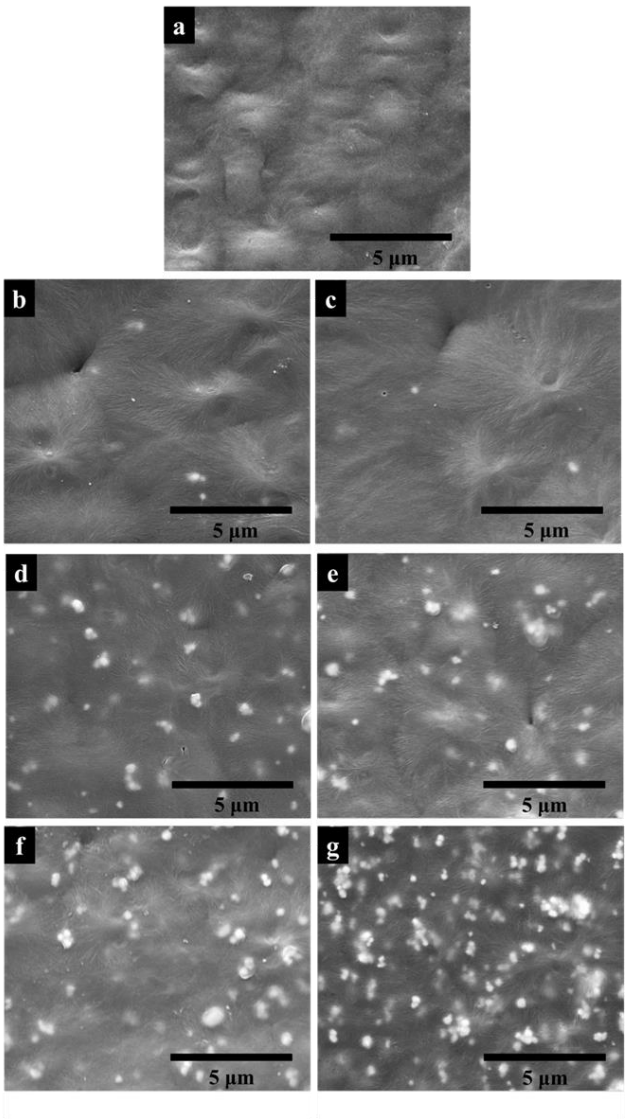

Figure 7.2 SEM images for the as-extruded composites films filled with different BTO content: (a) pure PVDF; (b) PVDF_BTO 0.15 vol. %; (c) PVDF_BTO 0.5 vol. %; (d) PVDF_BTO 1 vol. %; (e) PVDF_BTO 3 vol. %; (f) PVDF_BTO 5 vol. %; (g) PVDF_BTO 10 vol. %.

Figures 7.3 shows DSC temperature scans and isothermal crystallization data for the as-extruded PVDF and composite films. The values of melting (T_m) and crystallization (T_c) temperatures are listed in Table 7.1, which also includes the crystallinity (X_c), which

was determined from the enthalpy of fusion. The PVDF and composite films exhibit two fusion peaks during the first heating DSC temperature scan (Figure 7.3a). The broader peak at lower temperature corresponds to the melting of smaller and/or imperfect crystals. [191]As shown in Table 7.1, the position of the main fusion peak (T_m) was hardly altered by the addition of BTO particles (~ 169 °C). Similarly, a crystallinity of about 50%, typical for PVDF, [191] was found, independent of the BTO content. Figure 7.3b depicts the cooling DSC temperature scan after first heating. The T_c of pure PVDF was 142.1 °C, and barely varied with addition of less than 5 vol. % of BTO particles. The T_c increased to 143.5 and 146.2 °C in correspondence of 5 and 10 vol. % of BTO particles. The crystallization of semi-crystalline polymers involves two steps, crystal nucleation and crystal growth; a high content of BTO (> 5 vol. %) increased the amount of nucleation sites, which accelerated the crystallization of the PVDF and made it occur at a higher temperature than that of pure PVDF.

Isothermal crystallization experiments were conducted to understand the effect of BTO on the crystallization of PVDF. Due to the higher T_c of the PVDF composites containing 5 and 10 vol. % BTO, the isothermal crystallization temperature was chosen as 150 °C. The time dependence of the crystallinity (X_c) for the as-extruded PVDF and composite films are shown in Figure 7.3c. For all of the samples, the crystallinity firstly increased with time before reaching a plateau. During isothermal crystallization at 150 °C, pure PVDF achieved up to 38% crystallinity, which is lower than that of the extruded films due to the onset crystallization temperature. Compared to the pure PVDF, the composite samples exhibited higher crystallinity regardless of filler content. The crystallinity firstly increased with increasing BTO content up to 3 vol. %, then decreased at higher BTO content (5 vol. % and 10 vol. %).

Another characteristic shown in Figure 7.3c is the reduced time needed to reach the plateau for the composites with the higher BTO contents (5 and 10 vol. %). The isothermal crystallization behaviour is well described by the Avrami equation[192], as shown in Equation 7.1, where X_t is the relative crystallinity at a corresponding time *t*, which is equal to the absolute crystallinity X_c, crystallized at time *t*, divided by the final maximum crystallinity; *K* is a constant correlated to the overall crystallization rate; *n* is the Avrami exponent which describes both the nucleation nature (n_t) and crystal growth geometry (n_c) (and Equation (7.2)). Values of *K* and *n* for pure PVDF and the composite films were determined by fitting the plots of ln[-ln(1- X_t)] against ln*t* using Equation (7.3). The fitting curves are shown in Figure 7.3d and the related crystallization kinetics parameters are listed in Table 7.1, where the $t_{1/2}$ is defined as the required time to complete half of the crystallization, and is used to evaluate the crystallization rate.

$$X_t = 1 - \exp(-Kt^n) \qquad 7.1$$

$$n = n_t + n_c \qquad 7.2$$

$$\ln[-\ln(1 - X_t)] = \ln K + n\ln t \qquad 7.3$$

$$t_{1/2} = \left(\frac{\ln 2}{K}\right)^{\frac{1}{n}} \qquad 7.4$$

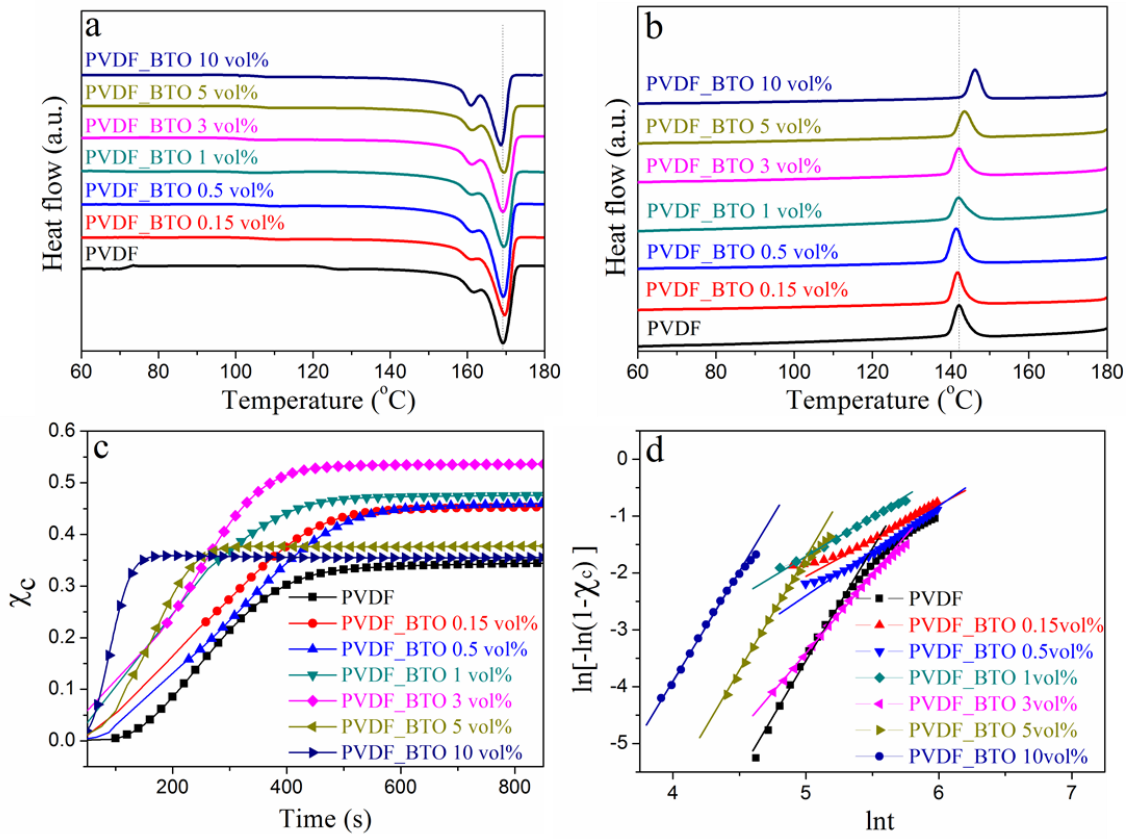

Figure 7.3 (a) First heating DSC temperature scan; (b) cooling DSC temperature scan; (c) crystallinity against time during isothermal crystallization at 150 °C; (d) fitted Avrami results. The enthalpy of fusion for a fully crystalline PVDF is 104.6 J/g.[186]

Table 7.1 Characteristic temperatures and thermodynamic values obtained from the DSC data. Melting temperature T_m and crystallinity X_c were determined from the first heating DSC curves; crystallization temperature T_c was determined from the cooling DSC curves and crystallinity $X_{c\text{-}iso}$, Avrami n and $t_{1/2}$ were calculated on the basis of DSC isothermal crystallization data.

	T_m (°C)	X_c	T_c (°C)	$X_{c\text{-}iso}$	Avrami n	$t_{1/2}$ (s)
PVDF	168.3±1	50.7±2%	142.1±1	38.6±3%	3.8±0.1	331
PVDF_BTO 0.15 vol.%	168.7±2	51.7±2%	141.7±1	45.4±2%	1.4±0.5	327
PVDF_BTO 0.5 vol.%	168.9±2	52.0±3%	141.6±1	46.4±3%	1.7±0.2	344
PVDF_BTO 1 vol.%	168.9±2	48.3±3%	142.0±2	47.9±1%	3.1±0.4	207
PVDF_BTO 3 vol.%	168.8±1	50.0±4%	142.0±1	53.7±4%	3.6±0.2	240
PVDF_BTO 5 vol.%	168.7±1	49.6±2%	143.5±1	38.0±2%	3.5±0.4	205
PVDF_BTO 10 vol.%	168.6±1	50.4±2%	146.2±1	35.7±1%	3.9±0.2	136

The Avrami equation is built on the ideal assumptions of: homogenous nucleation; no change in the crystal shape; constant crystallization rate and volume of polymer; and no occurrence of secondary crystallization.[193] However, real isothermal crystallization is more complicated than this, and all of the details cannot be precisely revealed by the Avrami equation. Consequently, the Avrami exponent n values, shown in Table 7.1, are not integers (as one would expect) and are highly scattered. Pure PVDF exhibited a value of about 4 and crystallized into spherulites (Figure 7.4a), indicating homogenous nucleation (n_t = 1) and three dimensional spherulite crystals (n_c = 3). The composites samples, however, showed two different behaviours. The composites filled with the

lower BTO contents of 0.15, 0.5 vol. % had a *n* value of about 2, suggesting the crystallization of 2-dimensional crystals ($n_c = 2$) and heterogeneous nucleation ($n_t = 0$). The *n* was in the range of 3 to 4 for composites filled with BTO contents higher than 1 vol. %, suggesting the crystallization of spherulites ($n_c = 3$) and heterogeneous nucleation ($n_t = 0$).

The morphologies of the samples crystallized at 150 °C are shown in Figure 7.4, where PVDF crystallized into spherulites, consistent with an Avrami exponent *n* of about 4 (Figure 7.4a). A similar spherulite structure was maintained for the composites filled with 0.15 vol. % of BTO particles (Figure 7.4b), which is contrary to the Avrami exponent *n* ranging from 1 to 2. This contradiction can be explained by the larger banded spherulites formed in the PVDF_BTO 0.5 vol. % composites, the diameter of which were about 50 μm, with concentric rings along the radial direction (Figure 7.4c inset). Banded spherulite structure has been reported in various semi-crystalline polymers.[194-196]

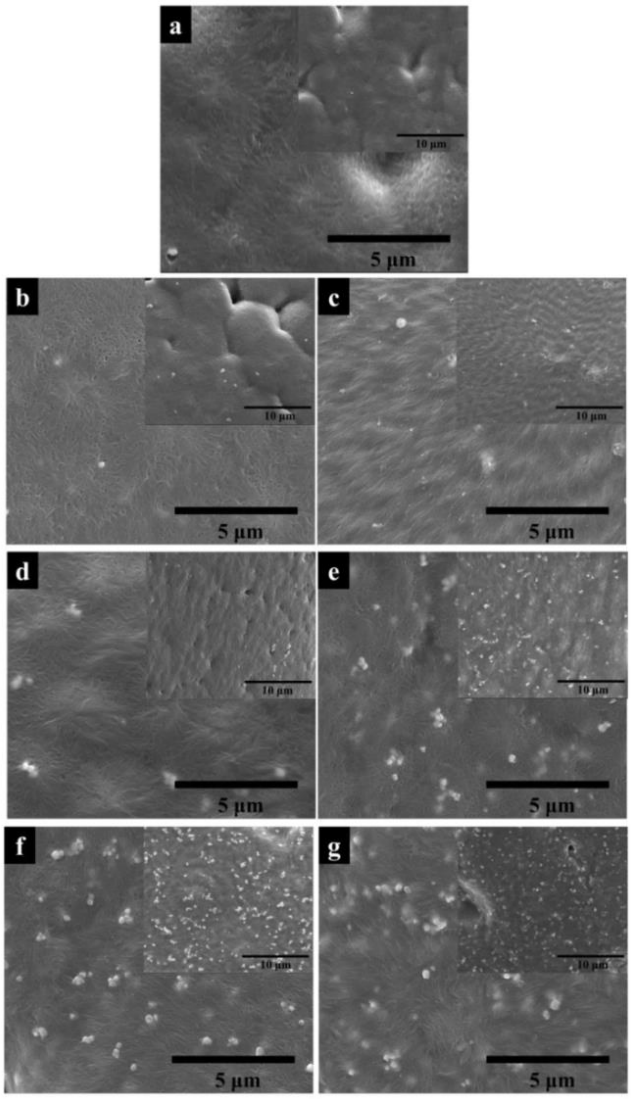

Figure 7.4 SEM images of samples isothermally crystallized at 150 °C: (a) pure PVDF; (b) PVDF_BTO 0.15 vol. %; (c) PVDF_BTO 0.5 vol. %; (d) PVDF_BTO 1 vol. %; (e) PVDF_BTO 3 vol. %; (f) PVDF_BTO 5 vol. %; (g) PVDF_BTO 10 vol. %.

The BTO particles served as nucleating agents for the crystallization of PVDF. For composites loaded with a small content of BTO fillers (up to 0.5 vol. %), the heterogeneous nucleus of inorganic particles provided enough space for the growth of the PVDF crystals, thus forming the large ring banded spherulites. The Avrami exponent *n* of PVDF_BTO 0.5 vol. % was less than 2, which is consistent with the structure of the twisted lamellae in the banded spherulites, not the spherulites

themselves. With increasing BTO content, more nucleation sites were present. In this case, the crystals influenced each other and the growth of large ring banded spherulites was impeded. Correspondingly, the Avrami exponent *n* for composites with large BTO content was in the range of 3 to 4. Figure 7.5 schematically illustrates the different microstructures due to varying BTO content.

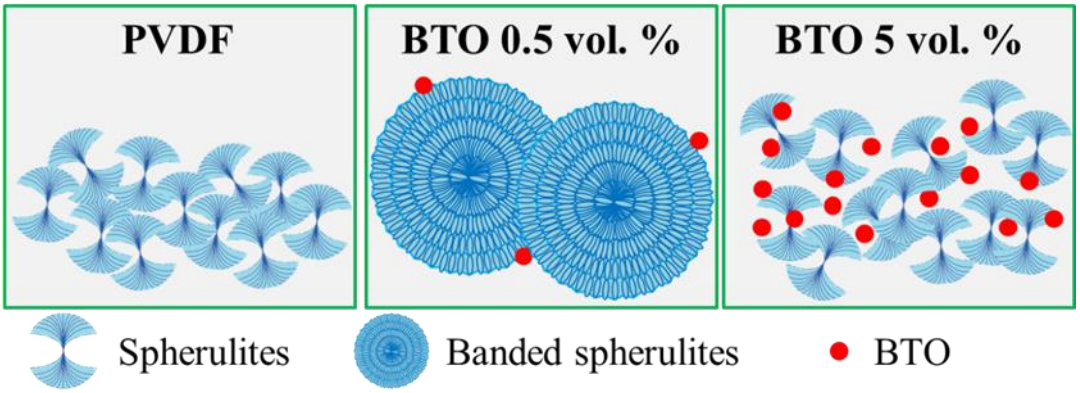

Figure 7.5 Schematic diagrams for spherulites crystallized at 150 °C.

On the basis of the $t_{1/2}$ values listed in Table 7.1, the crystallization rate of PVDF was influenced by the addition of BTO particles. Despite the nucleating effect, the $t_{1/2}$ values of composites filled with 0.15 and 0.5 vol. % BTO particles were similar to that of pure PVDF, arising from the longer time needed to the form large ring banded spherulites. With further increasing BTO content, the $t_{1/2}$ values became smaller, indicating that the addition of large amounts of BTO particles facilitated the crystallization of PVDF because there were more nucleation sites.

An important link exists between the isothermal crystallization studies and the morphology and thermal behaviours of the as-extruded films. Composites filled with less than 1 vol. % BTO particles crystallized into large ring banded spherulites (diameter ~ 50 μm) during isothermal crystallization, correspondingly, the as-extruded

composites filled with the same BTO content crystallized into large spherulites (diameter ~ 10 μm), almost tripling the size of the spherulites crystallized in the pure PVDF (diameter ~ 3 μm).

7.3.2 Effect of BTO particles on solid state drawing of PVDF films

Ferroelectric β-phase PVDF is widely used in applications that require electro-active properties. The common method to obtain the β-phase is solid state drawing of α-phase PVDF with draw ratios ranging from 3 to 5. It is conceivable that the addition of BTO particles would influence the behaviour of the PVDF matrix during solid state drawing, leading to differences in the functional properties

Figure 7.6 shows the stress-strain curves recorded during drawing of the as-extruded films, at 100 °C and 120 °C. The stretching temperatures were chosen according to the crystalline relaxation temperature of PVDF. [150]The samples showed similar values of strain at failure, ranging from 3 to 4.2, which should be sufficient to transform α- to β-phase.[160] Figure 7.7 shows the morphology of drawn films, which display fibrilar structure and no obvious difference exists between the 100 °C and 120 °C drawn films.

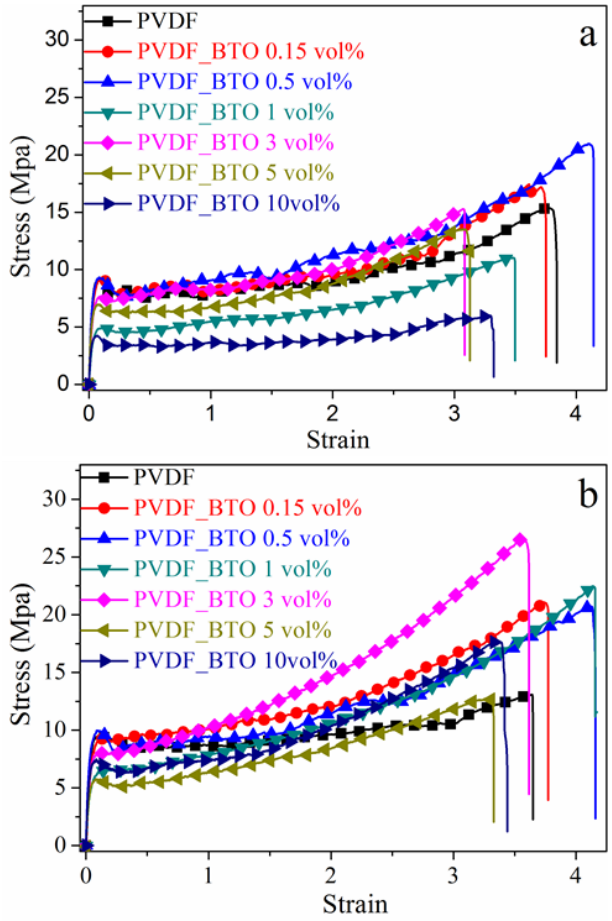

Figure 7.6 Stress-strain curves for PVDF and PVDF_BTO composites films drawn at: (a) 100 °C; (b) 120 °C. The drawing rates for both are 10 mm/min.

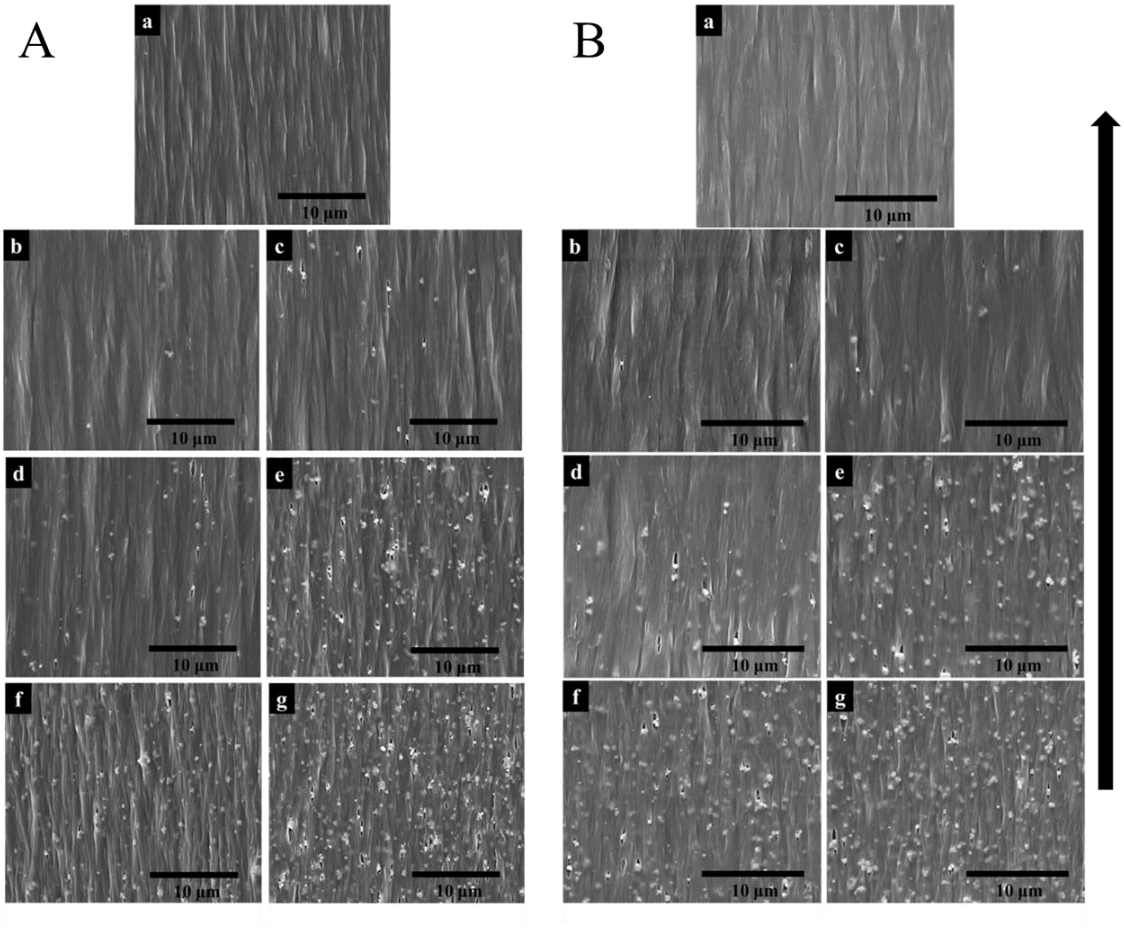

Figure 7.7 SEM images of films drawn to breaking point at 10 mm/min and (A) 100 °C and (B) 120 °C: (a) pure PVDF; (b) PVDF_BTO 0.15 vol. %; (c) PVDF_BTO 0.5 vol. %; (d) PVDF_BTO 1 vol. %; (e) PVDF_BTO 3 vol. %; (f) PVDF_BTO 5 vol. %; (g) PVDF_BTO 10 vol. %. The arrow indicates the drawing direction.

Figure 7.8 shows the XRD data for the drawn films. Reflections from the β-phase at 20.7° (110)/$(200)_\beta$ are clearly present (Figure 7.8a). For the films drawn at 100 °C, the emergence of the peak at 20.7° occurred with the disappearance of the $(100)_\alpha$ peak and a reduction in the intensity of the $(110)_\alpha$ peaks. The films drawn at 120 °C clearly show combined reflections from the α- and β-phases. None of the drawn films exhibited full transformation into the β-phase, but the lower drawing temperature (100 °C) favoured this transformation, which is consistent with other reported works.[145, 149, 150] A higher

drawing temperature is associated with higher chain mobility, especially in the amorphous region, which allows chains to relax, preventing efficient phase transformation.

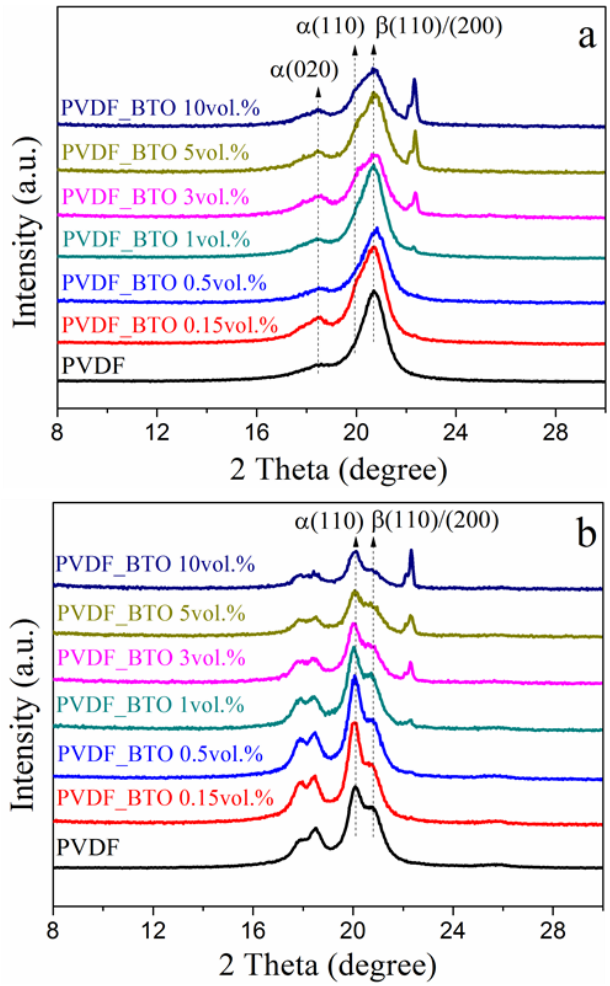

Figure 7.8 1D-WAXD patterns for films drawn to breaking point at 10 mm/min: (a) 100 °C; (b) 120 °C.

The phase transformation of PVDF is induced by the uniaxial tensile deformation leading to an orientation of the polymer chains along the drawing direction. The 2D-WAXD patterns for the films drawn at 100 °C and 120 °C are shown in Figure 7.9 and 7.10, respectively. Referenced to the 1D-XRD data, the arcs displayed in Figure 7.9 are attributed to the $(020)_{\alpha}$ and $(110)/(200)_{\beta}$ reflections in the 100 °C drawn PVDF films.

The equatorially concentrated (hk0) arcs indicate that the c-axis (polymer chain direction) is aligned along the drawing direction. Similarly, all of the composite samples exhibited diffraction arcs of $(020)_\alpha$ and $(110)/(200)_\beta$. The full rings from the reflections of the BTO particles are progressively more obvious with increasing filler content. The degree of polymer chain orientation was evaluated using the Herman's factor (f) using Equation 7.5, where φ is the angle between polymer chain axis and the reference direction (the drawing direction). For ideal orientation, φ=0 and f=1, on the contrary, $\langle\cos^2\varphi\rangle$=1/3 and f=0 describes a random orientation.

$$f = (3\langle\cos^2\varphi\rangle - 1)/2 \qquad 7.5$$

The calculated f values for PVDF and the composite samples are listed at the bottom of each 2D-WAXD pattern. The addition of BTO particles hardly influences the crystalline preferred orientation when drawing at 100 °C.

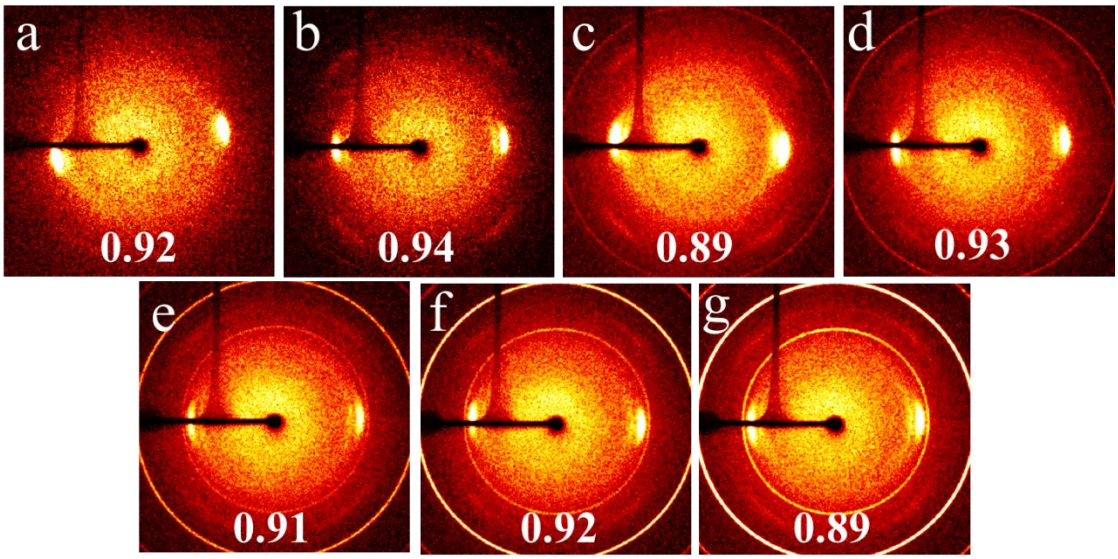

Figure 7.9 2D-WAXD ring patterns for films drawn to breaking point at 100 °C and 10 mm/min: (a) pure PVDF; (b) PVDF_BTO 0.15 vol. %; (c) PVDF_BTO 0.5 vol. %; (d) PVDF_BTO 1 vol. %; (e) PVDF_BTO 3 vol. %; (f) PVDF_BTO 5 vol. %; (g) PVDF_BTO 10 vol. %. The stretching direction is vertical with X-ray beam perpendicular to the film plane.

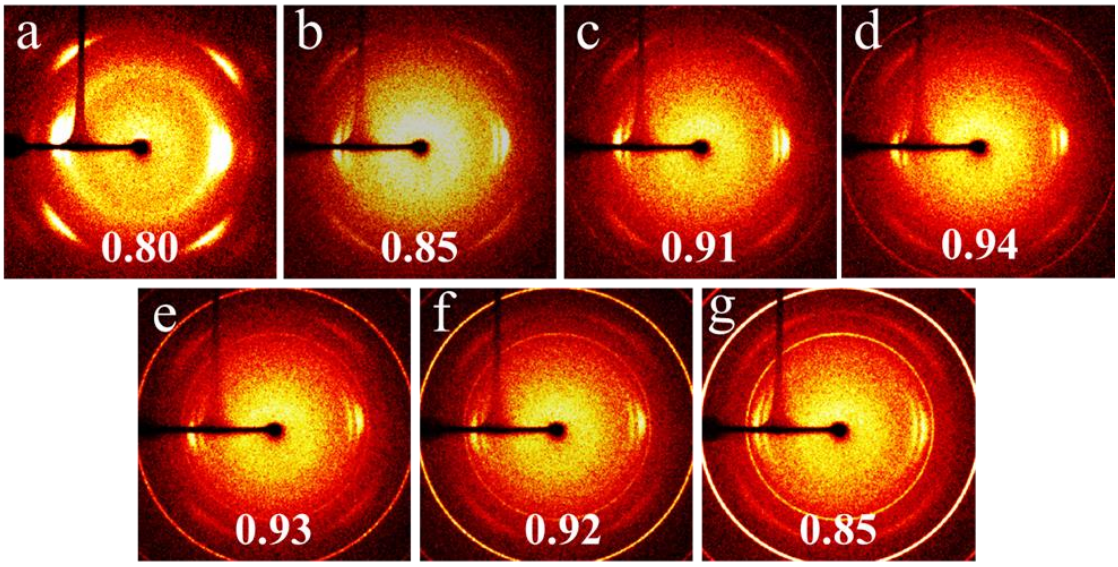

Figure 7.10 2D-WAXD ring patterns for films drawn to breaking point at 120 °C and 10 mm/min: (a) pure PVDF; (b) PVDF_BTO 0.15 vol. %; (c) PVDF_BTO 0.5 vol. %; (d) PVDF_BTO 1 vol. %; (e) PVDF_BTO 3 vol. %; (f) PVDF_BTO 5 vol. %; (g) PVDF_BTO 10 vol. %. The stretching direction is vertical with X-ray beam perpendicular to the film plane.

Apart from the $(020)_\alpha$ and $(110)/(200)_\beta$ reflections, the 120 °C drawn PVDF showed four arcs at about 45° off the equator (Figure 7.10a), which are reflections from the $(021)_\alpha$ crystal planes. The increased chain mobility with increased temperature leads to a smaller effect of drawing on chain conformation, only orienting the crystals but not changing the chain conformation from trans-gauche to all-trans, thereby merely forming oriented α-crystals. The intensity of the $(021)_\alpha$ reflection became weaker with increasing BTO amount, which is due to the reduced α-PVDF content in the composites. Contrary to the condition of drawing at 100 °C, the degree of orientation was enhanced by the presence of BTO particles. The *f* value peaked at 0.94 for the composite filled with 1 vol. % BTO.

Figure 7.11a shows the DSC heating scans for the drawn films. The values of the calculated crystallinity and melting temperature are listed in Table 7.2. The crystallinity values represent total crystallinity of the α- and β-phases combined. Compared to the DSC graphs for the as-extruded samples, the drawn films exhibited only one fusion peak, which was about 3 °C lower than that of the main fusion peak for the as-extruded films (Figure 7.3a and Table 7.1). This is probably ascribed to the different crystalline phases; however, according to the literature the values of the melting temperature for α- and β-PVDF are possibly not differentiated. Martins et al. [97] suggested that α- and β-PVDF showed indistinguishable melting temperatures in the range of 167-172 ℃, while other researchers[88, 98, 99] have suggested that the β-PVDF should have a higher melting temperature than the α-phase due to its more densely packed all-trans chain conformation. Lanceros-Méndez group[100] reported the melting temperature of poled β-PVDF films as 156.3 ℃, much lower than the commonly reported values for α-PVDF. The conclusion from our work is that the melting temperature of β-phase is slightly lower than that of α-phase. The films drawn at 100 °C showed similar crystallinity to those of the as-extruded films, while the crystallinity of the films drawn at 120 °C increased moderately, which is linked to their more obvious strain hardening behaviour (Figure 7.6 and Table 7.2). Another feature shown in Figure 7.11a is the highly asymmetric shape of the fusion peaks for the 100 °C drawn films, owing to the heterogeneous distribution of crystallite size formed during drawing at the lower temperature,[150] which suggests strong interactions between the PVDF and BTO fillers.

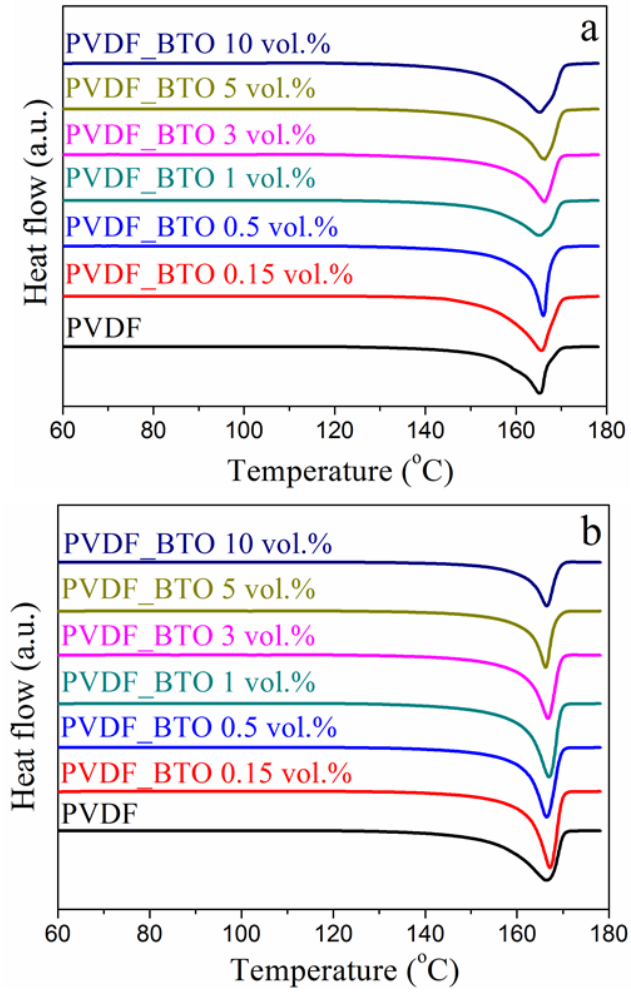

Figure 7.11 DSC heating scans for PVDF and PVDF_BTO composites films drawn to breaking point at: (a) 100 °C; (b) 120 °C.

Figure 7.12 shows the FTIR spectra for the drawn films. The fraction of β-phase (*F(β)*) is listed in Table 7.2. It can be seen that the films drawn at 100 °C exhibit more β-phase, which is consistent with their XRD data, and *F(β)* was nearly independent of BTO content. For films drawn at 120 °C, the formation of the β-phase was enhanced in the presence of the BTO particles. The increase was more prominent at low loadings (<5 vol. % BTO).

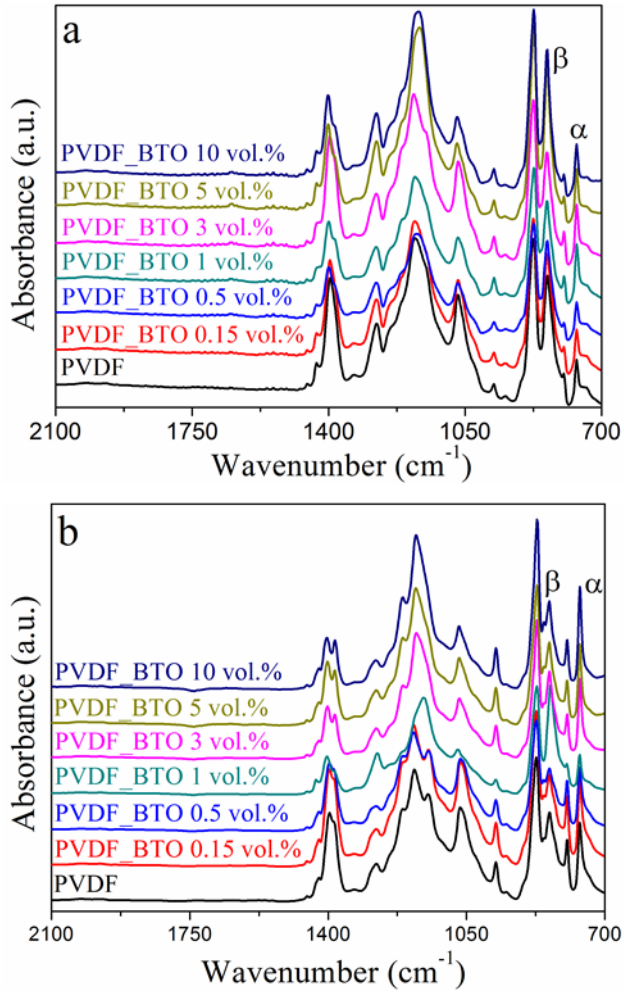

Figure 7.12 FTIR spectra for PVDF and PVDF_BTO composite films drawn to breaking point at: (a) 100 °C; (b) 120 °C.

Table 7.2 Crystallinity X_c, melting temperature T_m and fraction of β-phase *F(β)* for samples drawn to breaking point at 100 °C and 120 °C, the drawing rate is constant 10 mm/min. The enthalpy of fusion for a fully crystalline PVDF is 104.6 J/g.[186]

Samples	**Drawn at 100 °C**			**Drawn at 120 °C**		
	X_c	T_m	***F(β)* wt. %**	X_c	T_m	***F(β)* wt. %**
PVDF	50.3±2%	165.5±2	86.0±4	50.7±2%	166.5±2	47.3±3
PVDF_BTO 0.15 vol. %	53.5±4%	165.7±1	88.3±5	51.6±2%	167.4±1	51.4±2
PVDF_BTO 0.5 vol. %	49.4±4%	166.1±2	87.2±4	52.5±2%	166.5±2	53.9±3
PVDF_BTO 1 vol. %	48.8±3%	165.2±2	86.2±4	54.0±1%	166.9±1	59.9±4
PVDF_BTO 3 vol. %	48.9±1%	166.3±1	83.2±5	54.8±1%	166.7±2	56.1±3
PVDF_BTO 5 vol. %	49.2±4%	166.1±1	84.7±3	51.0±3%	166.1±2	51.0±3
PVDF_BTO 10 vol. %	49.4±5%	165.2±2	85.1±5	51.1±3%	166.5±1	45.2±3

7.3.3 Electric properties of PVDF_BTO composites

Dielectric properties

The dielectric frequency spectra for the pure PVDF and PVDF_BTO composites are shown in Figure 7.13a-c. In the low frequency range (100-10000 Hz) the dielectric loss

tangent (*D*) of the as-extruded films decreased with increasing frequency, which is ascribed to the crystalline relaxation of α-PVDF.[15]

Figure 7.13d shows the relationship between the BTO content and the values of dielectric constant *ε'* and dielectric loss *D* measured at 1000 Hz and room temperature. It can be seen that the 100 °C drawn pure PVDF and composites with low BTO content (0.15 and 0.5 vol. %) displayed larger dielectric constant (*ε'*) compared to the as-extruded films and the 120 °C drawn films with the same BTO content, which is due to the formation of the more polar β-phase structure, consistent with the reported work by Guan *et al.* [197] Composites filled with large amounts of BTO particles (5 and 10 vol. %), however, exhibited smaller *ε'* values in the drawn samples in comparison with the as-extruded samples, which is associated with the fact that drawing reduces agglomeration of the particles and improves the distribution of high ratios of fillers. Meanwhile, the *D* did not increase obviously due to the addition of BTO particles, which proves the fact that the introduction of BTO particles did not result in severe defects, and is also consistent with the DSC data, which showed that the composites and pure PVDF samples showed similar crystallinity values. The as-extruded samples showed higher dielectric loss than the drawn samples especially for the composites.

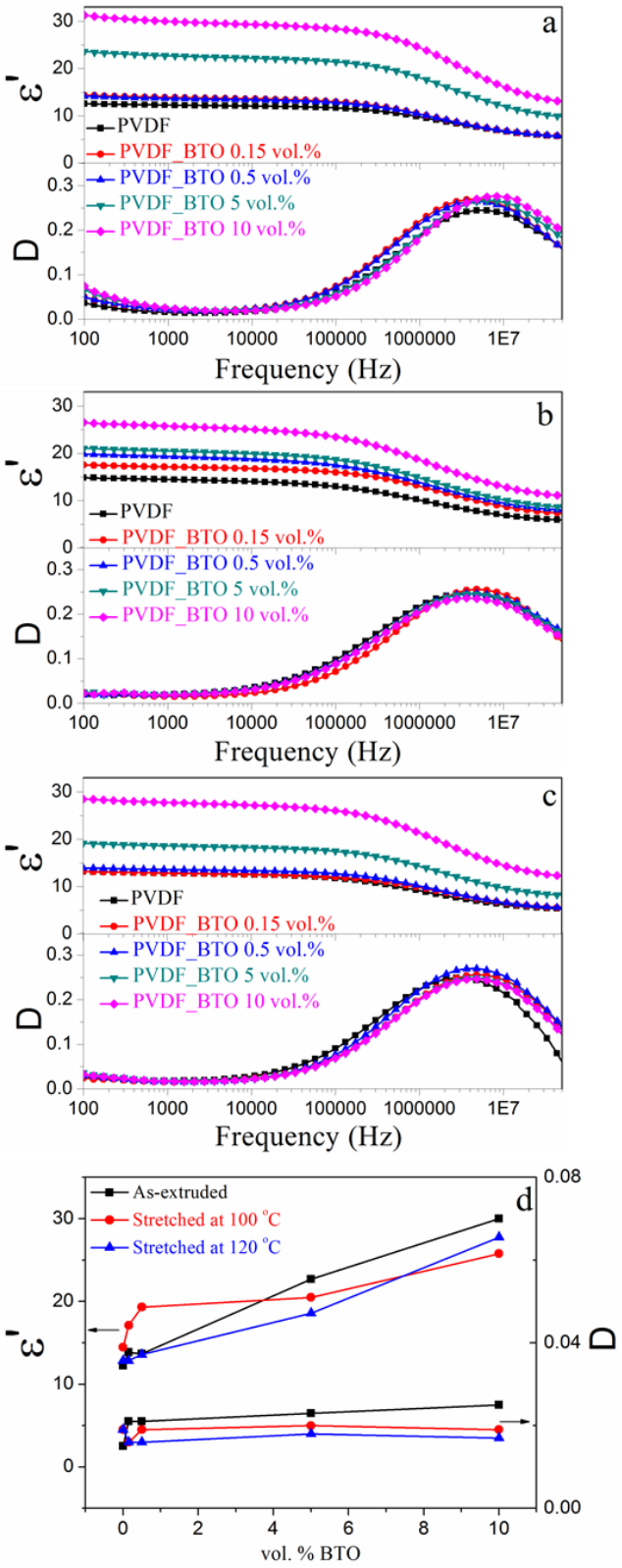

Figure 7.13 Frequency dependence of pure PVDF and PVDF _BTO composites with BTO content of 0.15, 0.5, 5, 10 vol. %: (a) as-extruded films; (b) films drawn to breaking point at

100 °C and 10 mm/min; (c) films drawn to breaking point at 120 °C and 10 mm/min. (d) dielectric permittivity (ε') and loss (D) as a function of vol. % BTO.

Ferroelectric properties

The ferroelectric properties of the pure PVDF and PVDF_BTO composites are shown in Figure 7.14. The displayed P-E loops are all saturated, which was determined by checking the invariance of the position of switching current peak with increasing maximum amplitude. The as-extruded samples displayed ferroelectric switching, which was associated with a field induced phase transformation during testing, from the non-polar α-phase to the polar δ-phase. The remnant polarization and coercive field for the pure as-extruded PVDF were 0.05 C/m^2 and 115 kV/mm (Figure 7.14a, b), respectively, consistent with the reported values for δ-PVDF.[40] Small amounts of BTO, 0.15 and 0.5 vol. %, slightly increased the remnant polarization. However, larger BTO contents, e.g. 10 vol. %, resulted in severe current leakage and decreased the breakdown voltage, which is mainly ascribed to particle aggregation and/or formation of voids at high filler contents.

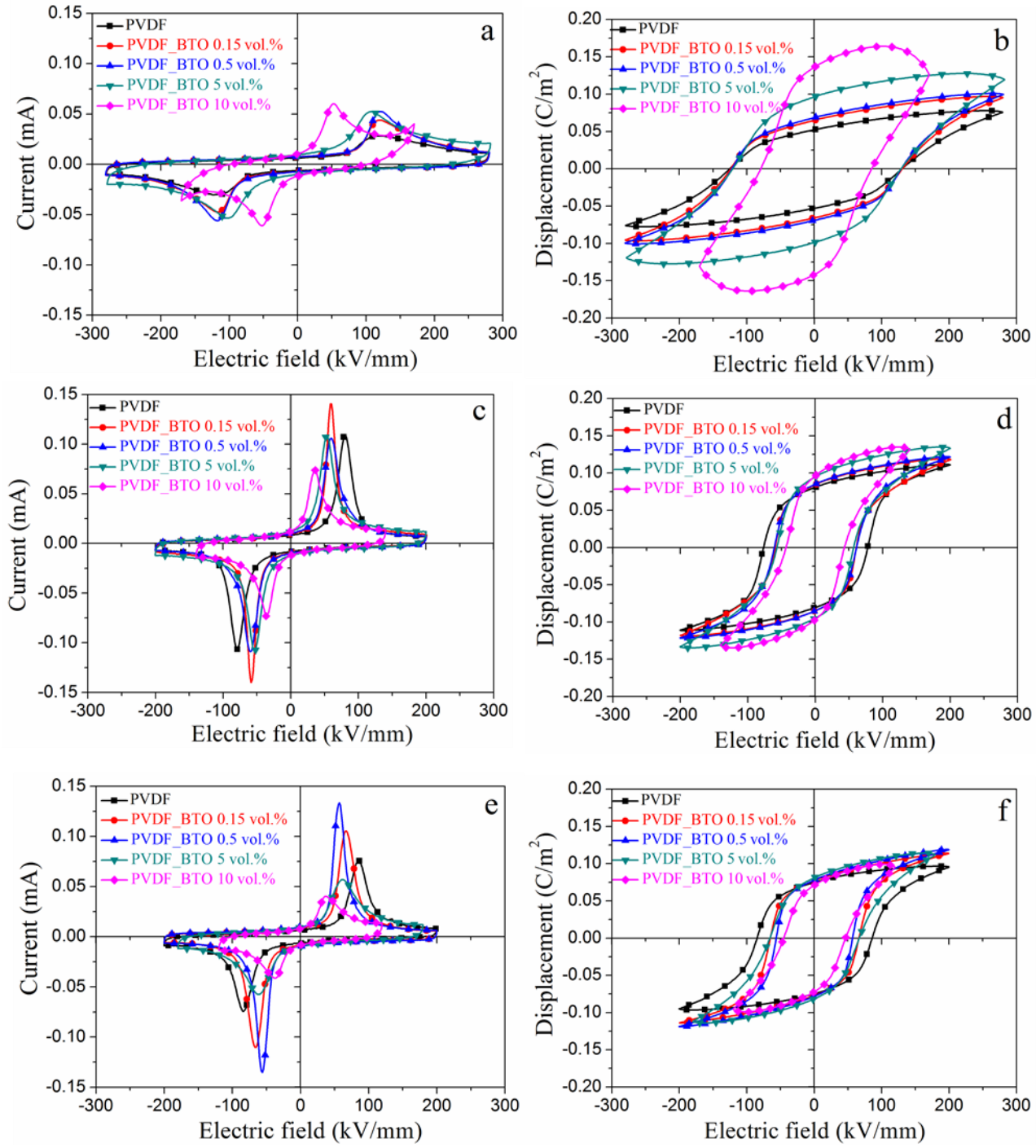

Figure 7.14 Ferroelectric I-E and P-E loops measured at 10 Hz for pure PVDF and PVDF _BTO composites with BTO content of 0.15, 0.5, 5, and 10 vol. %: (a, b) as-extruded films; (c, d) films drawn to breaking point at 100 °C and 10 mm/min; (e, f) films drawn to breaking point at 120 °C and 10 mm/min.

The drawn films (Figure 7.14c-f) produced well defined ferroelectric behaviour. The 100 °C drawn pure PVDF showed a remnant polarization of 0.080 C/m^2 and a coercive field of 80 kV/mm. Comparable values were observed in the 120 °C drawn PVDF, 0.075 C/m^2 and 86 kV/mm, respectively. The slightly lower remnant polarization in the 120 °C drawn PVDF films is linked to the lower content of the ferroelectric β-phase. It is clearly seen that the coercive field of the composites decreased to about 60 kV/mm, a 25 % reduction compared to that of pure PVDF in both the 100 °C and 120 °C drawn films. The interfaces between the PVDF matrix and BTO particles may have facilitated the nucleation of ferroelectric domains, which assists ferroelectric switching.[181] For the 100 °C drawn films, the remnant polarization of the composites filled with 5 vol. % BTO reached 0.095 C/m^2 without showing any current leakage. To the best of our knowledge, the highest reported values of ferroelectric remnant polarization of PVDF based polymer composites is 0.093 C/m^2 for PVDF-TrFE filled with 10.8 vol. % BTO nanofibers.[124]

7.4 Conclusions

In conclusion, the PVDF_BTO composites prepared by extrusion followed by solid state drawing were systematically studied. The BTO particles do not promote the crystallization of β-phase in PVDF, but larger α-PVDF spherulites were formed with the addition of less than 3 vol. % of BTO particles. A study of isothermal crystallization revealed that small amounts of BTO produce a significant change in the crystallization behaviour of PVDF; the Avrami exponent *n* changed from 4 to 2 with the addition of small amounts of BTO (less than 1 vol. %), which indicates that the crystals of PVDF were changed from three-dimensional spherulites to two-dimensional lamellar structure

due to the nucleation effect of BTO on the crystallization of large full ring banded spherulites. Additionally, in the following process of transforming α- to β-PVDF via solid state drawing, the rigid BTO particles produced stress concentrating effects along with the formation of voids and cavities, facilitating the generation of β-PVDF with more pronounced crystalline orientation in the case of the higher drawing temperature (120 °C). Finally, the dielectric properties were improved with the addition of BTO, the dielectric permittivity of 100 °C drawn films roughly increased from 14 to 20 (100 Hz), while the dielectric loss remained at about 0.02 after filling with 5 vol. % of BTO particles. The ferroelectric properties were also enhanced by drawing; the 100 °C drawn PVDF_BTO 5 vol. % composites films showed a remnant polarization of 0.095 C/m^2 the highest value ever reported for PVDF based composite materials and a coercive field of 50 kV/mm without the occurrence of obvious current leakage.

Chapter 8 Conclusions and Future Work

8.1 Conclusions

This thesis has examined the melt-extrusion processing, structure and properties of PVDF, PVDF-TrFE, PVDF/PVDF-TrFE blends and PVDF_BTO composite materials.

8.1.1 PVDF

In Chapter 4:

- Melt extruded PVDF films mainly crystallized into non-ferroelectric α-phase regardless of the processing conditions. The ferroelectric β-phase PVDF was obtained by high temperature drawing of the α-phase of as-extruded films. Both the α- and β-phase coexisted in the drawn films.
- The fraction of β-phase was influenced by the draw ratio, drawing temperature and drawing rate. A minimum draw ratio of 3 was required to form β-phase. High drawing temperature (> 100 °C) could only orientate the α-crystals along the drawing direction, but did not make the chain conformation change to form the β-phase. At the same draw ratio and drawing rate (draw ration 3, drawing rate 10 mm/min), films drawn at 120 °C contained only 50% β-phase, lower than that of films drawn at 80 °C and 100 °C (~ 80%). Films drawn at 100 °C and 5 mm/min contained only 65% β-phase, which increased to 80% with increasing drawing rate to 10 mm/min, but any further increase in the drawing rate made no difference on the content of β-phase.

- Uniaxial drawing changed the spherulites to fibril structure and caused the polymer chains to orientate along the drawing direction, resulting in preferred crystalline orientation. The overall crystallinity calculated using the values of enthalpy of fusion did not alter after drawing. However, the melting temperatures of the drawn films were lower than that of as-extruded films, as determined from both the DSC data and dielectric temperature spectra. Moreover, the dielectric temperature spectra also indicated higher glass transition temperature for the drawn films.
- The dielectric constant values of the drawn films were higher compared to the as-extruded films because of their higher β-phase content.
- The drawn films showed significantly higher ferroelectric remnant polarization and less current leakage as compared to the as-extruded films. It is believed that the improvement in the ferroelectric properties is mainly ascribed to their higher β-phase content and preferred orientation.

8.1.2 PVDF-TrFE

In Chapter 5:

- Highly crystalline and oriented PVDF-TrFE films can be produced by melt extrusion, with the polymer chain axis along extrusion direction. The crystalline structure and orientation level can be controlled by changing the extrusion temperature.
- The optimum extrusion temperature was found to be 190 ℃. The 190 ℃ extruded PVDF-TrFE films exhibited a well stacked edge-on lamella structure with remarkable ferroelectric properties.

- The coercive field was 23.9 kV/mm and the remnant polarization (0.078 C/m^2) was close to the estimated remnant polarization value assuming perfect in-plane c-axis orientation and 80% crystallinity (0.082 C/m^2). After annealing at 140 ℃ the crystallinity of the films was increased (~ 90%) and the ferroelectric properties further improved with P_r of 0.099 C/m^2 and E_c of 37.9 kV/mm.

8.1.3 PVDF/PVDF-TrFE blends

In Chapter 6:

- PVDF and PVDF-TrFE are immiscible according to the DSC results, but they intimately crystallize on a fine scale (~ 40 nm) without the appearance of distinct phase separation.
- With increasing amount of PVDF-TrFE, the blended films have more β-phase and increased preferred orientation, more than would be expected based on a simple rule of mixtures.
- Due to interfacial polarization, PVDF/PVDF-TrFE blended films have larger dielectric constant than those of the two pure components.
- The ferroelectric properties of the blended films were enhanced by the introduction of PVDF-TrFE. The switching field decreased (from 75 to 32 kV/mm), while the remnant polarization increased (from 0.040 to 0.077 C/m^2) with increasing amount of PVDF-TrFE from 0 to 40 wt. %.
- The Curie transition was suppressed in the blended films, which may lead to increased high temperature stability for piezoelectric applications.

8.1.4 PVDF_BTO composite films

In Chapter 7:

- The BTO particles do not promote the crystallization of β-phase in PVDF, but larger α-PVDF spherulites were formed with the addition of less than 3 vol. % of BTO particles.

- A study of isothermal crystallization revealed that small amounts of BTO produce a significant change in the crystallization behaviour of PVDF; the Avrami exponent *n* changed from 4 to 2 with the addition of small amounts of BTO (less than 1 vol. %), which indicates that the crystals of PVDF were changed from three-dimensional spherulites to two-dimensional lamellar structure due to the nucleation effect of BTO on the crystallization of large full ring banded spherulites.

- In the following process of transforming α- to β-PVDF via solid state drawing, the rigid BTO particles produced stress concentrating effects along with the formation of voids and cavities, facilitating the generation of β-PVDF with more pronounced crystalline orientation in the case of the higher drawing temperature (120 °C).

- The dielectric properties were improved with the addition of BTO, the dielectric permittivity of 100 °C drawn films roughly increased from 14 to 20 (100 Hz), while the dielectric loss remained at about 0.02 after filling with 5 vol. % of BTO particles.

- The ferroelectric properties were also enhanced by drawing; the 100 °C drawn PVDF_BTO 5 vol. % composites films showed a remnant polarization of 0.095 C/m^2 the highest value ever reported for PVDF based composite materials and a coercive field of 50 kV/mm without the occurrence of obvious current leakage.

8.2 Future work

8.2.1 Ferroelectric switching mechanism of polymers

There is an obvious lack of literature about the structure of ferroelectric domains in polymers and how they respond during ferroelectric switching. The in-situ temperature measurement of piezoresponse force microscopy (PFM) should be conducted to study the ferroelectric switching for polymers.

8.2.2 Revisiting the phase diagram of PVDF-TrFE

According to the existing phase diagram, PVDF-TrFE with TrFE content less than 55% should be antiferroelectric. However, the PE-loops of PVDF-TrFE 51/49 showed typical ferroelectric behaviour. The phase diagram of PVDF-TrFE should be revisited not only in the temperature dependence, but also in the electric field dependence.

8.2.3 Minimizing crystallite size for PVDF-based polymer films

PVDF-TrFE 77/23 shows a first order Curie transition with large hysteresis. However, the Curie transition of extruded PVDF/PVDF-TrFE blends was suppressed, which is significantly related to the small crystallite size. This gives us some thoughts on decreasing the crystallite size of PVDF-based polymers into several nanometers, which could help us to obtain high energy density and low loss dielectric polymer materials.

List of Publications

1. N. Meng, R. Mao, W. Tu, X. Zhu, R. M. Wilson, E. Bilotti, M. J. Reece, Processing and Characterization of Free Standing Highly Oriented Ferroelectric Polymer Films with Remarkably Low Coercive Field and High Remnant Polarization, *Polymer*, 2016, **100**, 69-76.
2. N. Meng, X. Zhu, R. Mao, M. J. Reece and E. Bilotti, Nanoscale Interfacial Electroactivity in PVDF/PVDF-TrFE Blended Films with Enhanced Dielectric and Ferroelectric Properties, *J. Mat. Chem. C*, 2017, **5**, 3296-3305.
3. N. Meng, W. Tu, Q. Zhang, E. Bilotti, M. J. Reece, Crystallization Kinetics and Enhanced Dielectric Properties of Free Standing PVDF/$BaTiO_3$ Composite Films, *Polymer*, DOI: 10.1016/j.polymer.2017.06.009.

Reference

1. L. B. Kong, T. S. Zhang, J. Ma and F. Boey, *Prog Mater Sci*, 2008, **53**, 207-322.
2. G. H. Haertling, *J Am Ceram Soc*, 1999, **82**, 797-818.
3. D. Damjanovic, *Reports on Progress in Physics*, 1998, **61**, 1267-1324.
4. J. Valasek, *Physical Review*, 1921, **17**, 475-481.
5. Y. Saito, H. Takao, T. Tani, T. Nonoyama, K. Takatori, T. Homma, T. Nagaya and M. Nakamura, *Nature*, 2004, **432**, 84-87.
6. D. Damjanovic, P. Muralt and N. Setter, *Ieee Sensors Journal*, 2001, **1**, 191-206.
7. R. B. Meyer, Liebert, L. ,Strzelecki, L. , Keller, P. , *Journal de Physique Lettres*, 1975, **36**, 3.
8. M. Tamura, S. Hagiwara, S. Matsumoto and N. Ono, *J Appl Phys*, 1977, **48**, 513-521.
9. R. G. Kepler, *Annual Review of Physical Chemistry*, 1978, **29**, 497-518.
10. R. Hasegawa, Kobayashi, M., Tadokoro, H., *Polymer Journal* 1972, **3**, 591-599.
11. T. Furukawa, T. Nakajima and Y. Takahashi, *Ieee T Dielect El In*, 2006, **13**, 1120-1131.
12. G. T. Davis, J. E. McKinney, M. G. Broadhurst and S. C. Roth, *J Appl Phys*, 1978, **49**, 4998-5002.
13. A. J. Lovinger, *Science*, 1983, **220**, 1115-1121.
14. S. L. Weinhold, M. H. ; and Lando, J. B. , *Macromolecules*, 1980, **13**, 1178-1183.
15. T. Furukawa, *Phase Transit*, 1989, **18**, 143-211.
16. J. B. D. Lando, W. W, *Journal of Macromolecular Science, Part B: Physics*, 1968, **B2**, 205-218.
17. T. Yagi, M. Tatemoto and J.-i. Sako, *Polym J*, 1980, **12**, 209-223.
18. T. Furukawa, M. Ohuchi, A. Chiba and M. Date, *Macromolecules*, 1984, **17**, 1384-1390.
19. T. Furukawa and G. E. Johnson, *J Appl Phys*, 1981, **52**, 940-943.
20. G. T. Davis, T. Furukawa, A. J. Lovinger and M. G. Broadhurst, *Macromolecules*, 1982, **15**, 329-333.

21. T. Furukawa, *Advances in Colloid and Interface Science*, 1997, **71–72**, 183-208.
22. K. Tashiro, K. Takano, M. Kobayashi, Y. Chatani and H. Tadokoro, *Polymer*, 1984, **25**, 195-208.
23. F. Ishii, A. Odajima and H. Ohigashi, *Polym J*, 1983, **15**, 875-882.
24. K. Tashiro, H. Tadokoro and M. Kobayashi, *Ferroelectrics*, 1981, **32**, 167-175.
25. R. G. Kepler and R. A. Anderson, *Advances in Physics*, 1992, **41**, 1-57.
26. E. Bellet-Amalric and J. F. Legrand, *Eur. Phys. J. B*, 1998, **3**, 225-236.
27. O. Hiroji, A. Shuyo and K. Keiko, *Japanese Journal of Applied Physics*, 1988, **27**, 2144.
28. G. T. Davis, M. G. Broadhurst, A. J. Lovinger and T. Furukawa, *Ferroelectrics*, 1984, **57**, 73-84.
29. F. Takeo, N. Kenji, K. Tomoyoshi and D. Munehiro, *Japanese Journal of Applied Physics*, 1987, **26**, 1039.
30. Z. Li, J. Wang, X. Wang, Q. Yang and Z. Zhang, *RSC Advances*, 2015, **5**, 80950-80955.
31. R. I. Mahdi, W. C. Gan and W. H. Abd Majid, *Sensors (Basel, Switzerland)*, 2014, **14**, 19115-19127.
32. N. Tsutsumi, T. Kitano, K. Kinashi and W. Sakai, *Materials*, 2014, **7**, 6367.
33. V. M. Fridkin and S. Ducharme, *Phys. Solid State*, 2001, **43**, 1320-1324.
34. S. Ducharme, V. M. Fridkin, A. V. Bune, S. P. Palto, L. M. Blinov, N. N. Petukhova and S. G. Yudin, *Physical Review Letters*, 2000, **84**, 175-178.
35. H. G. Kassa, R. Cai, A. Marrani, B. Nysten, Z. Hu and A. M. Jonas, *Macromolecules*, 2013, **46**, 8569-8579.
36. Z. J. Hu, M. W. Tian, B. Nysten and A. M. Jonas, *Nat Mater*, 2009, **8**, 62-67.
37. Y. Wu, Q. Gu, G. Ding, F. Tong, Z. Hu and A. M. Jonas, *ACS Macro Letters*, 2013, **2**, 535-538.
38. V. Bhavanasi, D. Y. Kusuma and P. S. Lee, *Advanced Energy Materials*, 2014, **4**, n/a-n/a.
39. S. Tasaka and S. Miyata, *J Appl Phys*, 1985, **57**, 906-910.
40. M. Li, H. J. Wondergem, M.-J. Spijkman, K. Asadi, I. Katsouras, P. W. M. Blom and D. M. de Leeuw, *Nat Mater*, 2013, **12**, 433-438.
41. Q. M. Zhang, V. Bharti and X. Zhao, *Science*, 1998, **280**, 2101-2104.

42. T. Furukawa, A. J. Lovinger, G. T. Davis and M. G. Broadhurst, *Macromolecules*, 1983, **16**, 1885-1890.
43. C. Huang, R. Klein, F. Xia, H. Li, Q. M. Zhang, F. Bauer and Z. Y. Cheng, *Dielectrics and Electrical Insulation, IEEE Transactions on*, 2004, **11**, 299-311.
44. H. Ohigashi, K. Omote and T. Gomyo, *Appl Phys Lett*, 1995, **66**, 3281-3283.
45. O. Hiroji and K. Keiko, *Japanese Journal of Applied Physics*, 1982, **21**, L455.
46. K. Kuniko and O. Hiroji, *Japanese Journal of Applied Physics*, 1986, **25**, 383.
47. Q. M. Zhang, H. Xu, F. Fang, Z.-Y. Cheng, F. Xia and H. You, *J Appl Phys*, 2001, **89**, 2613-2616.
48. R. C. G. Naber, P. W. M. Blom, A. W. Marsman and D. M. de Leeuw, *Appl Phys Lett*, 2004, **85**, 2032-2034.
49. D. Mao, M. A. Quevedo-Lopez, H. Stiegler, B. E. Gnade and H. N. Alshareef, *Organic Electronics*, 2010, **11**, 925-932.
50. X. B. Liu, A. Q. Jiang and T. A. Tang, *Integrated Ferroelectrics*, 2012, **133**, 81-87.
51. H. Kliem and R. Tadros-Morgane, *Journal of Physics D: Applied Physics*, 2005, **38**, 1860.
52. D. Guo and N. Setter, *Macromolecules*, 2013, **46**, 1883-1889.
53. L. M. Blinov, V. M. Fridkin, S. P. Palto, A. V. Sorokin and S. G. Yudin, *Thin Solid Films*, 1996, **284–285**, 474-476.
54. H. Zhu, S. Yamamoto, J. Matsui, T. Miyashita and M. Mitsuishi, *Journal of Materials Chemistry C*, 2014, **2**, 6727-6731.
55. J. L. Wang, B. L. Liu, X. L. Zhao, B. B. Tian, Y. H. Zou, S. Sun, H. Shen, J. L. Sun, X. J. Meng and J. H. Chu, *Appl Phys Lett*, 2014, **104**, 182907.
56. B. B. Tian, L. F. Chen, Y. Liu, X. F. Bai, J. L. Wang, S. Sun, G. L. Yuan, J. L. Sun, B. Dkhil, X. J. Meng and J. H. Chu, *Physical Review B*, 2015, **92**, 060102.
57. J. H. Park, N. Kurra, M. N. AlMadhoun, I. N. Odeh and H. N. Alshareef, *Journal of Materials Chemistry C*, 2015, **3**, 2366-2370.
58. M. Li, I. Katsouras, K. Asadi, P. W. M. Blom and D. M. de Leeuw, *Appl Phys Lett*, 2013, **103**, 072903.
59. S. Yano, *Journal of Polymer Science Part A-2: Polymer Physics*, 1970, **8**, 1057-1072.

60. E. Tuncer, M. Wegener and R. Gerhard-Multhaupt, *Journal of Non-Crystalline Solids*, 2005, **351**, 2917-2921.
61. R. Singh, J. Kumar, R. K. Singh, A. Kaur, R. D. P. Sinha and N. P. Gupta, *Polymer*, 2006, **47**, 5919-5928.
62. V. Sencadas, S. Lanceros-Méndez, R. Sabater i Serra, A. Andrio Balado and J. L. Gómez Ribelles, *Eur. Phys. J. E*, 2012, **35**, 1-11.
63. G. A. Samara, *Journal of Polymer Science Part B: Polymer Physics*, 1989, **27**, 39-51.
64. Y. Miyamoto, H. Miyaji and K. Asai, *Journal of Polymer Science: Polymer Physics Edition*, 1980, **18**, 597-606.
65. L. Yang, J. Ho, E. Allahyarov, R. Mu and L. Zhu, *ACS Applied Materials & Interfaces*, 2015, **7**, 19894-19905.
66. N. Karasawa and W. A. Goddard, III, *Macromolecules*, 1992, **25**, 7268-7281.
67. H. Ohigashi, *J Appl Phys*, 1976, **47**, 949-955.
68. K. Omote, H. Ohigashi and K. Koga, *J Appl Phys*, 1997, **81**, 2760-2769.
69. N. Tsutsumi, Y. Ueda, T. Kiyotsukuri, A. S. DeReggi and G. T. Davis, *J Appl Phys*, 1993, **74**, 3366-3372.
70. Q. Meng, W. Li, Y. Zheng and Z. Zhang, *J Appl Polym Sci*, 2010, **116**, 2674-2684.
71. Y. Tang and J. Scheinbeim, *Journal of Polymer Science Part B: Polymer Physics*, 2003, **41**, 927-935.
72. M. Li, N. Stingelin, J. J. Michels, M.-J. Spijkman, K. Asadi, K. Feldman, P. W. M. Blom and D. M. de Leeuw, *Macromolecules*, 2012, **45**, 7477-7485.
73. H. Tanaka, A. J. Lovinger and D. D. Davis, *Journal of Polymer Science Part B: Polymer Physics*, 1990, **28**, 2183-2198.
74. R. Gregorio, M. R. Chaud, W. Nunes Dos Santos and J. B. Baldo, *J Appl Polym Sci*, 2002, **85**, 1362-1369.
75. G. Natta, G. Allegra, I. W. Bassi, D. Sianesi, G. Caporiccio and E. Torti, *Journal of Polymer Science Part A: General Papers*, 1965, **3**, 4263-4278.
76. G. Guerra, F. E. Karasz and W. J. MacKnight, *Macromolecules*, 1986, **19**, 1935-1938.
77. J. Datta and A. K. Nandi, *Polymer*, 1994, **35**, 4804-4812.

78. J. Datta and A. K. Nandi, *Polymer*, 1997, **38**, 2719-2724.
79. J. Datta and A. K. Nandi, *Polymer*, 1998, **39**, 1921-1927.
80. J. Datta and A. K. Nandi, *Polymer*, 1996, **37**, 5179-5187.
81. Z.-M. Dang, J.-K. Yuan, J.-W. Zha, T. Zhou, S.-T. Li and G.-H. Hu, *Prog Mater Sci*, 2012, **57**, 660-723.
82. Q. Wang and L. Zhu, *Journal of Polymer Science Part B: Polymer Physics*, 2011, **49**, 1421-1429.
83. J. Wu, C.-W. Nan, Y. Lin and Y. Deng, *Physical Review Letters*, 2002, **89**, 217601.
84. P. Barber, S. Balasubramanian, Y. Anguchamy, S. Gong, A. Wibowo, H. Gao, H. Ploehn and H.-C. Zur Loye, *Materials*, 2009, **2**, 1697.
85. J. Y. Li, L. Zhang and S. Ducharme, *Appl Phys Lett*, 2007, **90**, 132901.
86. M. Rahimabady, S. Chen, K. Yao, F. Eng Hock Tay and L. Lu, *Appl Phys Lett*, 2011, **99**, 142901.
87. R. Haggenmueller, J. E. Fischer and K. I. Winey, *Macromolecules*, 2006, **39**, 2964-2971.
88. D. R. Dillon, K. K. Tenneti, C. Y. Li, F. K. Ko, I. Sics and B. S. Hsiao, *Polymer*, 2006, **47**, 1678-1688.
89. W. Mian, S. Jia-Hua, K. P. Pramoda and G. Suat Hong, *Nanotechnology*, 2007, **18**, 235701.
90. B. P. Grady, F. Pompeo, R. L. Shambaugh and D. E. Resasco, *The Journal of Physical Chemistry B*, 2002, **106**, 5852-5858.
91. L. Priya and J. P. Jog, *Journal of Polymer Science, Part B: Polymer Physics*, 2002, **40**, 1682-1689.
92. D. Shah, P. Maiti, E. Gunn, D. F. Schmidt, D. D. Jiang, C. A. Batt and E. P. Giannelis, *Advanced Materials*, 2004, **16**, 1173-1177.
93. X. Zhang, Y. Ma, C. Zhao and W. Yang, *Appl Surf Sci*, 2014, **305**, 531-538.
94. H.-J. Ye, W.-Z. Shao and L. Zhen, *J Appl Polym Sci*, 2013, **129**, 2940-2949.
95. X. Huang, P. Jiang, C. Kim, F. Liu and Y. Yin, *Eur Polym J*, 2009, **45**, 377-386.
96. S. Ansari and E. P. Giannelis, *Journal of Polymer Science Part B: Polymer Physics*, 2009, **47**, 888-897.

97. P. Martins, A. C. Lopes and S. Lanceros-Mendez, *Progress in Polymer Science*, 2014, **39**, 683-706.
98. J. S. Andrew and D. R. Clarke, *Langmuir*, 2008, **24**, 670-672.
99. E. Erdtman, K. C. Satyanarayana and K. Bolton, *Polymer*, 2012, **53**, 2919-2926.
100. C. M. Costa, V. Sencadas, J. F. Mano and S. Lanceros-Méndez, *Journal*, 2006, **514-516**, 951-955.
101. K. Ke, Y. Wang, W. Yang, B.-H. Xie and M.-B. Yang, *Polymer Testing*, 2012, **31**, 117-126.
102. S. Liu and J. Zhai, *Journal of Materials Chemistry A*, 2015, **3**, 1511-1517.
103. A. Srivastava, P. Maiti, D. Kumar and O. Parkash, *Composites Science and Technology*, 2014, **93**, 83-89.
104. H. Tang and H. A. Sodano, *Nano Letters*, 2013, **13**, 1373-1379.
105. S. Liu, S. Xue, W. Zhang, J. Zhai and G. Chen, *Ceramics International*, 2015, **41, Supplement 1**, S430-S434.
106. Z.-M. Dang, J.-K. Yuan, S.-H. Yao and R.-J. Liao, *Advanced Materials*, 2013, **25**, 6334-6365.
107. F.-A. He, K. Lin, D.-L. Shi, H.-J. Wu, H.-K. Huang, J.-J. Chen, F. Chen and K.-H. Lam, *Composites Science and Technology*, 2016, **137**, 138-147.
108. X. Lin, J.-W. Tian, P.-H. Hu, R. Ambardekar, G. Thompson, Z.-M. Dang and P. Coates, *J Appl Polym Sci*, 2016, **133**, 42893.
109. L. V. Todorov, C. I. Martins and J. C. Viana, *J Appl Polym Sci*, 2014, **131**, n/a-n/a.
110. T. Tanaka, *Dielectrics and Electrical Insulation, IEEE Transactions on*, 2005, **12**, 914-928.
111. T. J. Lewis, *Dielectrics and Electrical Insulation, IEEE Transactions on*, 2004, **11**, 739-753.
112. P. Kim, N. M. Doss, J. P. Tillotson, P. J. Hotchkiss, M.-J. Pan, S. R. Marder, J. Li, J. P. Calame and J. W. Perry, *ACS Nano*, 2009, **3**, 2581-2592.
113. C.-W. Nan, Y. Shen and J. Ma, *Annual Review of Materials Research*, 2010, **40**, 131-151.
114. J. Fu, Y. Hou, M. Zheng, Q. Wei, M. Zhu and H. Yan, *ACS Applied Materials & Interfaces*, 2015, **7**, 24480-24491.

115. Q. G. Chi, J. F. Dong, G. Y. Liu, Y. Chen, X. Wang and Q. Q. Lei, *Ceramics International*, 2015, **41**, 15116-15121.

116. S. Ogitani, S. A. Bidstrup-Allen and P. A. Kohl, *Advanced Packaging, IEEE Transactions on*, 2000, **23**, 313-322.

117. S. Ramesh, B. A. Shutzberg, C. Huang, G. Jie and E. P. Giannelis, *Advanced Packaging, IEEE Transactions on*, 2003, **26**, 17-24.

118. P. Kim, S. C. Jones, P. J. Hotchkiss, J. N. Haddock, B. Kippelen, S. R. Marder and J. W. Perry, *Advanced Materials*, 2007, **19**, 1001-1005.

119. T. Zhou, J.-W. Zha, R.-Y. Cui, B.-H. Fan, J.-K. Yuan and Z.-M. Dang, *ACS Applied Materials & Interfaces*, 2011, **3**, 2184-2188.

120. L. Shaohui, Z. Jiwei, W. Jinwen, X. Shuangxi and Z. Wenqin, *ACS Applied Materials & Interfaces*, 2014, **6**, 1533-1540.

121. M. T. Buscaglia, M. Viviani, V. Buscaglia, L. Mitoseriu, A. Testino, P. Nanni, Z. Zhao, M. Nygren, C. Harnagea, D. Piazza and C. Galassi, *Physical Review B*, 2006, **73**, 064114.

122. Z.-M. Dang, H.-Y. Wang, B. Peng and C.-W. Nan, *J Electroceram*, 2008, **21**, 381-384.

123. N. Guo, S. A. DiBenedetto, P. Tewari, M. T. Lanagan, M. A. Ratner and T. J. Marks, *Chemistry of Materials*, 2010, **22**, 1567-1578.

124. Y. Song, Y. Shen, H. Liu, Y. Lin, M. Li and C.-W. Nan, *Journal of Materials Chemistry*, 2012, **22**, 8063-8068.

125. Y. Song, Y. Shen, H. Liu, Y. Lin, M. Li and C.-W. Nan, *Journal of Materials Chemistry*, 2012, **22**, 16491-16498.

126. M. Arbatti, X. Shan and Z. Y. Cheng, *Advanced Materials*, 2007, **19**, 1369-1372.

127. H. M. Jung, J.-H. Kang, S. Y. Yang, J. C. Won and Y. S. Kim, *Chemistry of Materials*, 2010, **22**, 450-456.

128. Y. Li, X. Huang, Z. Hu, P. Jiang, S. Li and T. Tanaka, *ACS Applied Materials & Interfaces*, 2011, **3**, 4396-4403.

129. V. Tomer, G. Polizos, C. A. Randall and E. Manias, *J Appl Phys*, 2011, **109**, 074113.

130. T. C. M. Chung, *Green and Sustainable Chemistry*, 2012, **2**, 9.

131. W. Yong, Z. Xin, C. Qin, B. Chu and Z. Qiming, *Dielectrics and Electrical Insulation, IEEE Transactions on*, 2010, **17**, 1036-1042.
132. A. Chauhan, S. Patel, R. Vaish and C. Bowen, *Materials*, 2015, **8**, 5439.
133. F. Takeo, F. Koji and F. Eiichi, *Japanese Journal of Applied Physics*, 1976, **15**, 2119.
134. M. Dietze and M. Es-Souni, *Sensors and Actuators A: Physical*, 2008, **143**, 329-334.
135. Y. Sui, W.-T. Chen, J.-J. Ma, R.-H. Hu and D.-S. Liu, *RSC Advances*, 2016, **6**, 7364-7369.
136. S. C K, U. Valiyaneerilakkal, K. Singh and S. Varghese, *J Appl Phys*, 2015, **118**, 204102.
137. W. Li, Q. Meng, Y. Zheng, Z. Zhang, W. Xia and Z. Xu, *Appl Phys Lett*, 2010, **96**, 192905.
138. W. Xia, Z. Xu, F. Wen, W. Li and Z. Zhang, *Appl Phys Lett*, 2010, **97**, 222905.
139. Xplore, http://www.xplore-together.com/products/micro-compounders).
140. N. K. Masao Kakudo, *X-Ray Diffraction by Polymers*, Elsevier Publishing Company, Amsterdam, London & New York, 1972.
141. V. Cauda, S. Stassi, K. Bejtka and G. Canavese, *ACS Applied Materials & Interfaces*, 2013, **5**, 6430-6437.
142. N. Shingne, M. Geuss, B. Hartmann-Azanza, M. Steinhart and T. Thurn-Albrecht, *Polymer*, 2013, **54**, 2737-2744.
143. E. Ozkazanc, H. Y. Guney, T. Oskay and E. Tarcan, *J Appl Polym Sci*, 2008, **109**, 3878-3886.
144. L. Li, M. Zhang, M. Rong and W. Ruan, *RSC Advances*, 2014, **4**, 3938-3943.
145. V. R. P, D. V. Khakhar and A. Misra, *J Appl Polym Sci*, 2010, **117**, 3491-3497.
146. P. Sajkiewicz, A. Wasiak and Z. Gocłowski, *Eur Polym J*, 1999, **35**, 423-429.
147. S. André-Castagnet and S. Tencé-Girault, *Journal of Macromolecular Science, Part B*, 2002, **41**, 957-976.
148. F. Fang, M. Z. Zhang and W. Yang, *J Appl Polym Sci*, 2007, **103**, 1786-1790.
149. H.-J. Ye, L. Yang, W.-Z. Shao, S.-B. Sun and L. Zhen, *RSC Advances*, 2013, **3**, 23730-23736.

150. J. Defebvin, S. Barrau, G. Stoclet, C. Rochas and J.-M. Lefebvre, *Polymer*, 2016, **84**, 148-157.
151. H. Guo, Y. Zhang, F. Xue, Z. Cai, Y. Shang, J. Li, Y. Chen, Z. Wu and S. Jiang, *CrystEngComm*, 2013, **15**, 1597-1606.
152. Y.-L. Loo, R. A. Register and A. J. Ryan, *Physical Review Letters*, 2000, **84**, 4120-4123.
153. M. Challier, J. Besson, L. Laiarinandrasana and R. Piques, *Engineering Fracture Mechanics*, 2006, **73**, 79-90.
154. M. Sharma, G. Madras and S. Bose, *Physical Chemistry Chemical Physics*, 2014, **16**, 14792-14799.
155. Y. Takahashi and H. Tadokoro, *Macromolecules*, 1980, **13**, 1317-1318.
156. J. Buckley, P. Cebe, D. Cherdack, J. Crawford, B. S. Ince, M. Jenkins, J. Pan, M. Reveley, N. Washington and N. Wolchover, *Polymer*, 2006, **47**, 2411-2422.
157. D. M. Esterly and B. J. Love, *Journal of Polymer Science Part B: Polymer Physics*, 2004, **42**, 91-97.
158. J. L. Lutkenhaus, K. McEnnis, A. Serghei and T. P. Russell, *Macromolecules*, 2010, **43**, 3844-3850.
159. F. Oliveira, Y. Leterrier, J.-A. Månson, O. Sereda, A. Neels, A. Dommann and D. Damjanovic, *Journal of Polymer Science Part B: Polymer Physics*, 2014, **52**, 496-506.
160. V. Sencadas, R. Gregorio and S. Lanceros-Méndez, *Journal of Macromolecular Science, Part B*, 2009, **48**, 514-525.
161. W. T. Mead, A. E. Zachariades, T. Shimada and R. S. Porter, *Macromolecules*, 1979, **12**, 473-478.
162. E. S. Sherman, *Polymer Engineering & Science*, 1984, **24**, 895-907.
163. A. Prasad, R. Shroff, S. Rane and G. Beaucage, *Polymer*, 2001, **42**, 3103-3113.
164. A. Keller and M. J. Machin, *Journal of Macromolecular Science, Part B*, 1967, **1**, 41-91.
165. T. Kanaya, I. A. Polec, T. Fujiwara, R. Inoue, K. Nishida, T. Matsuura, H. Ogawa and N. Ohta, *Macromolecules*, 2013, **46**, 3031-3036.
166. R. T. Chen, C. K. Saw, M. G. Jamieson, T. R. Aversa and R. W. Callahan, *J Appl Polym Sci*, 1994, **53**, 471-483.

167. Z. Bashir, J. A. Odell and A. Keller, *J Mater Sci*, 1986, **21**, 3993-4002.
168. L. Balzano, S. Rastogi and G. Peters, *Macromolecules*, 2011, **44**, 2926-2933.
169. A. J. Lovinger, G. T. Davis, T. Furukawa and M. G. Broadhurst, *Macromolecules*, 1982, **15**, 323-328.
170. K. Koga and H. Ohigashi, *J Appl Phys*, 1986, **59**, 2142-2150.
171. Y. J. Shin, R. H. Kim, H. J. Jung, S. J. Kang, Y. J. Park, I. Bae and C. Park, *ACS Applied Materials & Interfaces*, 2011, **3**, 4736-4743.
172. M. C. Christie, J. I. Scheinbeim and B. A. Newman, *Journal of Polymer Science Part B: Polymer Physics*, 1997, **35**, 2671-2679.
173. T. Furukawa, G. E. Johnson, H. E. Bair, Y. Tajitsu, A. Chiba and E. Fukada, *Ferroelectrics*, 1981, **32**, 61-67.
174. W. J. Hu, D.-M. Juo, L. You, J. Wang, Y.-C. Chen, Y.-H. Chu and T. Wu, *Scientific Reports*, 2014, **4**, 4772.
175. M. Kobayashi, K. Tashiro and H. Tadokoro, *Macromolecules*, 1975, **8**, 158-171.
176. Y. Tan, J. Zhang, Y. Wu, C. Wang, V. Koval, B. Shi, H. Ye, R. McKinnon, G. Viola and H. Yan, *Scientific Reports*, 2015, **5**, 9953.
177. R. Gregorio, *J Appl Polym Sci*, 2006, **100**, 3272-3279.
178. R. Gregorio and R. C. CapitãO, *J Mater Sci*, 2000, **35**, 299-306.
179. J. R. Gregorio and M. Cestari, *Journal of Polymer Science Part B: Polymer Physics*, 1994, **32**, 859-870.
180. M. P. Silva, V. Sencadas, G. Botelho, A. V. Machado, A. G. Rolo, J. G. Rocha and S. Lanceros-Mendez, *Materials Chemistry and Physics*, 2010, **122**, 87-92.
181. N. Meng, R. Mao, W. Tu, X. Zhu, R. M. Wilson, E. Bilotti and M. J. Reece, *Polymer*, 2016, **100**, 69-76.
182. P. K. Agarwal, R. H. Somani, W. Weng, A. Mehta, L. Yang, S. Ran, L. Liu and B. S. Hsiao, *Macromolecules*, 2003, **36**, 5226-5235.
183. C. M. Costa, M. N. T. Machiavello, J. L. G. Ribelles and S. Lanceros-Méndez, *J Mater Sci*, 2013, **48**, 3494-3504.
184. H. Zhou and G. L. Wilkes, *J Mater Sci*, 1998, **33**, 287-303.
185. J. Liu, X.-L. Lu and C.-R. Wu, *J Appl Polym Sci*, 2013, **129**, 1417-1425.
186. C. Marega and A. Marigo, *Eur Polym J*, 2003, **39**, 1713-1720.
187. K. Tashiro and M. Kobayashi, *Phase Transit*, 1989, **18**, 213-246.

188. J. P. Penning and R. St. John Manley, *Macromolecules*, 1996, **29**, 84-90.
189. L. Zhu, *The Journal of Physical Chemistry Letters*, 2014, **5**, 3677-3687.
190. H. Yan, H. Zhang, R. Ubic, M. J. Reece, J. Liu, Z. Shen and Z. Zhang, *Advanced Materials*, 2005, **17**, 1261-1265.
191. N. Meng, X. Zhu, R. Mao, M. J. Reece and E. Bilotti, *Journal of Materials Chemistry C*, 2017, DOI: 10.1039/C7TC00162B.
192. M. Avrami, *The Journal of Chemical Physics*, 1939, **7**, 1103-1112.
193. M. Avrami, *The Journal of Chemical Physics*, 1941, **9**, 177-184.
194. J. Liu, H.-M. Ye, J. Xu and B.-H. Guo, *Polymer*, 2011, **52**, 4619-4630.
195. H. Tanaka, T. Ikeda and T. Nishi, *Appl Phys Lett*, 1986, **48**, 393-395.
196. Y. Wang, C.-M. Chan, L. Li and K.-M. Ng, *Langmuir*, 2006, **22**, 7384-7390.
197. F. Guan, J. Pan, J. Wang, Q. Wang and L. Zhu, *Macromolecules*, 2010, **43**, 384-392.